

The University of Hull

An analysis of ferromagnetic shape memory alloys produced by melt spinning,
sputtering and pulsed laser deposition.

Being a Thesis submitted for the Degree of
Doctor of Philosophy
In the University of Hull

By

Neil Dearing, MPhys

October 2009

Acknowledgements.....	1
Introduction.....	3
References.....	6
Chapter 1. Magnetism Theory.....	8
1.1 Introduction.....	8
1.2 The Quantum mechanical origin of magnetism.....	8
1.2.1 Magnetic moments and quantum mechanical modifications to classical theory.....	8
1.2.2 Quantum mechanical coupling.....	11
1.2.3 The magnetic moment in materials.....	12
1.2.4 Quenching of orbital angular momentum in the transition metals.....	13
1.2.5 The Zeeman effect.....	13
1.3 Magnetic Exchange.....	14
1.3.1 The Bethe-Slater curve.....	14
1.4 Mean field model.....	16
1.5 Magnetic anisotropy.....	18
1.5.1 Magnetocrystalline Anisotropy.....	18
1.5.2 Shape Anisotropy.....	19
1.5.3 Stress Anisotropy.....	20
1.5.4 Magnetisation rotation in a ferromagnet with uniaxial anisotropy.....	21
1.6 References.....	22
Chapter 2. Theory and mechanism of the shape memory effect.....	24
2.1 Introduction.....	24

2.2	The martensitic transformation.....	26
2.3	Superelasticity.....	27
2.4	The ferromagnetic shape memory effect.....	28
2.5	The Ni-Mn-Ga System	30
2.5.1	The effect of chemical composition.....	31
2.5.2	Magnetic properties of Ni-Mn-Ga	33
2.5.3	Magnetocrystalline anisotropy in Ni-Mn-Ga	34
2.5.4	The effect of adding dopants to Ni-Mn-Ga	35
2.6	The Ni-Fe-Ga system.....	36
2.7	The Co-Ni-Ga system	38
2.8	Thin Films	38
2.8.1	Sputtered Films.....	40
2.8.2	Pulsed Laser Deposited films.....	41
2.9	Modelling the ferromagnetic shape memory effect	42
2.10	References.....	47
Chapter 3.	Experimental	54
3.1	Melt Spinning	54
3.2	Sputtering.....	56
3.2.1	The sputtering system.....	58
3.3	Pulsed Laser Depositon	61
3.3.1	Preparation of the substrate.....	64
3.3.2	Preparation of the Target	65
3.4	Vibrating Sample Magnetometer (VSM).....	65

3.5	X-Ray Diffraction (XRD)	68
3.6	Transmission electron microscopy (TEM)	71
3.7	Capacitance Dilatometry	72
3.8	Magnetic Susceptibility.....	76
3.9	References.....	79
Chapter 4.	Results and Discussion	81
4.1	Melt Spun Ni-Mn-Ga	81
4.1.1	Sample preparation.....	81
4.1.2	Magnetisation.....	84
4.1.3	Crystal Structure	91
4.1.4	Magnetic Field Induced Strain.....	99
4.1.5	Discussion and Summary	103
4.2	Melt Spun Ni-Fe-Ga	105
4.2.1	Sample Preparation	105
4.2.2	Crystal Structure	106
4.2.3	Magnetisation.....	112
4.2.4	Discussion and summary	120
4.3	Melt Spun Ni-Fe-Al.....	122
4.3.1	Sample Preparation	122
4.3.2	Magnetisation.....	123
4.3.3	Crystal Structure	125
4.4	Sputtered Ni-Fe-Ga.....	128
4.4.1	Sample Preparation	128

4.4.2	Films on glass microscope slides.....	130
4.4.3	Films on Silicon Nitride Membranes.....	135
4.4.4	Summary and Conclusions	141
4.5	Ni-Mn-Ga Films produced by Pulsed Laser Deposition.....	143
4.5.1	Initial Deposition.....	143
4.5.2	Spectroscopic analysis of the ablation plume	144
4.5.3	Films on SiN membranes.....	146
4.5.4	Discussion and Summary.	153
4.6	References.....	155
Chapter 5.	Summary and Outlook.....	158
	References	164

Appendix 1: Publications resulting from this work:

Acknowledgements

Inevitably, there are several people who deserve a great amount of praise and thanks for their support and help, both practical and in terms of influence, inspiration and sheer patience.

First and foremost is the late Alan Jenner, whose dedication to and passion for his subject helped to ignite my own. Without his drive and support, it is likely there would never have been a PhD, and whilst he is greatly missed, this thesis stands as proof that his influence lives on in his students. Over the years he became a dear friend who always had time for me when I needed someone to talk to. His words of encouragement, coupled with the occasional kick up the rear are what kept me going through the course of this PhD.

Thanks must also go to Mary O'Neill and Pete Dyer, who kindly took on both myself and this project after Alan's passing. More patience, along with steady hands and constructive criticism have been just as valuable in helping me see this through to a conclusion.

No researcher is worth anything without technicians – so a big thank you must also go to the late Alan Boyer and to the late Paul Monk for their help and assistance in designing and building the equipment I needed for this research – and in how to mend it later on.

One more thank you that must be passed on is to the friends and family who offered so much support during the writing up phase, despite no doubt despairing of this ever finishing.

Finally, this work would not have been possible without the funding provided by the EPSRC, who should receive plenty of thanks – as without them, so much research would never be possible.

Introduction

Ferromagnetic shape memory alloys (FSMA) have recently attracted much interest and research because of their large magnetic-field induced strain. Strains of up to 10% have been reported in single crystals of Ni_2MnGa at room temperature. The mechanism of twin boundary motion is understood to be responsible for the strain in FSMA's and theoretically allows for a full crystal lattice distortion strain, which is 10% in the case of orthorhombic martensites[1] and 5-6% in the case of tetragonal martensites[2, 3]. These strains however are only achievable in single crystals and much smaller strains have been observed in polycrystalline samples. Here, competition of the randomly orientated grains restrict the cooperative twin boundary motion that is evident in single crystals.

Melt spun ribbons are often highly textured and may offer a method of producing ribbons in a form useful as a start material for applications, i.e. basis of a useful 'bulk' compact form. Magnetic and structural properties of melt spun Ni-Mn-Ga have previously been reported[4-7]. Applied magnetic field has been shown to affect the transformation strain on cooling[8]. Ni-Mn-Ga alloys form a Heusler (L2_1) lattice which, on cooling, undergoes a diffusionless transformation beginning at the martensite start temperature M_s into either a tetragonal or orthorhombic martensite, both of which are highly twinned. The reverse transformation begins at the austenite start temperature A_s and both transformations occur over a range of approximately 10K. The type of martensite

formed depends strongly on the composition of the sample and its thermal history. The influence of atomic order in Ni-Mn-Ga alloys has also been studied [9]. It has been found that the degree of atomic order plays a large part in determining the martensitic transition temperature. This temperature is suppressed significantly in the disordered B2 structure where there is little correlation of the Mn and Ga atoms at the body center. Ni₂MnGa undergoes a B2 to L2₁ (Heusler) transition at 1071K on cooling [10]. In this work the structural and magnetic properties of melt spun Ni-Mn-Ga ribbons are presented and the effect of an applied magnetic field on the transformation strain is shown for the case of annealed ribbons under tensile stress.

It is the intention of this work to explore the properties of melt-spun ribbons of the ferromagnetic shape memory alloys Ni-Mn-Ga and Ni-Fe-Ga with the addition of Tb. A range of compositions of both alloys have been created and analysed for both structural and magnetic properties. Melt spun ribbons are usually either amorphous or nanocrystalline, so the effect of heat treatments to both relieve stress and re-crystallise the ribbons is also explored. This provides some insight into how the crystal structure and magnetic properties evolve with annealing temperature

Thin films of these ferromagnetic shape memory alloys were also produced by both sputtering and pulsed laser deposition in order to characterise their behaviour and gain some insight into the growth conditions necessary to

successfully produce thin films of ferromagnetic shape memory alloys. This was done because thin films grown at low temperatures can have similar properties to the melt spun ribbons, in that they are nanocrystalline or amorphous. It was hoped that producing and analysing these thin films would yield some more information about the behaviour of polycrystalline ferromagnetic shape memory alloys.

Chapter 1 discusses the theory of magnetism, beginning with a discussion of the origins of magnetism and the magnetic moment. It moves on to talk about the quantum mechanical theories of magnetism and gives an account of magnetic anisotropy and how this affects materials.

Chapter 2 introduces Ferromagnetic shape memory alloys and presents the theory behind these alloys. Several alloy systems are explored and the effects of heat treatments and compositional changes are discussed. The properties of thin films of ferromagnetic shape memory alloys from the literature are presented to illustrate the state of the art in this area at the time of writing.

Chapter 3 describes the experimental techniques used in this research, beginning with the production techniques of melt spinning, sputtering and pulsed laser deposition. This is followed by a discussion of the various material analysis methods that were used.

Chapter 4 presents the results of this work and is split into sections based on the material system and production technique. Melt spun ribbons of Ni-Mn-Ga, Ni-Fe-Ga and Ni-Fe-Al are presented and their magnetic and magnetoelastic properties are discussed. This is followed by an analysis of sputtered Ni-Fe-Ga films and Pulsed laser deposited films of Ni-Mn-Ga.

Finally chapter 5 summarises the work and draws some conclusions about the production methods and material systems studied in this work.

References

- [1] A. Sozinov, A. A. Likhachev, N. Lanska, K. Ullakko, and V. K. Lindroos, "10% magnetic-field-induced strain in Ni-Mn-Ga seven-layered martensite," *J. Physique IV*, vol. 112, pp. 955-958, 2003.
- [2] S. J. Murray, M. Marioni, S. M. Allen, and R. C. O'Handley, "6% magnetic-field-induced strain by twin-boundary motion in ferromagnetic Ni-Mn-Ga," *Appl. Phys. Lett*, vol. 77, pp. 886-888, 2000.
- [3] O. Heczko, A. Sozinov, and K. Ullakko, "Giant field-induced reversible strain in magnetic shape memory NiMnGa alloy," *IEEE Trans. Mag.*, vol. 36, pp. 3266-3268, 2000.
- [4] J. Pons, C. Sugui, V. A. Chernenko, E. Cesari, P. Ochin, and R. Portier, "Transformation and ageing behaviour of melt-spun Ni-Mn-Ga shape memory alloys," *Mater. Sci. Eng.*, vol. A273-275, pp. 315-319, 1999.

- [5] F. Albertini, S. Besseghini, A. Paoluzi, L. Pareti, M. Pasquale, F. Passaretti, C. P. Sasso, A. Stantero, and E. Villa, "Structural, Magnetic and Anisotropic Properties of Ni₂MnGa Melt-Spun Ribbons," *J. Magn. Magn. Mat.*, vol. 242-245, pp. 1421-1424, 2002.
- [6] V. A. Chernenko, V. V. Kokorin, and I. N. Vitenko, "Properties of ribbon made from shape memory alloy Ni₂MnGa by quenching from the liquid state," *Smart Mater. Struct.*, vol. 3, pp. 80-82, 1994.
- [7] O. Heczko, P. Svec, D. Janickovic, and K. Ullakko, "Magnetic properties of Ni-Mn-Ga ribbon prepared by rapid solidification," *IEEE Trans. Mag.*, vol. 38, pp. 2841-2843, 2002.
- [8] P. A. Algarabel, C. Magen, L. Morellon, M. R. Ibarra, F. Albertini, N. Magnani, A. Paoluzi, L. Pareti, M. Pasquale, and S. Besseghini, "Magnetic-field-induced strain in Ni₂MnGa melt-spun ribbons," *J. Magn. Magn. Mater.*, vol. 272-76, pp. 2047-2048, 2004.
- [9] M. Kreissl, T. Kanomata, M. Matsumoto, K. U. Neumann, B. Ouladdiaf, T. Stephens, and K. R. A. Ziebeck, "The influence of atomic order and residual strain on the magnetic and structural properties of Ni₂MnGa," *J. Magn. Magn. Mater.*, vol. 272-76, pp. 2033-2034, 2004.
- [10] V. V. Khovailo, T. Takagi, A. N. Vasilev, H. Miki, M. Matsumoto, and R. Kainuma, "On order-disorder (L2(1) → B2) phase transition in Ni_{2+x}Mn_{1-x}Ga Heusler alloys," *Phys Stat. Solidi A*, vol. 183, pp. R1-R3, 2001.

Chapter 1.....Magnetism Theory

1.1 Introduction

This chapter provides the background theory necessary to understand the magnetic phenomena present in ferromagnetic shape memory alloys (FSMA). In particular, attention is paid to the causes and effects of magnetic anisotropy because of its significance in determining how the FSMA behaves under the application of an external magnetic field. Analysis of the hysteresis loop, which is key to determining the anisotropy is also addressed.

1.2 The Quantum mechanical origin of magnetism

In the classical approach the magnetic moment arises from the angular momentum of the unpaired electrons where any value of angular momentum is allowed. In reality however quantum mechanics dictates that the angular momentum must be quantised leading to a quantisation of the individual magnetic moments.

1.2.1 Magnetic moments and quantum mechanical modifications to classical theory

The magnetic moment is considered to have two components arising from an orbital and spin angular momentum. The orbital contribution can be understood by considering the electron orbit as a current loop and the electronic mass

orbiting the nucleus makes the connection with angular momentum. The relationship between magnetic moment and angular momentum can be shown experimentally by suspending a ferromagnetic rod from a thin fibre. A coil is wrapped around the rod and when the rod is magnetized it begins to rotate as a direct result of the change in angular momentum[1]. This is the Einstein-de Haas effect. The spin angular momentum is considered classically by examining a rotating charged body with the charge assumed to be on the surface. The classical approach breaks down however because it predicts unrealistically large tangential velocities from the spin angular momentum and therefore a quantum mechanical approach is required. In order to describe the magnetic moments in a quantum mechanical framework two new quantum numbers are used to define the magnetic properties of the electrons, these are the orbital, l and spin, s angular momentum quantum numbers.

The orbital moment m_0 can be shown classically by considering an electron in an elliptical orbit around a nucleus to be

$$m_0 = -\left(\frac{e}{2m_e}\right)p_0 \quad \text{Eq. 1.1}$$

where m_e is the electronic mass and p_0 is the orbital angular momentum. Quantum mechanics shows that the angular momentum must be quantised, taking values that are multiples of $h/2\pi$. The angular momentum quantum number, l can also take values of $0, 1, \dots, n-1$ where n is the principal quantum number with the orbital magnetic moment then being given by

$$m_0 = -l \cdot \left(\frac{eh}{4\pi m_e} \right) \quad \text{Eq. 1.2}$$

This is the origin of the Bohr magneton, μ_b which is conveniently defined as $eh/4\pi m_e$. It is clearly the smallest unit of electronic magnetic moment that a single electron can take and as such is a convenient unit for describing the magnetic moment per atom.

Electron spin also leads to a magnetic moment and is given classically by considering a spinning charged body.

$$m_e = -\left(\frac{e}{m_e}\right)p_s \quad \text{Eq. 1.3}$$

The spin moment is also necessarily quantised, with spin quantum number s which is always equal to $\frac{1}{2}$ for an electron. The spin magnetic moment then becomes

$$m_e = -s\left(\frac{eh}{2\pi m_e}\right) \quad \text{Eq. 1.4}$$

It is clear that spin angular momentum contributes twice as much to the magnetic moment and the total moment is the vector sum of the angular and spin momenta.

$$m_{tot} = \mu_b(l + 2s) = -g\mu_b p_{tot} \quad \text{Eq. 1.5}$$

where g is the Lande splitting factor and depends upon the relative contributions of spin and angular momentum whereby it is 2 for spin only and 1 for orbital only contributions.

It should be noted that there is a wave mechanical correction for calculating the total magnetic moment and it shows that the assumption that magnetic moment is an integral multiple of μ_B and s is not quite true. The corrected value for total magnetic moment of a single electron is shown by[2]

$$m_{tot} = \mu_B [\sqrt{s(s+1)} + \sqrt{l(l+1)}] = \mu_B [\sqrt{j(j+1)}] \quad \text{Eq. 1.6}$$

1.2.2 Quantum mechanical coupling

The above consideration of magnetic moments is only for single electrons, whereas there may be several electrons in an unfilled shell of the atom, all of which contribute to the total atomic moment. The quantum mechanical coupling between electrons within an atom determines how the individual electronic moments are summed to find the total atomic moment. There are two obvious methods of summing the orbital and spin moments depending upon whether the l vectors and s vectors of individual atoms are strongly coupled, (l-l) and (s-s) coupling, or whether the (l-s) coupling is dominant. The case whereby (s-s) and (l-l) coupling is dominant is known as Russell Saunders coupling and is common to most materials including the transition metals and 4f elements. In this case the total angular momentum can be found by summing the orbital and spin components separately.

$$J = \sum l_i + \sum s_i \quad \text{Eq. 1.7}$$

1.2.3 The magnetic moment in materials

The phenomenon of magnetism can be explained on the atomic scale by the magnetic moments possessed by unpaired electrons. The unpaired electrons which contribute to magnetism are often involved in forming chemical bonds. This is the case for the 3d transition metals (TM) and oxides where it is the 3d shell that has the unpaired electrons and this is the outermost shell apart from the 2 electrons in the 4s shell. Since the electrons possessing the magnetic moment are in one of the outermost electron shells they can directly interact with their neighbouring atoms and can freely move between atoms in metals. This is however not the case for the Rare Earth (RE) elements whose unpaired electrons are in the 4f shell which is surrounded by the 5s5p5d6s shells which effectively screen the 4f shell from its neighbouring atoms. Therefore any exchange interaction between 4f shells must proceed in an indirect manner which leads to some of the significant differences between TM and RE elements. Another important difference between these two groups is that the 4f shell has up to 14 electrons compared with up to 10 in the 3d shell which can result in a larger magnetic moment in the RE elements.

On the macroscopic scale we can only detect the magnetic moments if they are aligned in some way and have long range order such as in a ferromagnetic material for example. Paramagnetic materials do not display a macroscopic magnetic moment except on application of an external magnetic field. Many

other types of order do occur but only ferromagnetic and antiferromagnetic order need be considered for the analysis of Ferromagnetic shape memory alloys.

1.2.4 Quenching of orbital angular momentum in the transition metals

Interestingly when the magnetic moments for the transition metals are calculated they seem to show values similar to what would be predicted if only the spin component was included in the calculation i.e. in the transition elements the orbital component generally disappears. A good description of this effect has been written by Morrish[3] and Kittel[4]. The 4f elements do not display this effect however, due in part to the fact that the magnetic 4f shell is well shielded by the 6s,5p and 5d shells whereas the unpaired electrons in the 3d elements are in the outer shell and are generally loosely bound.

1.2.5 The Zeeman effect

The Zeeman effect arises from the fact that an external magnetic field changes the electron energy levels in an atom[5]. This effect can be readily observed by the splitting of spectral lines[6] in the presence of a magnetic field with the energy difference given by

$$\Delta E = -\mu_0 \Delta m \bullet H \qquad \text{Eq. 1.8}$$

where Δm is the difference in the component of magnetic moment along the field direction.

1.3 Magnetic Exchange

Macroscopic magnetic order requires a driving force that causes some sort of alignment of the localised atomic moments. They can be coupled via an externally applied magnetic field such as in paramagnetic materials or by an exchange interaction between neighbouring magnetic moments. Magnetic exchange generally aligns neighbouring moments either parallel or anti-parallel depending upon the sign of the exchange energy. The exchange energy originates from a quantum mechanical interaction between electrons with overlapping wave functions and the exchange Hamiltonian, H_{ij} can be written as

$$H_{ij} = -2J_{ij}s_i \bullet s_j \quad \text{Eq. 1.9}$$

where J_{ij} is the exchange energy and $s_{i,j}$ are the electron spins of the interacting electrons. Minimising H_{ij} shows that a negative J leads to anti-parallel alignment and a positive J results in parallel alignment of the moments. Magnetic materials that exhibit long range order with moments aligned parallel are said to be ferromagnetic eg. Ni, Fe, Co and those that have antiparallel alignment of adjacent moments are anti-ferromagnetic such as Manganese.

1.3.1 The Bethe-Slater curve

Bethe performed some calculations of the exchange integral[7] with respect to the 3d transition metals using published data of the radius of the d orbitals and interatomic spacing and showed that the exchange energy for two one electron systems can be written as[8]

$$J = \iint \psi_a^*(r_1)\psi_b^*(r_2) \left[\frac{1}{r_{ab}} - \frac{1}{r_{a2}} - \frac{1}{r_{b1}} + \frac{1}{r_{21}} \right] \psi_b(r_1)\psi_a(r_2) d\tau \quad \text{Eq. 1.10}$$

where r_{ab} is the interatomic distance, r_{a2} and r_{b1} are the distances between respective nuclei and electrons and r_{21} is the distance between electrons. The integral becomes positive for small r_{ab} or r_{21} or with large r_{a2} or r_{b1} and as a result the exchange integral can be plotted as a function of r_{ab}/r_d where r_d is the radius of the d orbital. This analysis correctly separates the ferromagnetic 3d elements from the antiferromagnetic elements and illustrates the point that lattice spacing in crystalline materials can significantly affect the exchange energy and therefore the magnetic order of a material.

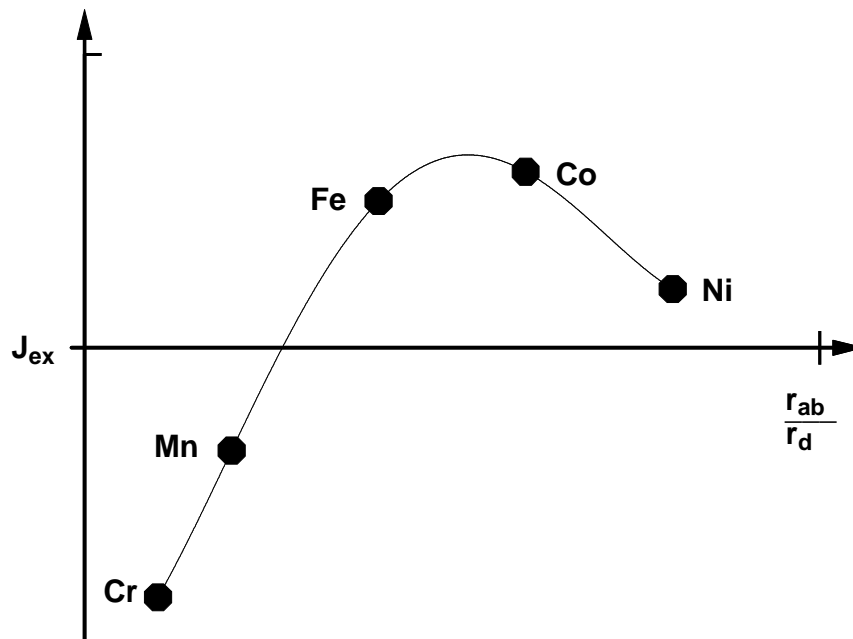


Figure 1.1 Bethe-Slater Curve

One of the main pieces of evidence in support of the Bethe-Slater curve is the existence of ferromagnetism in the Heusler alloys such as Cu_2MnAl which has a saturation magnetisation comparable with that of Nickel. Ferromagnetism is thought to arise from the fact that the Mn atoms are around 60% further apart than in elemental manganese and this makes the exchange energy positive. The common ferromagnetic shape memory alloy Ni_2MnGa forms a Heusler alloy with Mn at the body centre positions on the lattice resulting in the manganese atoms coupling ferromagnetically in the same manner as in Cu_2MnAl . The magnetic moment in Ni_2MnGa is thought to mainly arise from the manganese atoms with the nickel moment being small in comparison.

1.4 Mean field model

Weiss proposed that magnetic moments interact via an interaction field H_e which Weiss called the “molecular field”[9, 10]. This field is proportional to the magnetisation such that

$$H_e = \alpha M \quad \text{Eq. 1.11}$$

where α is the mean field constant and M is the magnetisation. This is equivalent to saying that every moment interacts equally with every other moment in the solid. In a paramagnetic material this is a reasonable assumption due to the homogeneous distribution of moment direction throughout the whole solid which leads to the local moment on a microscopic scale being the same as the bulk magnetisation. In a ferromagnetic material however this is no longer valid because of the ferromagnetic order which leads to the local magnetisation

being equal to the saturation magnetisation because adjacent magnetic moments are aligned parallel within a domain. The saturation magnetisation is the magnetisation of a material in the presence of an applied field sufficiently strong to align all of the magnetic moments. The bulk magnetisation, which is an average of all moments within a volume varies with the domain structure because the magnetisation direction in each domain may be different. Clearly the Weiss mean field model is not valid for a ferromagnetic sample but it is generally considered to be a good model if only single domains are considered in which case the interaction field becomes

$$H_e = \alpha M_s \qquad \text{Eq. 1.12}$$

where M_s is the spontaneous magnetisation within a domain. One important problem with this theory is that it does not consider the nearest neighbour interactions, it just assumes an average field and cannot explain the existence of antiferromagnetism or some of the more complex magnetic ordering that are observed.

Other models, such as the Ising model consider only the nearest neighbour interactions which can lead to both ferromagnetism and antiferromagnetism when α is positive and negative respectively.

1.5 Magnetic anisotropy

Magnetic anisotropy is responsible for the magnetic properties varying with direction in a crystal, leading to easy and hard axes of magnetisation. Magnetocrystalline anisotropy is fundamental in defining the magnetisation axis in permanent magnets as the magnetic moments in materials with high anisotropy are more difficult to rotate away from their easy axis under the action of a field. From a theoretical point of view magnetic anisotropy arises from a combination of the magnetic dipole interaction and from spin-orbit coupling. Magnetocrystalline anisotropy is the only type of magnetic anisotropy that is fundamentally linked to the crystal structure. Other types do exist however such as shape anisotropy and stress anisotropy.

1.5.1 Magnetocrystalline Anisotropy

As a result of the electrostatic crystal fields a magnetic crystal possesses easy and hard axes of magnetisation whereby it is easier to magnetise in some directions than others. The actual easy and hard directions depend upon the crystal symmetry, atomic spacing and the sign of the anisotropy energy. For a uniaxial material such as hexagonal cobalt the anisotropy energy density can be represented by a one constant approximation[11]

$$E = K_1 \sin^2 \theta \text{ Jm}^{-3} \qquad \text{Eq. 1.13}$$

where E is the energy density contributed to the system, K_1 is the anisotropy energy density and θ is the angle between unique axis and the magnetisation vector. From this equation it is clear that if K_1 is positive then the unique axis is

an easy axis and it follows that it is a hard axis if K_1 is negative. A cubic crystal with the associated higher symmetry can often be modelled with a one constant approximation although more correctly the following two constant equation should be used[12].

$$E = K_1(\cos^2 \theta_1 \cos^2 \theta_2 + \cos^2 \theta_2 \cos^2 \theta_3 + \cos^2 \theta_1 \cos^2 \theta_3) + K_2(\cos^2 \theta_1 \cos^2 \theta_2 \cos^2 \theta_3) \quad \text{Eq. 1.14}$$

Again E is the energy density, K_1 and K_2 are anisotropy constants and $\theta_1, \theta_2, \theta_3$ are the angles between magnetisation vector and the three crystal axes. In the cubic system if $K_1 > 0$ then the $\langle 100 \rangle$ direction is the easy axis and if $K_1 < 0$ the $\langle 111 \rangle$ direction is the easy axis. In most cases $K_1 \gg K_2$ so one constant gives a pretty good approximation.

The above equations for the anisotropy energy are for an unstrained crystal. The anisotropy energy also has a strain dependence resulting in magnetostriction, a phenomenon whereby the length of a magnetic material changes under the action of an applied field. This can be considered mathematically by minimising the sum of the elastic energy and the strain dependent anisotropy energy. It should also be noted here that amorphous materials do not exhibit this type of anisotropy purely because it is associated with crystal structure which they do not possess.

1.5.2 Shape Anisotropy

The physical shape of the magnetic sample also adds an extra anisotropy term as a result of magnetostatic effects and the demagnetisation factor. The

demagnetising field is a result of the dipole field created by a magnetised piece of magnetic material and can be written as:

$$H_d = N_d M \quad \text{Eq. 1.15}$$

where N_d and M are the demagnetisation factor and the magnetisation respectively. The demagnetisation factor is simply a shape dependent constant that is used to describe this effect. In general a sample will have a different N_d for each axis with short dimensions having a much larger N_d than a long dimension. As a result of this it is easier to magnetise a sample along its longer axis and indeed this is the main reason why the moments in a thin film will lie in the plane of the film rather than perpendicular to it. The energy density associated with the demagnetising field is written as

$$E_d = \frac{\mu_0}{2} N_d M^2 \quad \text{Eq. 1.16}$$

1.5.3 Stress Anisotropy

During most material fabrication techniques, and particularly so with melt spinning, stress is induced in the material which remains once the process is complete. As a result of magnetostriction the magnetic moments can be strongly coupled to stresses in the material. For example if a positive magnetostrictive material is put under tensile stress a magnetic easy axis will form along the axis of the stress. This is particularly noticeable in amorphous materials which lack any significant magnetocrystalline anisotropy. Hence amorphous magnetic materials can make good stress sensors.

1.5.4 Magnetisation rotation in a ferromagnet with uniaxial anisotropy

The magnetisation process proceeds by both domain wall motion and magnetisation rotation. The anisotropy energy does not affect domain wall motion but it is the main factor governing the magnetisation rotation process. Rotation of the magnetic moments can be modelled by minimising the field energy, E_H and the anisotropy energy, E_a such that the total energy would be

$$E_{tot} = E_a(\theta) + E_H \quad \text{Eq. 1.17}$$

For a uniaxial material this becomes

$$E_{tot} = K_1 \sin^2 \theta + \mu_0 M_s H \cos \phi \quad \text{Eq. 1.18}$$

where θ and ϕ are the angles between magnetic moment and the anisotropy axis and the applied field respectively. Clearly the moment angle will be found by minimising this equation with respect to θ which results in the following equation

$$\sin(2\theta) = \frac{\mu_0 M_s H}{K_1} \cos(\phi) \quad \text{Eq. 1.19}$$

1.6 References

- [1] A. Einstein and W. J. d. Haas, "Experimental proof of the existence of Ampère's molecular currents," *Proc. KNAW*, vol. 18 I, pp. 696-711, 1915.
- [2] D. Jiles, "Introduction to magnetism and magnetic materials," Chapman and Hall, 1998, pp. 271.
- [3] A. H. Morrish, *The physical principles of magnetism*: Wiley, New York, 1965.
- [4] C. Kittel, *Introduction to solid state physics*: Wiley, New York, 1986.
- [5] P. Zeeman, "On the influence of Magnetism on the Nature of the Light emitted by a Substance," *Phil. Mag*, vol. 43, pp. 226, 1897.
- [6] P. Zeeman, "Doubles and triplets in the spectrum produced by external magnetic forces," *Phil. Mag*, vol. 44, pp. 55, 1897.
- [7] H. Bethe, *Handb. d. Phys*, vol. 24, pp. 595, 1933.
- [8] D. Jiles, "Introduction to magnetism and magnetic materials," Chapman and Hall, 1998, pp. 299.
- [9] P. Weiss, "The variation of ferromagnetism with temperature," *Compt. Rend*, vol. 143, pp. 1136, 1906.
- [10] P. Weiss, "L'hypothèse du champ moléculaire et la propriété ferromagnétique," *J. Phy*, vol. 6, pp. 661, 1907.
- [11] S. Blundell, "Magnetism in condensed matter," Oxford University Press, 2001, pp. 128-129.

[12] D. Jiles, "Introduction to magnetism and magnetic materials," Chapman and Hall, 1998, pp. 152-153.

Chapter 2. ...Theory and mechanism of the shape memory effect

2.1 Introduction

The Shape Memory Effect (SME) is a diffusionless martensitic phase transition in which the atoms move co-operatively on heating or cooling through the transition temperature. The high temperature phase, often called the parent or austenitic phase is usually cubic, with the martensite having a lower symmetry close packed structure

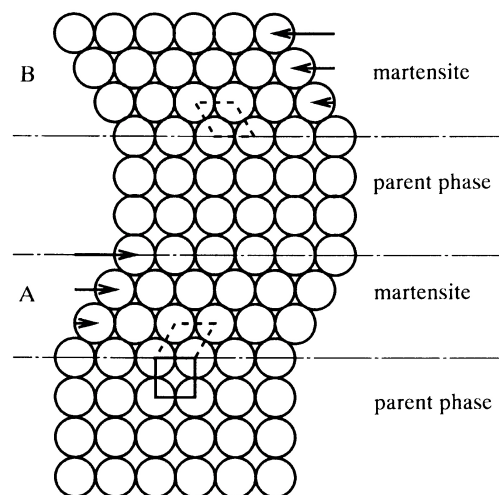


Figure 2.1. A simplified 2D illustration of the martensitic transformation showing the two phases and also the two martensitic twin variants, labeled A and B. The arrows represent the motion of the atomic planes as the martensitic transformation proceeds.

When cooled past the martensite start temperature M_s the cubic austenite phase becomes unstable and transforms by a shear like mechanism into martensite

over a small temperature range, usually of the order of a few degrees, finishing at the temp M_f . T_{mart} is used to refer to M_s - M_f . The reverse transition temperatures are usually denoted by A_s and A_f for the start and finish temperatures respectively. In NiMnGa there is usually some hysteresis of the order of 10K. Note that transition temperatures M_s , M_f , A_s and A_f will be in italics throughout in order to differentiate them from the saturation magnetization M_s . It can be seen in Figure 2.1 that the two regions A and B have the same structure with different orientations. These are the twin variants and form to accommodate the change in shape that occurs with the martensitic transformation. Since the martensite has a lower symmetry than the cubic austenite many variants can be formed from the same parent phase in order to accommodate the change in lattice parameters. It is this martensitic transition which forms the basis of the shape memory effect.

In general a shape memory alloy can be distorted in the martensite phase by applying a stress which causes twin boundary motion to occur in the highly twinned martensitic structure, leading to a reorientation of twin variants. The process of twin boundary motion requires an applied force to overcome the pinning force and as such is an irreversible process so the material remains in its strained state when the applied stress is removed. In most shape memory alloys the original shape is returned on heating through the transition temperature and it is retained on cooling; this is referred to as the one way shape memory effect.

With some materials it is possible to “train” them such that on passing through the transition temperature they transform from one shape to another and back again on cooling. The two stable states are created by a training process which usually involves a series of compressions in the martensite phase which creates defects and dislocations that will later guide the formation of martensite in a particular orientation. These lead to what is called the two way shape memory effect[1].

2.2 The martensitic transformation

The martensitic transformation in shape memory alloys is a reversible first order transformation that is exothermic on cooling as the martensite is formed. There is hysteresis associated with the transformation and there is a temperature range over which both austenite and martensite coexist, typically less than 10 degrees but this depends on the material processing. The most common method for detecting these transitions is differential scanning calorimetry which measures heat flow at a constant heating and cooling rate, typically 10 K/minute. As in most techniques there is a trade off between sensitivity and resolution, with lower heating rates giving higher temperature resolution but lower sensitivity and vice versa. The martensitic transformation in Ferromagnetic shape memory alloys can also be observed using magnetic techniques such as field cooling and by observing the small signal susceptibility as it changes with temperature. Both of these techniques rely on the fact that there is a large difference in magnetic anisotropy between the two phases, with the magnetocrystalline anisotropy of the

cubic austenite being several orders of magnitude lower than the martensite which is typically tetragonal having a unique easy axis along the short axis. This anisotropy is key to describing the field induced strain in ferromagnetic shape memory alloys.

2.3 Superelasticity

Some shape memory alloys, NiTi in particular, exhibit a phenomenon known as superelasticity. These materials are in the austenite phase under normal conditions but on the application of an external stress the crystal structure changes to a lower symmetry martensite phase to accommodate the stress and the material strains accordingly. These strains can be very large, up to 10% which leads to this effect often being described as rubber like behaviour. The material distorts when stressed but regains its former shape upon release of the stress.

The mechanism is explained by the stress creating a state whereby the crystal can lower its internal energy by forming preferentially orientated martensite. This stress induced martensite becomes unstable on removal of the stress and the crystal returns to its austenitic form. It should be noted that within the elastic limit these transformations are diffusionless and no atomic bonds are broken, i.e. no slip occurs.

2.4 The ferromagnetic shape memory effect

The ferromagnetic shape memory effect (FSME) arises from the fact that the martensite has a large magnetoelastic anisotropy with a unique easy axis (the short c-axis in Ni-Mn-Ga)[2]. This, coupled with the exceptionally low twinning stress, eg. typically 2MPa in Ni-Mn-Ga, results in a magnetic field being able to move twin boundaries. Thus when a field is applied twin variants with the c-axis orientated away from the field axis have a higher magnetostatic energy than those with easy axis along the field direction. It is this excess energy that provides for the force on the twin boundaries[3]. The magnitude of the anisotropy energy[4] is key to this process because if it is not large enough then the magnetic moments will rotate towards the field direction reducing the force on the twin boundary before it exceeds the pinning force and no twin boundary motion will occur. This dependence also means that materials with higher anisotropy energy will be able to produce larger forces on application of a field which will lead to devices with higher energy densities. This mechanism also leads to a relatively low blocking stress above which the FSMA can not strain no matter how high the applied field. This is typically 2-3MPa for Ni-Mn-Ga[5].

The maximum reversible field induced strain in single crystal samples has been found to be of the order of 10%, with polycrystalline materials[6] having a much lower field induced strain of <1%[7]. This discrepancy is a result of the random orientation of crystal grains with some contributing more than others to the effect. In a single crystal however the whole sample can contain only two twin variants

and total conversion of one to the other can occur under the action of a magnetic field with the result that the maximum strain is equal to the lattice distortion, which is ~5%, or ~10% for tetragonal and orthorhombic Ni-Mn-Ga martensites respectively. This is an order of magnitude greater than the 0.2% that the best magnetostrictive material Terfenol D can produce. These large strains have only been demonstrated in single crystals whilst polycrystalline materials show a maximum of approximately 1% strain. This is typically caused by the random orientation of the crystallites and the fact that only a small proportion of them produce a significant force on their respective twin boundaries with a particular field direction. This also causes an additional stress as the material changes length and the change of length of some crystallites opposes others limiting the maximum force and extension that is available in polycrystalline materials.

It should be noted that once a field has moved the twin boundaries there is no force to restore the material to its original shape and it remains in its extended (or contracted) state. This is one of the significant differences to the well known magnetostrictive materials which rely instead on magnetization rotation producing a purely magnetostrictive strain. There are two methods available to compensate for this in actuator design, either a field perpendicular to the original field can be used to restore the original length or a force provided by some physical mechanism will restore it to the original length. This restoring force is crucial if the material is to be used as an actuator[8].

2.5 The Ni-Mn-Ga System

Ni-Mn-Ga alloys have been found to exhibit the FSME over a range of compositions around the stoichiometric composition Ni_2MnGa . This effect was first observed in Ni-Mn-Ga by Ullakko in 1996[9]. A strain of $\sim 0.2\%$ was observed in a stoichiometric Ni_2MnGa Heusler alloy. Larger strains of 5% were observed in 1999[10] in a tetragonal martensite and a 10% strain was seen in 2002 in an orthorhombic martensite[11].

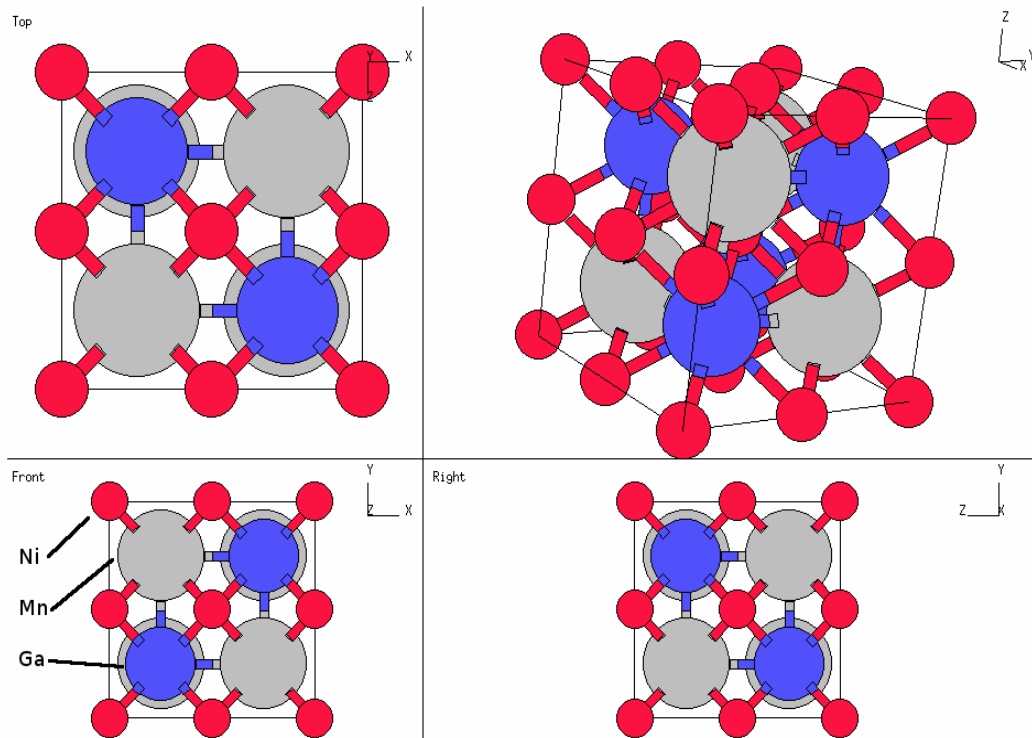


Figure 2.2 Heusler (L₂₁) structure of Ni₂MnGa. Note that it is a Body Centred structure with long range order of the Mn and Ga atoms at the body centres.

The crystal structure of Ni-Mn-Ga strongly depends on the chemical composition and the heat treatments it has undergone. All samples have a $L2_1$ body centred cubic (BCC) high temperature phase (Figure 2.2) but the nature of the martensite phase varies[12, 13]. Three different martensite phases have been observed so far, a tetragonal martensite with a lattice distortion of 20%, a 5 layer modulated, almost tetragonal martensite (5M) with a distortion of 5% and a 7 layer modulated, almost orthorhombic martensite (7M) with a distortion of 10%[14]. Both types of the modulated martensites are monoclinic but the exact parameters of the structure have not yet been agreed upon and for the purposes of calculations are approximated as tetragonal and orthorhombic respectively[15]. In principle the tetragonal phase should give a larger field induced strain but the twinning stress in this phase is large enough ($\sim 20\text{MPa}$) to impede twin boundary motion with magnetization rotation occurring before the twin boundaries move. Both of the modulated martensites have a lower twinning stress of $\sim 2\text{MPa}$ which is lower than the force that can be produced by the action of a magnetic field[16]. As a result single crystals of these two materials can produce strains equal to their lattice distortions with the correct orientation of magnetic field[5].

2.5.1 The effect of chemical composition

In order to create a viable actuator material it is necessary to understand how the magnetic and structural properties vary with composition[17]. Various composition series have been examined to determine the effect of substituting all three elements and a strong linear correlation between martensitic transition

temperature and the number of valence electrons per atom ($= \frac{V_e}{a}$) is found. $\frac{V_e}{a}$ is equal to 10, 7 and 3 for Ni, Mn and Ga respectively and the average $\frac{V_e}{a}$ values for the alloy are calculated. 5M martensites have been shown to exist with $7.60 < \frac{V_e}{a} < 7.70$ and $301\text{K} < M_s < 342\text{K}$ [18]. Also 7M martensites occur with $7.66 < \frac{V_e}{a} < 7.71$ and $335\text{K} < M_s < 353\text{K}$ [19]. Non modulated martensites have been observed with $7.60 < \frac{V_e}{a} < 7.82$ and $310\text{K} < M_s < 550\text{K}$. Interestingly a nickel content above 51% always results in a non modulated martensite regardless of the $\frac{V_e}{a}$ ratio and the optimal range for obtaining a 5M or 7M martensite is 48% - 51% Ni with 27-32% Mn. The different martensitic structures can exist with alloys of almost the same composition, a change of <2% can result in any of the three structures and there is some overlap. This suggests that the martensitic structure is sensitive to something other than just the composition. It is likely that the other factor is the atomic order which is influenced by the heat treatment temperature and duration. A long anneal is usually required at a temperature near to the L_{21} ordering temperature in order to promote the Heusler structure. The L_{21} ordering temperature is the temperature below which long range order of the Mn and Ga atoms at the body centres begins to form, resulting in the Heusler structure with alternate Mn and Ga atoms at the centre of adjacent lattice cells. The difference in heat treatments is probably responsible for the fact that several different structures have been obtained with very similar compositions.

In the alloy series $\text{Ni}_{50}\text{Mn}_{25+x}\text{Ga}_{25-x}$ for example [15], M_s increases linearly with x from 11K to 110K. The saturation magnetization decreases from $100 \text{ Am}^2\text{kg}^{-1}$ ($x=0$) to $68 \text{ Am}^2\text{kg}^{-1}$ ($x=5$). This reduction of magnetization is attributed to antiferromagnetic coupling of the excess Mn atoms. Assuming this mechanism, the magnetic moment of Ni-Mn-Ga is predominantly on the Mn atom and the saturation magnetization σ_s would be

$$\sigma_s = \sigma_s^{Mn} - \frac{x}{25} \sigma_s^{Mn} \quad \text{Eq. 2.1}$$

It does however not follow this linear rule and it appears that the moment contributed by the excess Mn atoms increases with Mn content. This suggests that the excess Mn atoms alters the electronic structure of the unsubstituted Mn atoms causing a greater than expected reduction in σ_s .

2.5.2 Magnetic properties of Ni-Mn-Ga

The austenite and martensite show distinctly different magnetic characteristics. The cubic austenite is magnetically very easy, having a low anisotropy energy and it exhibits low hysteresis, low coercivity and remnance typical of a magnetization process proceeding primarily by magnetization rotation. The martensite by comparison shows a large uniaxial anisotropy with easy axis along the short c-axis. It is this difference that allows the martensitic phase change to be observed by field cooling the material through its transition temperature. A significant drop in the magnetic moment is observed as the transformation proceeds as a result of the large change in anisotropy forcing some of the

moments away from the field direction. This provides another method to observe the transformation temperatures and its hysteresis.

It is also possible to observe twin boundary motion in the hysteresis loop of a shape memory alloy as it produces an abrupt change in magnetization once a critical field for actuation is reached. If the material is stressed then this will be reversible as the field is removed and will be observed in both field directions. However if the material is unstressed then this may be a one way effect and the material does not return to its original state after the field is removed[20].

2.5.3 Magnetocrystalline anisotropy in Ni-Mn-Ga

It is accepted that a large anisotropy energy is required for the FSME to occur in these materials. The anisotropy energy of the parent austenite phase is typically low, of the order 10^3 Jm^{-3} . The martensite however has an anisotropy several orders of magnitude greater, typically $1.6-1.7 \times 10^5 \text{ Jm}^{-3}$ [10, 21-23] for the 5M and 7M martensites whereas the non modulated tetragonal martensite has a higher anisotropy of $-2.3 \times 10^5 \text{ Jm}^{-3}$. The 5M martensite has uniaxial anisotropy with the short c axis [001] as an easy axis, the 7M structure has a hard axis along [100], an intermediate axis along [010] and an easy axis [001]. By comparison the non modulated structure is significantly different in that the anisotropy energy is negative leading to an easy plane (001) and a unique hard axis [001] perpendicular to it. Since the force that a FSMA can exert is proportional to the anisotropy energy one possible avenue of development would be to try to find a method of increasing the anisotropy energy. However the low twinning stress

seems to be related to the 5M and 7M structures so any approach must maintain these types of martensite that exist only over a small composition range.

2.5.4 The effect of adding dopants to Ni-Mn-Ga

In the Ni-Mn-Ga system large field induced strains have been observed but there are some drawbacks, in particular the alloy is extremely brittle and a 1cm x 1cm x 3cm ingot fractures if dropped from a height of 1m or so. This makes it orders of magnitude more brittle than most metals and ultimately limits its performance in harsh environments where it may be subjected to shocks and large transient loads. Several elements, including Co, Fe and Al have been added to or substituted into the Ni-Mn-Ga system in an attempt to reduce the brittleness and produce a more functional material[24, 25]. Iron was thought to be promising and has been added to several alloys in the hope that it would increase the saturation magnetization and Curie temperature of the resulting alloy[26-29]. In these studies an increase in saturation magnetization and Curie temperature was noted but the substitution of Fe for Mn resulted in the suppression of the martensitic transition temperature. A field induced strain of ~1.2% was also observed in $\text{Ni}_{52}\text{Mn}_{16}\text{Fe}_8\text{Ga}_{24}$.

The shape memory effect has also been found to occur in Ni-Mn-Co-Ga[24, 30] in which the substitution of Co for Mn resulted in a rapid increase of the transformation temperature to 525K with the curie temperature left largely unaffected. When Co was substituted for Ni however the transformation

temperature decreased steadily from 318K to 305K at 5% substitution. The Curie temperature also increased from 354K to 365K as well. This suggests that the position of the Co atoms makes a very significant difference to both the transformation temperature and the Curie temperature.

2.6 The Ni-Fe-Ga system

The ferromagnetic shape memory effect has been shown to occur in alloys of Ni-Fe-Ga[31-33] which can be considered a complete substitution of Fe for Mn. However an adjustment of the composition is required to create an alloy with a transformation temperature close to room temperature. This results from the empirical relationship of transformation temperature to the valence electron per atom ratio that shows the ideal ratio is around 7.7 for a room temperature transformation[34].

It has been reported that these alloys also undergo a $L2_1 \rightarrow B2$ order-disorder transition at 970K in much the same way as the Ni-Mn-Ga alloys[35, 36]. The B2 structure is BCC with no long range ordering of the elements, whereas the $L2_1$ structure possesses long range order of the elements at the body centre which is equivalent to the Heusler structure. The other significant factor for the possibility of the FSME is the presence of modulated martensite phases which lower the twinning stress by an unknown mechanism. In Ni-Fe-Ga both 5 layer and 7 layer modulated martensites have been observed[31] so the material is considered a potential candidate for ferromagnetic shape memory applications. A field

induced strain of 175ppm was reported in a single crystal of $\text{Ni}_{54.2}\text{Fe}_{19.3}\text{Ga}_{26.5}$ and this strain was attributed to the field induced movement of twin boundaries. The movement of twin boundaries was observed on application of an external stress which has produced an elongation of up to 12.5% in a $\text{Ni}_{54}\text{Fe}_{19}\text{Ga}_{27}$ alloy. This does show that the material exhibits the conventional shape memory effect and it has the other ingredients necessary for the ferromagnetic shape memory effect so should be a good candidate.

However most of the alloys investigated so far, have transition temperatures well below room temperature and have a significant proportion of a face centred cubic structure present as shown by XRD. It is thought that the presence of an FCC phase both suppresses the martensitic transition temperature and impedes the movement of any twin boundaries formed in the martensite. One possible method of producing single phase Ni-Fe-Ga is through melt-spinning because the rapid cooling rate of 10^6K/s prevents formation of an FCC phase. Unfortunately the resultant material is likely to need some heat treatment in order to increase the atomic order and relax the cast-in stresses which would inhibit any shape memory effect that would otherwise be apparent.

Another potential problem is that the magnetocrystalline anisotropy energy at room temperature is a little smaller than that of Ni-Mn-Ga so the driving force of twin boundary motion is not as strong and may not overcome defects and pinning sites in the crystal. This is mainly a result of the lower Curie temperature, T_c .

(310K) of Ni-Fe-Ga alloys with a room temperature martensitic transition. The anisotropy energy decreases rapidly in the vicinity of T_c to a point where it is no longer large enough to facilitate twin boundary motion. It may be possible to improve these properties of Ni-Fe-Ga by adding dopants to the alloy and this could lead to functional Ni-Fe-Ga ferromagnetic shape memory alloys.

2.7 The Co-Ni-Ga system

A martensitic transformation close to room temperature has been reported in Co_2NiGa [37, 38] which is also ferromagnetic. These alloy compositions were chosen to give an $\frac{V_e}{a}$ ratio >7.3 similar to the functional Ni-Mn-Ga alloys. A highly twinned structure, necessary for the shape memory effect is observed in the martensitic phase of Co_2NiGa . It also displays an increasing transformation temperature with increasing annealing time at 1123K as a result of the increasing atomic order and homogeneity. At the time of writing no field induced strain data has been published for Co-Ni-Ga however and it is yet to be proven as a ferromagnetic shape memory alloy.

2.8 Thin Films

Thin films of shape memory materials are particularly attractive for use in micro electro mechanical systems (MEMS) devices if they can be fabricated with similar properties to those observed in the bulk samples. Various attempts have been made to produce thin films of Ni-Mn-Ga by sputtering and pulsed laser

deposition with varying degrees of success. This thesis focuses on the production of thin films of Ni-Fe-Ga by sputtering but the work done on Ni-Mn-Ga films is important and is discussed below.

The growth temperature is of particular importance, especially with certain substrates such as silicon. Too low a temperature and the film is amorphous or nanocrystalline and does not exhibit any shape memory effect which is highly dependent on the crystal structure and long range atomic order. The film would also have large internal stresses that also inhibit the shape memory effect. On the other hand if the temperature is too high then two potential problems occur. Firstly at elevated temperatures the adsorbed elements may begin to evaporate in the low pressure environment of the deposition chamber, in particular the Gallium content in the film is lowered and to a lesser degree the Manganese content is also reduced. Nickel and Iron have a much lower vapour pressure at these temperatures and are less susceptible to this process. The second problem occurs at deposition temperatures in excess of 600°C where silicon diffuses into the film from silicon substrates and it may be possible for a silicide phase to form[39] which would completely destroy the intended properties of the shape memory film. There is an ideal deposition temperature in the region of 200°C – 600°C in which a large grained polycrystalline film is grown without any diffusion of the substrate into the deposited film. One of the aims of this research is to investigate this and find the optimum temperature for deposition of Ni-Fe-Ga films.

2.8.1 Sputtered Films

Prior to this work only a few papers had been published relating to thin films of ferromagnetic alloys concentrating solely on Ni-Mn-Ga[40]. Ni-Mn-Ga films sputter deposited onto PolyVinylAlcohol (PVA) substrates have been shown to exhibit the ferromagnetic shape memory effect[41]. These films of $\sim 5\mu\text{m}$ thickness were deposited at 323K and then removed from the substrate which dissolves in hot water. They then underwent post growth heat treatment at 1023K for 10 hours in order to crystallize the film and improve the atomic ordering such that the ordered Heusler phase formed, without which the shape memory effect is unlikely to be observed. They were then heat treated at 673K for various times whilst being constrained in a 4mm diameter tube. The resulting coiled films were then observed to uncoil as they were heated through the transition temperature. The strain was estimated from the radius of curvature to be $\sim 0.1\%$. It should also be noted that an increase in the strain was observed in a film with a longer aging time (10 hours as opposed to 4 hours). They were also shown to exhibit a strain of the order of 0.1% on the application of an applied magnetic field of 5T with the film beginning to strain at 2T, a much larger field than the 0.2-0.4T activation field of the bulk Ni-Mn-Ga.

Thin films of Ni-Mn-Ga were sputter deposited onto single crystal silicon(001) substrates[42]. A transition temperature of 500°C has been observed. This is significantly higher than in bulk Ni-Mn-Ga and is probably due to the clamping

effect of the substrate. The optimal growth temperature range for films on silicon is shown to be 300-350°C, with films deposited at lower temperature being non-magnetic due to an amorphous and disordered structure. At higher deposition temperatures a cubic silicide ($\text{Mn}_{12}\text{Ni}_4\text{Si}_3$) was formed leading to the film being non magnetic and this prevented the formation of the shape memory phase.

2.8.2 Pulsed Laser Deposited films

Ni-Mn-Ga films have been deposited onto glass, silicon, GaAs and single crystal Ni-Mn-Ga using pulsed laser deposition (PLD) [43-48] to explore the properties of these low dimensional structures with the aim of producing ferromagnetic shape memory alloys suitable for micro devices. Most films are polycrystalline in nature and as a result do not approach the 10% strain achieved in bulk single crystals. A strain of 0.1% has been demonstrated in a film partially removed from the substrate.

Films of ~300nm thickness deposited onto a single crystal of Ni-Mn-Ga at a temperature of between 40°C and 100°C showed the shape memory effect on cooling through the martensitic transition temperature. The deposition temperature was chosen between the Curie temperature and the martensitic transition temperature so the crystal was in the austenitic phase during film deposition. Although this experiment demonstrated the shape memory effect for pulsed laser deposited films it is not particularly useful to deposit a thin film onto

a single crystal of the same material. The effect must be demonstrated with other substrates to be useful for practical applications.

Ni-Mn-Ga films deposited by PLD onto a GaAs substrate[49] show a granular rough surface structure indicative of there being a chemical reaction between substrate and deposited film. This can be prevented by the prior deposition of an inert lattice matched buffer layer which keeps the film and GaAs substrate separated by a few nm. The shape memory effect was not demonstrated in these films

2.9 Modelling the ferromagnetic shape memory effect

The large magnetic field induced strains in ferromagnetic shape memory alloys are believed to originate from a process of twin boundary motion as opposed to magnetostriction. The field dependent strain shows a large linear component in contrast to the quadratic dependence that is characteristic of magnetostrictive strains. In 1998 O'Handley proposed a phenomenological model which described the process of twin boundary motion[50]. This model accounts for the linear dependence of the strain and also describes the characteristics close to saturation.

The model treats the material as having only two variants and incorporates the Zeeman energy of each variant, the elastic energy and the effect of finite anisotropy energy. The geometry of the model is shown in Figure 2.3

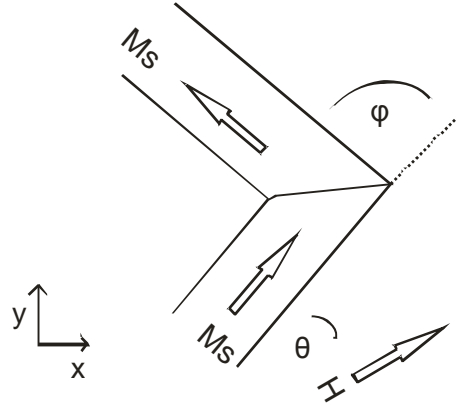


Figure 2.3 The mechanism for twin boundary motion showing the orientation of the variants and the applied field. The twin boundary moves vertically in the figure, converting one twin variant into the other.

In the case of strong anisotropy where it can be assumed that the applied field does not rotate the moments away from the c-axis the free energy, g of the system can be represented as the sum of magnetic and elastic energies which gives

$$g = -M_s H [f_1 \cos \theta + f_2 \cos(\theta + \varphi)] + \frac{1}{2} C e_0^2 [f_1^2 + f_2^2 + 2f_1 f_2 \cos \varphi] \quad \text{Eq. 2.2}$$

where f_1 and f_2 represent the fractions of the twin variants, C is an elastic stiffness coefficient and e_0 is the transformation strain. The coefficient C incorporates elastic energies resulting from defects, pinning sites and also external stress which may be applied. The free energy, g can be minimized to give the fraction of each variant under the action of a magnetic field. The resulting field induced strain in the x and y directions is given by

$$\varepsilon_x = \frac{e_x}{e_0} = \frac{\sin \varphi}{2(1 - \cos \varphi)} \left[(1 - \cos \varphi) - \left[(\cos \theta - \cos(\theta + \varphi)) \frac{M_s H}{C e_0^2} \right] \right] \quad \text{Eq. 2.3}$$

$$\varepsilon_y = \frac{e_y}{e_0} = \frac{1}{2} \left[(1 + \cos \varphi) + \left[(\cos \theta - \cos(\theta + \varphi)) \frac{M_s H}{C e_0^2} \right] \right] \quad \text{Eq. 2.4}$$

It is clear that these equations produce a linear field dependence of strain. They are a good approximation of the strain in Ni-Mn-Ga alloys in the low field region. The approximation of strong anisotropy breaks down as the field becomes large and the model deviates from experimental data at high fields.

In order to model the effect of finite anisotropy another term must be added to the free energy balance to describe the effect of magnetization rotation in the twin variants. A simpler geometry is used in this case, the important difference is that the field is along the c-axis of one of the variants and the twins are at 90° to each other. This simplifies the description of magnetization rotation because only the one variant shows this effect. The geometry is shown in Figure 2.4.

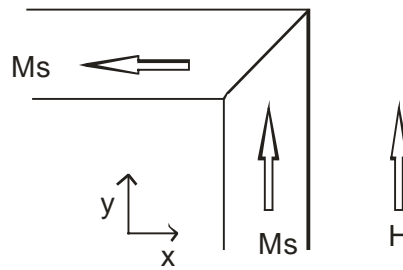


Figure 2.4 Geometry for the case of finite anisotropy energy

The equation for the free energy including the magnetic anisotropy in the unfavorably orientated variant is then

$$g = -(f_1 + f_2 \cos \psi) M_s H + \frac{1}{2} C e_0^2 \left(\frac{1}{2} + 2\delta f^2 \right) + f_2 K_u \cos^2 \psi \quad \text{Eq. 2.5}$$

where δ^* is the fractional displacement of the twin boundary and K_u is the anisotropy energy. This energy is minimized with respect to δ^* to give the strain and magnetization as a function of applied field.

$$\varepsilon_x = \frac{1}{2} \left[1 - \frac{HM_s}{Ce_0^2} \left(1 - \frac{M_s H}{4K_u} \right) \right] \quad \text{Eq. 2.6}$$

$$\varepsilon_y = \frac{1}{2} \left[1 + \frac{HM_s}{Ce_0^2} \left(1 - \frac{M_s H}{4K_u} \right) \right] \quad \text{Eq. 2.7}$$

These equations describe linear behaviour only at low fields, at which they resemble the approximation of infinite anisotropy. As the field increases the moments begin to rotate away from the easy axis in the variant orthogonal to the field direction leading to a breakdown of the approximation and a reduction in the rate of increase of strain. In some cases the strain may even reduce at very high fields because rotation of the moment vector reduces the Zeeman energy difference between variants while the elastic energy which this works against remains unchanged. This encompasses the high field non linear behavior of FSMA that has been observed experimentally. It does not however describe the non-linear behaviour observed at low fields but this is generally attributed to the fact that there are many more than two twin orientations in a real material. The effect of pinning sites and defects also tends to reduce the expected strain at low fields.

The maximum work that can be done by a shape memory alloy can be estimated from this model by taking the stress strain product which gives the work output, W as

$$W = \frac{M_s^2 H^2}{4C e_0^2} \left(1 - \frac{M_s H}{4K_u} \right) \quad \text{Eq. 2.8}$$

This gives an idea of the important properties of a shape memory alloy that are needed to maximize the energy available for use in an actuator. This model shows that energy output is maximized by having a large saturation magnetization coupled with a large anisotropy energy. A low value for C , which describes the elastic energy is also necessary because the force available is generally quite small and when the force required to overcome internal defects is minimised there is a greater force available to do work against an external stress. Interestingly the work output is not maximized in materials with very large transformation strains because they generally have lower anisotropy energy.

The optimum field direction for maximum field induced strain is calculated using the model with the large anisotropy approximation. Ni-Mn-Ga has twins at approximately 90° to each other and in this case maximum strain is obtained with the applied field at 45° to the easy axis of both variants. In other words maximum strain is obtained with the field orientated along the axis of the twin boundary which is a little counter intuitive but a very important result.

2.10 References

- [1] K. Otsuka and C.M.Wayman, "Shape Memory Materials," Cambridge University Press, 1999, pp. 44.
- [2] L. Straka, O. Heczko, and K. Ullakko, "Investigation of magnetic anisotropy of Ni–Mn–Ga seven-layered orthorhombic martensite " *J. Magn. Mater.*, vol. 274-276, pp. 2049-2050, 2004.
- [3] P. Mullner and K. Ullakko, "The force of a Magnetic/Electric field on a Twinning Dislocation," *Phys. stat.sol.*, vol. 208, pp. R1, 1998.
- [4] L. Straka and O. Heczko, "Magnetic anisotropy in Ni-Mn-Ga martensites," *J.Appl.Phys*, vol. 93, pp. 8636, 2003.
- [5] R. C. O'Handley, S. J. Murray, M. Marioni, H. Nembach, and S. M. Allen, "Phenomenology of giant magnetic-field-induced strain in ferromagnetic shape memory materials," *J. Appl. Phys*, vol. 87, pp. 4712, 2000.
- [6] S. Besseghini, M. Pasquale, F. Passeretti, A. Sciacca, and E. villa, "NiMnGa polycrystalline magnetically activated shape memory alloy: A calorimetric investigation," *Scripta. Mater*, vol. 44, pp. 2681-2687, 2001.
- [7] S. Jeong, K. Inoue, S. Inoue, K. Koterazaawa, M. Taya, and K. Inoue, "Effect of Magnetic field on martensite transformation in a polycrystalline Ni₂MnGa," *Mater. Sci. Eng.*, vol. A359, pp. 253-260, 2003.
- [8] P. Mullner, V. A. Chernenko, and G. Kostorz, "Stress induced twin rearrangement resulting in change of magnetisation in a Ni-Mn-Ga ferromagnetic martensite," *49*, pp. 129-133, 2003.

- [9] K. Ullakko, J. K. Huang, C. Kantner, and R. C. O'Handley, "Large magnetic-field-induced strains in Ni₂MnGa single crystals," *Appl. Phys. Lett*, vol. 69, pp. 1966, 1996.
- [10] O. Heczko, A. Sozinov, and K. Ullakko, "Giant field-induced reversible strain in magnetic shape memory NiMnGa alloy," *IEEE Trans. Mag.*, vol. 36, pp. 3266-3268, 2000.
- [11] A. Sozinov, A. A. Likhachev, N. Lanska, and K. Ullakko, "Giant magnetic-field-induced strain in NiMnGa seven-layered martensitic phase," *Appl. Phys. Lett*, vol. 80, pp. 1746, 2002.
- [12] V. V. Runov, Y. P. Chernenkov, M. K. Runova, V. G. Gavriljuk, and N. I. Glavatska, "Study of Phase transitions and mesoscopic magnetic structure in Ni-Mn-Ga by means of small angle polarised neutron scattering," *Physica B*, vol. 335, pp. 109-113, 2003.
- [13] V. A. Chernenko, "Compositional instability of b-phase in Ni-Mn-Ga alloys" *Scripta. Mater*, vol. 40, pp. 523-527, 1999.
- [14] T. Castan, A. Planes, and A. Saxena, "Modulated phases in multi-stage structural transformations," *Phys. Rev. B*, vol. 67, pp. 4113, 2003.
- [15] C. Jiang, Y. Muhammad, L. Deng, W. Wu, and H. XU, "Composition dependance on the martensitic structures of the Mn rich NiMnGa alloys," *Acta. Mater.*, vol. 52, pp. 2779-2785, 2004.
- [16] M. A. Marioni, R. C. O'Handley, S. M. Allen, S. R. Hall, D. I. Paul, M. L. Richard, J. Feuchtwanger, B. W. Peterson, J. M. Chambers, and R.

Techapiesancharoenkij, "The ferromagnetic shape-memory effect in Ni-Mn-Ga," *J. Magn. Magn. Mater.*, vol. 290, pp. 35-41, 2005.

[17] A. Vasilev, A. Bozhko, V. Khovailo, I. Dikshtein, V. Shavrov, S. Seletskii, and V. Buchelnikov, "Structural and magnetic phase transitions in shape memory alloys $Ni_{2+x}Mn_{1-x}Ga$," *J. Magn. Magn. Mater.*, vol. 196-197, pp. 837-839, 1999.

[18] S. J. Murray, M. Marioni, P. G. Tello, S. M. Allen, and R. C. O'Handley, "Giant Magnetic-field-induced strain in Ni-Mn-Ga crystals: experimental results and modelling," *J. Magn. Magn. Mat.*, vol. 226-230, pp. 945-957, 2001.

[19] N. Lanska, O. Soderberg, A. Sozinov, Y. Ge, K. Ullakko, and V. K. Lindroos, "Composition and temperature dependence of the crystal structure of Ni-Mn-Ga alloys," *J. Appl. Phys.*, vol. 95, pp. 8074-8078, 2004.

[20] N. Glavatska, G. Mogylny, I. Glavatskiy, and V. Gavriljuk, "Temperature stability of martensite and magnetic field induced strain in Ni-Mn-Ga," *Scripta. Mater.*, vol. 46, pp. 605-610, 2002.

[21] S. J. Murray, M. Marioni, S. M. Allen, and R. C. O'Handley, "6% magnetic-field-induced strain by twin-boundary motion in ferromagnetic Ni-Mn-Ga," *Appl. Phys. Lett.*, vol. 77, pp. 886-888, 2000.

[22] R. Tickle and R. D. James, *J. Magn. Magn. Mater.*, vol. 195, pp. 627, 1999.

[23] L. Straka, O. Heczko, and K. Ullakko, *IEEE Trans. Mag.*, vol. 38, pp. 2835, 2002.

[24] A.A.Cherechukin, T.Takagi, H.Miki, M.Matsumoto, and M.Ohtsuka, "Influence of three dimensional transition elements on magnetic and structural phase transitions of NiMnGa alloys," *J. Appl. Phys.*, vol. 95, pp. 1740, 2004.

- [25] Y. Suto, Y. Imano, N. Koeda, T. Omori, R. Kainuma, K. Ishida, and K. Oikawa, "Magnetic and martensitic transformations of NiMnX(X=In,Sn,Sb) ferromagnetic shape memory alloys," *Appl. Phys. Lett*, vol. 85, pp. 4358, 2004.
- [26] G.H.Wu, W.H.Wang, J.L.Chen, L.Ao, Z.H.Liu, and W.S.Zhan, "Magnetic properties and shape memory of Fe doped NiMnGa single crystals," *Appl. Phys. Lett*, vol. 80, pp. 634, 2002.
- [27] D.Kikuchi, T.Kanomata, Y.Yamaguchi, H.Nishihara, K.Koyama, and K.Watanabe, "Magnetic properties of ferromagnetic shape memory alloys NiMnFeGa," *J.Alloys cmpds.*, vol. 383, pp. 184-188, 2004.
- [28] z. H. Liu, M. Zhang, Y. T. Cui, Y. Q. Zhou, W. H. Wang, and G. H. Wu, "Martensitic transformation and shape memory effect in ferromagnetic Heusler alloy Ni₂FeGa," *Appl. Phys. Lett*, vol. 82, pp. 424-426, 2003.
- [29] X. Feng, D. Fang, and K. Hwang, "Mechanical and Magnetostrictive properties of Fe-Doped Ni₅₂Mn₂₄Ga₂₄ Single Crystals," *Chinn. Phys. Lett.*, vol. 19, pp. 1547, 2002.
- [30] K.Oikawa, T.Ota, F.Gejima, T.Ohmori, R.Kainuma, and K.Ishida, *Mater. Trans.*, vol. 42, pp. 2472, 2001.
- [31] H.Morito, A.Fujita, K.Fukamichi, R.Kainuma, and K.Ishida, "Magnetic field induced strain of NiFeGa in single variant state," *Appl. Phys. Lett*, vol. 83, pp. 4993, 2003.
- [32] Y.sutou, N.Kamiya, T.Omori, R.Kainuma, and K.Ishida, "Stress-strain characteristics in NiFeGa ferromagnetic shape memory alloys," *Appl. Phys. Lett*, vol. 84, pp. 1275, 2004.

- [33] K.Oikawa, T.Omori, R.Kainuma, and K.Ishida, "Effects of annealing on martensitic and magnetic transitions of NiFeGa ferromagnetic shape memory alloys," *J. Magn. Magn. Mater*, vol. 272-276, pp. 2043-2044, 2004.
- [34] X. Jin, M. Marioni, D. Bono, S. M. Allen, and R. C. O'Handley, "Empirical mapping of NiMnGa properties with composition and valence electron concentration," *J.Appl.Phys*, vol. 91, pp. 8222-8224, 2002.
- [35] K. Oikawa, T. Ota, T. Ohmori, Y. Tanaka, H. Morito, A. Fujita, R. Kainuma, K. Fukamichi, and K. Ishida, "Magnetic and martensitic phase transitions in ferromagnetic Ni–Ga–Fe shape memory alloys," *Appl. Phys. Lett*, vol. 81, pp. 5201, 2002.
- [36] A. Fujita, K. Fukamichi, F. Gejima, R. Kainuma, and K. Ishida, "Magnetic properties and large magnetic field induced strains in off-stoichiometric Ni-Mn-Al Heusler alloys," *Appl. Phys. Lett*, vol. 77, pp. 3054, 2000.
- [37] Y.Kisha, C.Craciunescu, M.Sato, T.Okazaki, Y.Furuya, and M.Wuttig, "Microstructures and magnetic properties of rapidly solidified CoNiGa ferromagnetic shape memory alloys," *J. Magn. Magn. Mater*, vol. 262, pp. L186-L191, 2003.
- [38] M.Wuttig, J.Li, and C.Craciunescu, *Scripta. Mater*, vol. 44, pp. 2393, 2001.
- [39] J. W. Dong, J. Q. Xie, J. Lu, C. Adelman, and C. J. Palmstrom, "Shape memory and ferromagnetic effects in single crystal Ni₂MnGa thin films," *J.Appl.Phys*, vol. 95, pp. 2593, 2004.
- [40] Y. Murakami, D. Shindo, M. Suzuki, M. Ohtsuka, and K. Itagaki, "Magnetic domain structure in Ni_{53.6}Mn_{23.4}Ga_{23.0} shape memory alloy films studied by

electron holography and lorentz microscopy," *Acta. Mater.*, vol. 51, pp. 485-494, 2003.

[41] M.Ohtsuka, M.Sanada, M.Matsumoto, and K.Itagaki, "Magnetic field induced shape memory in NiMnGa sputtered films," *Mater. Sci. Eng.*, vol. 378, pp. 377-383, 2004.

[42] J. Ahn, N.Cheng, T.Lograsso, and M.Krishnan, "Magnetic properties, Structure and shape memory transitions in Ni-Mn-Ga thin films grown by ion beam sputtering," *IEEE Trans. Mag.*, vol. 37, pp. 2141-2143, 2001.

[43] A. Hakola, O. Heczko, A. Jaakkola, T. Kajava, and K. Ullakko, "Ni-Mn-Ga films on Si, GaAs and Ni-Mn-Ga single crystals by pulsed laser deposition," *App. Surf. Sci.*, vol. 238, pp. 155-158, 2004.

[44] F. J. Castano, B. Nelson-Cheeseman, R. C. O'Handley, and C. A. Ross, "Structure and thermomagnetic properties of polycrystalline Ni-Mn-Ga films," *J.Appl.Phys*, vol. 93, pp. 8492, 2003.

[45] Hakola, A., Heczko, O., Jaakkola, A., Kajava, T., Ullakko, and K, "Pulsed laser deposition of NiMnGa thin films on silicon," *Appl. Phys. A*, vol. 79, pp. 1505-1508, 2001.

[46] P. G. Tello, F. J. Castano, R. C. O'Handley, and S. M. Allen, "Ni-Mn-Ga thin films produced by pulsed laser deposition," *J.Appl.Phys*, vol. 91, 2002.

[47] A. Hakkola, O. Heczko, A. Jaakkola, T. Kajava, and K. Ullakko, "Pulsed Laser Deposition of Ni-Mn-Ga thin films on Silicon," *Appl. Phys. A*, vol. 79, pp. 1505, 2004.

- [48] C. Y. Chung, V. A. Chernenko, V. V. Khovailo, J. Pons, E. Cesari, and T. Takagi, "Thin films of ferromagnetic shape memory alloys processed by laser beam ablation," *Mater. Sci. Eng.*, vol. 378, pp. 443-447, 2004.
- [49] Dong, J. W., Chen, L. C., Xie, J. Q., Müller, T. A. R., Carr, D. M., Palmstrøm, and C. J., "Epitaxial growth of ferromagnetic Ni₂MnGa on GaAs(001) using NiGa interlayers," *J.Appl.Phys*, vol. 88, pp. 7357-7359, 2000.
- [50] R. C. O'Handley, "Model for strain and magnetisation in magnetic shape memory alloys," *J.Appl.Phys*, vol. 83, pp. 3263-3270, 1998.

Chapter 3.....Experimental

Samples of ferromagnetic shape memory alloys were produced by the processes of melt spinning, magnetron sputtering and pulsed laser deposition. They were then characterised by various techniques including X-Ray diffraction, vibrating sample magnetometer, differential scanning calorimetry and inductively coupled plasma spectrometry. This chapter gives a description of the measurement techniques used in this research, their advantages and limitations as well as detailing the sample production methods.

3.1 Melt Spinning

The properties of rapidly quenched metallic alloys often differ enormously from those of their slowly cooled counterparts making them interesting for fundamental research and sometimes industrial applications. The process of melt spinning allows the production of ribbons of material a few mm wide and tens of microns thick, and with some materials it is possible to get pieces tens of meters long. This process was used to produce nanocrystalline ribbons of Ni-Fe-Ga and Ni-Mn-Ga which allowed the study of metastable crystal structures that are not necessarily found in slowly cooled samples. The Melt-Spinning process involves melting the metal, using an RF induction heater, and ejecting the liquid metal onto a spinning copper wheel using high pressure argon or other inert gas. A schematic of the melt spinner is shown in Figure 3.1.

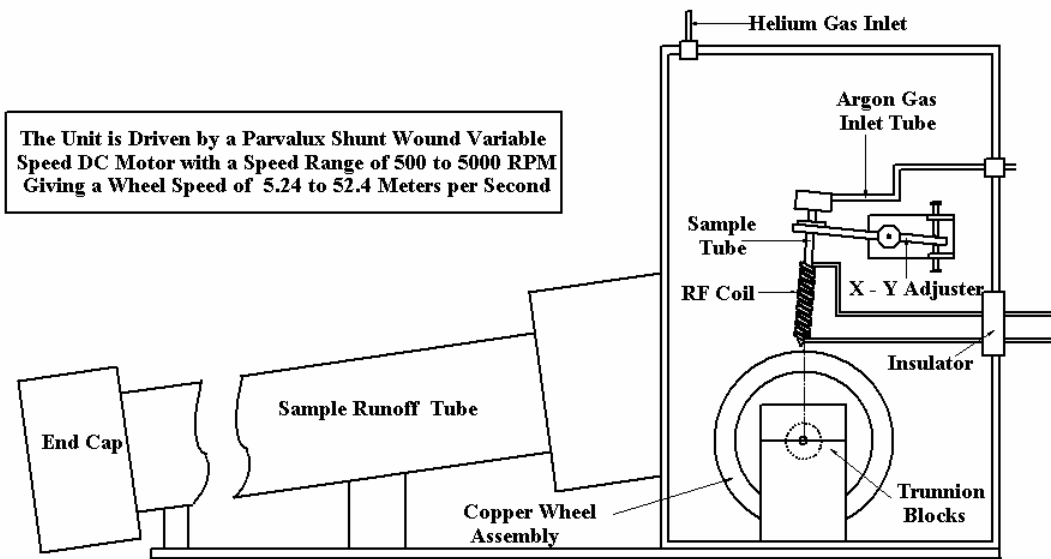


Figure 3.1 Schematic of the melt spinner

Cooling rates $> 10^6$ degrees per second are achieved resulting in amorphous or nanocrystalline ribbons being produced. This is very useful for some magnetostrictive materials as it reduces the magnetocrystalline anisotropy enabling them to produce strains at lower fields. An extra advantage for the production of shape memory alloys is the resulting ribbons are often highly textured and the rapid cooling rate quenches in the BCC phase in materials that normally form a two phase solid solution. The BCC phase is crucial to the shape memory effect, since it is only this phase that transforms into a martensite on cooling.

There are many factors which can affect the thickness of ribbon and cooling rate [1], eg. wheel speed, ejection pressure and melt temperature, the first two of which can be set with good accuracy for repeatability. The temperature of the

melt is not easily measured, so there is a great uncertainty in the ejection temperature and hitting the eject button at the right time requires experience. This may lead to significant variations in properties between samples but with practice repeatable results can be obtained. This method produces ribbons with a minimum thickness of about 20µm with varying properties. The ribbon has small grooves on one side caused by the surface roughness of the wheel. Sputtering and Pulsed Laser Deposition were investigated in order to obtain films thinner than 20µm.

3.2 Sputtering

Sputtering was first observed in 1852 by Sir W.R.Grove who discovered surface coatings in a valve in which he investigated a glow discharge. It was originally named Spluttering by Sir W.Thompson but because of a printers error became known as sputtering. It is basically the ejection of particles from the surface of a target by exposure to bombardment from heavy particles of sufficient energy, usually argon ions. The mechanism was originally thought to be the local heating of the target causing evaporation, but fundamental differences between sputtering and thermal evaporation lead to the conclusion that the mechanism is actually momentum transfer between the gas and target [2]. The following facts support this :

- The angular distribution of sputtered particles depends on the direction of the incident particles.
- Particles sputtered from single crystal targets show preferred directions
- Sputtering yields depend on both particle energy and mass
- The mean velocity of sputtered particles is much higher than that of evaporated particles.

There are three sputtering methods; DC sputtering, RF sputtering and magnetron sputtering, DC sputtering was the first to be developed and can only be used for depositing conducting materials because with insulators a charge would build up on the target and the discharge would cease. To get around this limitation RF sputtering was developed which uses an RF field, usually at 13.56MHz to excite the gas. The alternating field eliminates the problem of charge build up and allows almost any material to be sputter deposited. The deposition rates achievable are of the order of a few nms^{-1} . In order to increase the deposition rate, magnetron sputtering is used. This technique uses a magnetic field to concentrate the plasma around the target, by causing the electrons to travel in a spiral, increasing the likelihood that they will cause further ionisation. This increases the efficiency of the system allowing growth rates up to 10nms^{-1} .

One of the aims of this research was to produce sputtered thin films of a ferromagnetic shape memory alloy, all of the known ones of which are metallic and therefore conducting. This allowed conventional DC magnetron sputtering to be used.

3.2.1 The sputtering system

During the course of this work, A great deal of effort was put into rebuilding the sputtering system which arrived as a reclaimed system with no vacuum system, several serious leaks and in a poor state of repair. It required the design of several vacuum feedthroughs for water coolant and high voltage connections, the assembly of the vacuum system and interlocks as well as the design and building of a simple high voltage DC power supply for the 3" magnetron. All of the gas and water pipes were assembled, the electrical systems wired up and a protective enclosure was built to keep the high voltage parts out of reach.

A schematic of the sputtering system is shown in Figure 3.2. The main chamber is lifted on a hoist to gain access to the sample space and sputtering targets. This poses a problem of letting air into the entire chamber which drastically increases the pumping time but this could not be avoided with this chamber design.

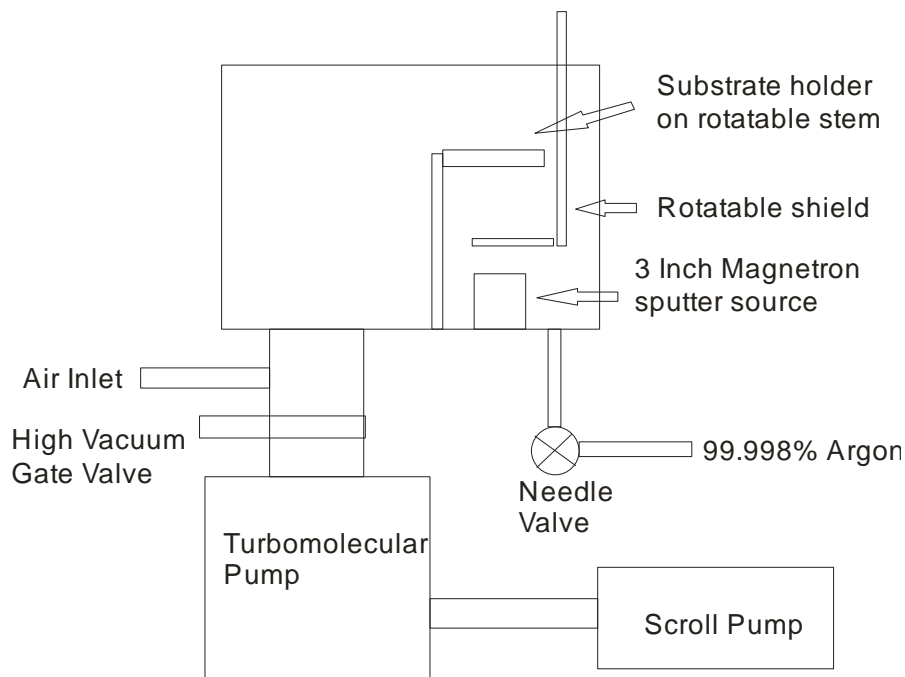


Figure 3.2 Schematic of the sputtering system used for this work

The substrate holder is rotatable from outside the chamber so that the substrate can be placed over a shield to prevent deposition when the target is being cleaned after exposure to the air. There is also a rotatable shield which can cover the magnetron during this cleaning process to further reduce unwanted deposition.

In the past, a complex arrangement of traps had to be used to prevent hydrocarbons from the pumping system backstreaming into the deposition chamber and contaminating the deposited films. This led to the choice of a scroll pump and a magnetically levitated turbo molecular pump, neither of which expose any oil to the vacuum thus eliminating this problem. Two gas bottles are required for this system, one high purity argon (99.998%) for the deposition and a nitrogen bottle to drive the pneumatically operated gate valve and to bring the

chamber back to atmospheric pressure after deposition. The Argon line is kept continuously pressurised to 55psi at all times to prevent any air getting into the line in case of small leaks in the system.

The magnetron is powered by a custom built power supply (Figure 3.3) that employs a step up transformer (110V -> 660V) which is rectified to provide ~1000V DC. This is then regulated by a power MOSFET acting as a simple linear regulator. The MOSFET gate is controlled by a feedback loop that senses the current and compares it with the set point thus providing a simple constant current power supply which provides 1000V to strike the discharge and goes quickly into current control. There is a series resistor that limits the surge current to 2A at the strike condition and in the event of a failure of the pass transistor. A separate digital voltage and current meter in line with the cable connecting the magnetron to the power supply allows power measurements to be made.

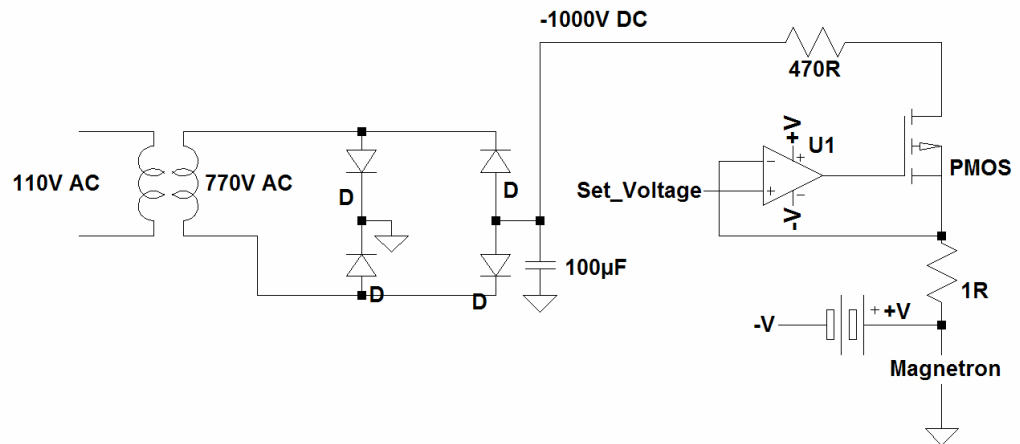


Figure 3.3 Circuit diagram of the custom built magnetron power supply

3.3 Pulsed Laser Deposition

Pulsed Laser Deposition of shape memory films was attempted as an alternative to sputtering with the aim of comparing the two processes. A Questek 2000 series Excimer laser was used for this work, running with ArF or KrF laser gas mixtures with output at 193 and 248nm respectively. These wavelengths were chosen because the metallic target reflects much less radiation at the far UV end of the spectrum and the absorption depth is also shorter leading to a lower threshold fluence for ablation. A higher energy density delivered to the ablated volume also tends to vaporise the material more efficiently and leads to fewer droplets in the deposited film.

The chamber used for this work is shown in Figure 3.4. It was constructed of aluminium with a borosilicate observation window and Quartz optical windows. The chamber was pumped with an oil diffusion pump with liquid nitrogen cold trap backed by a rotary pump which gave an ultimate vacuum of 10^{-6} mbar after overnight pumping. Not shown in this figure is a rectangular mask, 12x8mm at the output aperture of the laser that is positioned to select the central portion of the beam giving an approximate flat top intensity distribution in the beam.

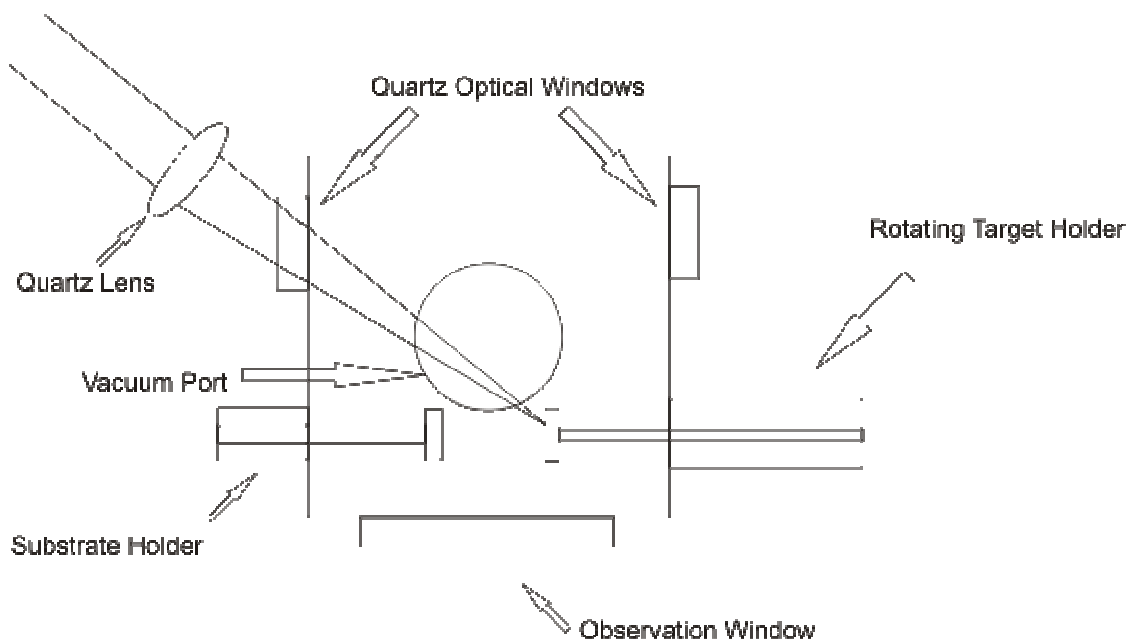


Figure 3.4 Schematic of the Laser deposition chamber. The height of the chamber is 30cm and the vacuum port is on the bottom with a cold trap directly underneath the chamber.

It is important to expose a fresh target surface for each pulse by rotating the target [3, 4]. This maintains a uniform ablation plume over many thousands of pulses and so prevents the plume wobbling as the laser drills a hole into the target. The target was rotated by a DC electric motor at approximately 30rpm. It has also been shown that rotating the substrate can also lead to a more uniform film thickness[5] but it was not possible to do this in this chamber. However, only small areas of 5mmx5mm of film were being deposited in this work so that without rotating the substrate a uniform thickness could be achieved over this area. The uniformity had a strong dependence on the target-substrate distance.

The mount for the motor allowed the target to be positioned in three dimensions within a range of approximately 10mm to provide fine adjustment of the projected image of the aperture on the target surface. The target-substrate distance was also adjustable from outside the chamber by sliding the mounting pole through an O ring mount. This was always done before pumping to prevent any minor temporary leaks as it was moved.

A Boron Nitride heater was attached to the substrate holder to provide substrate heating up to 1000°C although it was never used above 800°C.

It was recognised that oxygen inside the chamber could prove to be very problematic because Manganese oxidises readily and in the energetic

environment of the plume it could combine readily with any oxygen present. To try to minimise this problem the chamber was pumped to 10^{-2} mbar, filled with 99.998% Argon back to atmospheric pressure and then pumped to $< 10^{-5}$ mbar prior to film deposition. Some of the ablated material was deposited onto the optical window reducing the intensity of the transmitted beam as the deposition progressed. This, combined with surface roughening of the target, was enough to prevent ablation from occurring after around 50,000 pulses although deposition was usually stopped before this point. After each deposition the window was removed and cleaned with Cerium Oxide and Methanol to remove this coating.

3.3.1 Preparation of the substrate

Films were successfully deposited onto glass, silicon and silicon nitride membranes for TEM analysis. The silicon and glass substrates were cleaned prior to deposition by washing with acetone and then cleaned in a beaker of acetone placed in an ultrasonic bath for 10 minutes. This was followed by rinsing first in a dish of HPLC grade methanol and then rinsing in a dish of ultra pure distilled water, followed by blowing dry with high purity nitrogen (99.998%). This process provided a clean surface with no residue, ideal for the deposition of a thin film. The silicon nitride membranes of thickness 50nm required no preparation prior to deposition since any cleaning could damage the fragile membranes.

3.3.2 Preparation of the Target

The Ni-Mn-Ga Target was cut from a sample purchased from Adaptamat Ltd, to approximately 3mm thickness and prior to each deposition it was sanded flat using 600 Grit emery paper followed by 1200 Grit emery paper. It was polished with 3 μ m lapping paper and then cleaned in an ultrasonic bath in acetone to remove any finger grease and debris from the sanding process. It was then blown dry and mounted for the deposition process by gluing onto an SEM stub which fits into the holder.

During the first 1000 pulses or so stoichiometric transfer from target to substrate did not occur. A large increase of gallium and a deficiency of Nickel and manganese was noted after the deposition of the first films and for all subsequent films the target was irradiated for 1000 pulses before the substrate was inserted into the chamber. After the cleaning pulses the chamber had to be opened up to insert the substrate. It was filled with argon to atmospheric pressure and the substrate was inserted very quickly before pumping the chamber again. Ideally some sort of shield would be present to prevent deposition during the cleaning but it was not possible to do this within the confines of the chamber.

3.4 Vibrating Sample Magnetometer (VSM)

The VSM is a method of directly measuring the magnetic moment of a sample in a static magnetic field. In practice the static field is slowly ramped to produce the hysteresis loop. The VSM was first developed by Foner[6] in 1959. The principle

of operation is that the sample is mechanically vibrated in a static field and the oscillating movement of the sample induces an oscillating voltage in a set of pickup coils placed close to the sample. In a standard VSM with electromagnets the vibration is usually vertical, perpendicular to the field direction. Another geometry with the vibration along the field direction has also been developed primarily for use with superconducting magnets but since the transverse geometry was used for all of the measurements this will be the focus of this discussion.

There are two main objectives that must be followed when designing a pickup system for a VSM[7], these are:

- 1) The coils must not respond to external interfering fields. i.e the effective area presented to external fields must be as close to zero as possible
- 2) The pickup system must be firmly attached to the electromagnet so that they do not vibrate with respect to the applied magnetic field which would produce a large spurious response. This implies that there must be very good isolation between the vibrating sample and the pickup system.

There are several possible pickup coil geometries in use for VSM's and the VSM used for this work uses the Mallinson geometry [8], developed in 1966. This geometry is ideal for the confined space between the magnet poles and provides good sensitivity. This is especially useful when a cryostat or furnace is in use

because space is very tight in these circumstances. Its only disadvantage is its sensitivity to fluctuations in the applied field.

The induced voltage is proportional to both the magnetic moment of the sample and the vibration amplitude so the magnitude of vibration has to be tightly controlled to maintain accuracy. This is done by utilising a pair of capacitor plates, one of which is attached to the vibrating rod to provide feedback to the controller which can then accurately set the amplitude independent of loading effects such as sample and sample rod mass.

The sample position relative to the coils affects the sensitivity and indeed this is very important in the calibration of the VSM, especially if the absolute magnitude of the moment is desired. At the saddle point, located at the exact centre of the pickup coils the sensitivity to position is at a minimum and this is the best place to put the sample for repeatable results. The VSM is mounted on a tiltable stage that allows the sample position to be precisely set in all three dimensions. The procedure for setting the saddle point and calibrating the VSM is as follows:

Put the nickel calibration sample in the holder and set a static field of 4000Oe.

Adjust the height for maximum detected moment.

Adjust the y axis position (perpendicular to applied field) for maximum detected moment.

Adjust the x axis position (parallel to applied field) for minimum detected moment.

Use a screwdriver to adjust the sensitivity to set the moment to the calibration value written on the sample bottle.

The VSM is a Lakeshore 7300 series connected to a computer via a GPIB bus for control and data capture. The electromagnet can produce fields of 10000Oe when powered from a DC generator which has its own controller that was built during the course of this work. This is all controlled by a feedback loop incorporating a Hall probe in the sample space which allows direct setting of the applied field. The generator produces some current noise and a ripple current which reduces the sensitivity of the instrument by an order of magnitude. With this generator, moments of $\sim 10^{-4}$ emu can be resolved compared with $\sim 10^{-5}$ emu with the solid state power supply. For fields < 4000 Oe a solid state power supply can be used which has much lower noise, increasing the sensitivity somewhat but it is limited to $\pm 40V$ and $\pm 4A$.

3.5 X-Ray Diffraction (XRD)

X-Ray diffraction using a Siemens D5700 Diffractometer was the primary method of structural analysis carried out in this work. . This instrument performs “2 theta” scans with an angular step size of 0.02° and a 2 second dwell time at each angular position to provide sufficient sensitivity. Ribbon samples were stuck onto a glass microscope slide with double sided tape. The slide was then assembled with the diffractometers sample holder so as to ensure each sample was in the same position relative to the beam. The samples created in this work were all

polycrystalline and gave a powder diffraction pattern so a one dimensional scan is sufficient to extract the structural information.

Braggs law was used to find the lattice spacings and fit a structure to the sample.

$$n\lambda = 2d \sin \theta \qquad \text{Eq. 2.9}$$

where n is an integer, d is the spacing between lattice planes, λ is the X-Ray wavelength and θ is the angle of incidence relative to the plane normal.

An important factor that must be considered with ordered Heusler alloys is that not all atoms scatter X-Rays with equal efficiency which leads to extra peaks appearing in the diffraction pattern. The reason for this is straightforward. X-Rays are scattered by the interaction with electrons orbiting the atom, therefore the scattering efficiency is approximately proportional to the number of electrons orbiting the atom. This approximation breaks down as the atom size increases and waves scattered from opposite sides of the atom begin to show a phase shift that reduces the intensity of the scattered beam.

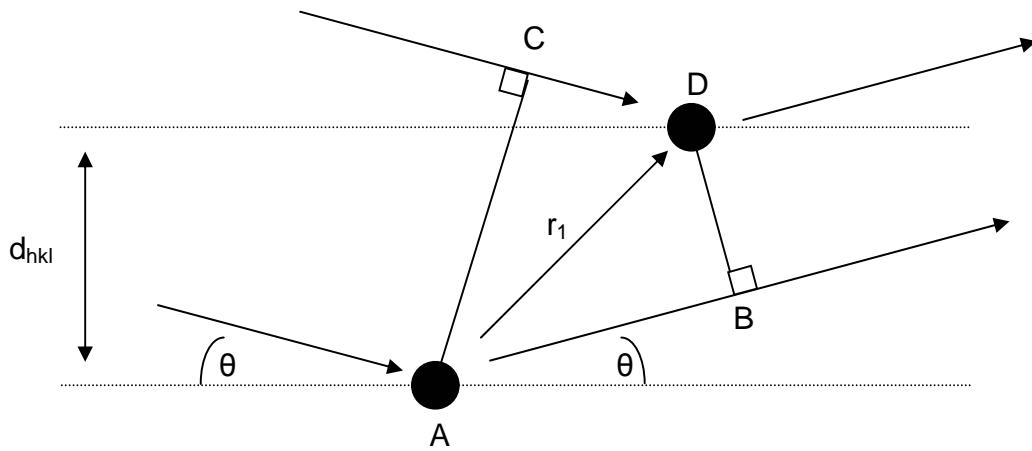


Figure 3.5 Atoms at A & D scatter incoming X-Rays with scattering factors f_1 and f_2 respectively. The total scattering at each Bragg angle can then be determined.

The scattering factor for a 2 atom unit cell shown in Figure 3.5 can be calculated to take into account the different scattering factors of the 2 atoms. The path difference of waves scattered from the 2 atoms can be represented by

$$(PD) = AB - CD = r_1 s_i - r_1 s_s = r_1 (s_i - s_s) \quad \text{Eq. 2.10}$$

where s_i and s_s are the incident and scattered X-Ray vectors. It follows then that r_1 can be written as the sum of its components along each axis and because the Bragg condition is satisfied $(s_i - s_s)$ can be written in terms of λ and d_{hkl} .

$$r_1 = u_1 \underline{a} + v_1 \underline{b} + w_1 \underline{c} \quad \text{Eq. 2.11}$$

$$(s_i - s_s) = 2 \sin \theta = \frac{\lambda}{d_{hkl}} \quad \text{Eq. 2.12}$$

In a system with orthogonal axes this leads to the following equations for the path difference and relative phase angle.

$$(PD) = \lambda(u_1\underline{a} + v_1\underline{b} + w_1\underline{c}) \quad \text{Eq. 2.13}$$

$$(\text{Phase angle}) = \frac{2\pi}{\lambda}(PD) = 2\pi(u_1\underline{a} + v_1\underline{b} + w_1\underline{c}) \quad \text{Eq. 2.14}$$

The resulting structure factor for any number of atoms can then be found by adding the atomic contributions using a vector phase diagram, which can be represented mathematically by the following

$$F_{hkl} = \sum_{n=0}^{n=N} f_n \text{Exp}[2\pi j(u_n\underline{h} + v_n\underline{k} + w_n\underline{l})] \quad \text{Eq. 2.15}$$

where N is the number of atoms in a unit cell, f_n is the scattering factor for the n^{th} atom and u_n, v_n, w_n are the positions of the n^{th} atom within the unit cell. It is the differing values of f_n for the different atoms in a Heusler alloy that results in F_{hkl} being non zero for certain cases and thus giving extra peaks. The intensity of Bragg reflection is given by $F_{hkl} \square F_{hkl}^*$ and it should also be noted that f_n will be a function of the angle of incidence of the X-Ray beam as well as the atomic number.

3.6 Transmission electron microscopy (TEM)

TEM is an extremely useful tool for imaging the microstructure of materials and thin films in particular. It is possible with a high resolution TEM (HRTEM) to obtain pictures showing the individual atomic planes. In contrast to scanning electron microscopy the image in TEM is formed by the electron beam passing

through the material which necessitates a very small thickness in the region of less than ~300nm. This can be achieved by mechanical and ion beam thinning of a bulk material. In this work however thin films were deposited onto 50nm thick Silicon Nitride membranes which are transparent to the electron beam and greatly reduce the preparation necessary for TEM samples.

The TEM, a JEOL 2010 was also fitted with an Energy Dispersive X-Ray Spectrometer (EDX) system which allows in-situ composition measurement of the samples with an accuracy of $\pm 1\%$. The bombardment of atoms with an energetic electron beam causes ionisation from the inner electron shells of the atom and the transition of an outer electron into the resultant vacancy produces X-ray's characteristic of that particular element. The X-rays are then detected by a Lithium doped Silicon detector which generates a pulse proportional to the energy of the X-ray photon allowing the elements to be detected in a parallel fashion with a typical scan taking around 2 minutes to give enough X-ray counts for an accurate result.

3.7 Capacitance Dilatometry

A capacitance method was chosen to measure field induced strain in the melt spun ribbons because of the high sensitivity and low stress on the sample that can be achieved. The 3 terminal capacitance method was used because it minimises the effects of stray capacitance caused by surrounding objects and

the connecting coaxial cables[9]. A schematic of the apparatus is shown in Figure 3.6.

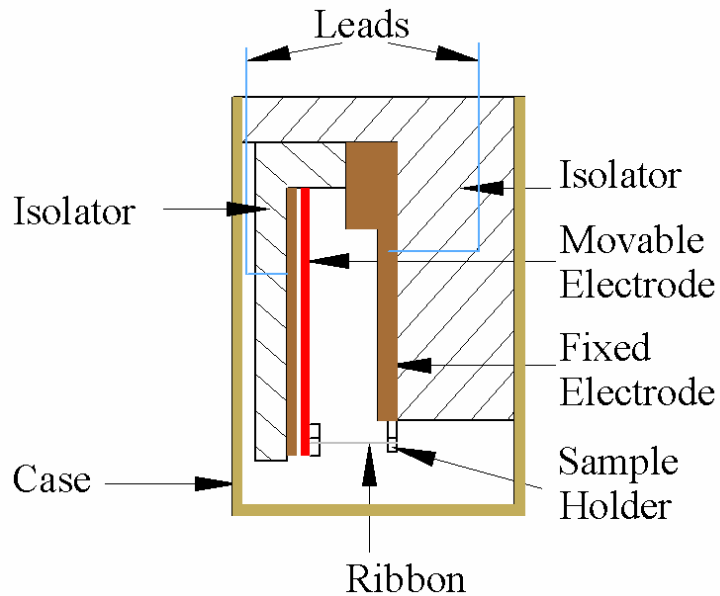


Figure 3.6 Internal structure of the capacitance cell used for measuring field induced strains in magnetic ribbons

The ribbon is clamped to a fixed point at one end and to a moveable electrode at the other. The moveable electrode is mounted on a beryllium copper leaf spring that maintains the ribbon under a small tension at all times so that the length of the sample can be accurately measured. The spring is cut and drilled and then heat treated at 230°C for 2 hours to enhance its properties. A significant problem in this research was encountered with the tensioning system in that the leaf spring underwent many iterations in order to obtain a tension lower than the blocking stress in ferromagnetic shape memory alloys. This spring exerts a force of approximately 0.08N on the ribbon corresponding to a stress of ~2MPa in a typical ribbon.

The equation for the capacitance C of the cell is

$$C = \frac{\epsilon_0 A}{d} + C_{stray} \quad \text{Eq. 2.16}$$

where d is the separation, A is the surface area of the plates, C_{stray} is the stray capacitance from the leads etc. and ϵ_0 is the permittivity of free space. The sample is attached to the movable electrode such that a change in its length, Δl produces a change in the inter electrode separation Δd which leads to

$$\Delta C = \frac{\partial C}{\partial d} \Delta d = \frac{-\epsilon_0 A}{d^2} \Delta d \quad \text{Eq. 2.17}$$

Taking C_0 and d_0 to be the initial capacitance and separation values the sensitivity can be written as

$$\frac{\partial(C/C_0)}{\partial d} = \frac{-C_0}{\epsilon_0 A} \quad \text{Eq. 2.18}$$

It is possible from this result to calibrate the capacitance cell by measuring two values of $\partial(C/C_0)/\partial d$ in units of ppm/ μm at different electrode separations. The capacitance bridge (Andeen Hagerling Model 2500) is capable of resolving changes in capacitance of less than 0.5ppm and since the capacitance cell gives approximately a 20 ppm change in capacitance for a 1 ppm change in sample length the overall sensitivity of the system should be around 0.05ppm. This is such a small change in sample length that it can become easily swamped by mechanical vibration and indeed the noise in the system limits the precision to $\pm 0.25\text{ppm}$.

In practice the stray capacitances and edge effects cannot be completely ignored and to obtain a more accurate representation of the sensitivity as a function of C_0 the sensitivity can be represented as a polynomial such that

$$\frac{\partial(C/C_0)}{\partial d} = a_0 + a_1 C_0 + a_2 C_0^2 + \dots \quad \text{Eq. 2.19}$$

If $\partial(C/C_0)$ is measured at several values of d , a calibration curve can be plotted and a polynomial fitted to the data in order to find $\partial(C/C_0)$ as a function of C_0 .

The capacitance cell was initially calibrated with a polycrystalline nickel sample that was prepared by compressing a piece of high purity (99.9%) Nickel wire in a 10 ton press to obtain a piece 0.09 x 1.5 x 8 mm. This was then annealed to relieve the stress induced by this process. Nickel has a saturation magnetostriction of 47.2ppm at room temperature[10-12] which gives the basis for the calibration of the capacitance cell. This sample was clamped into the capacitance cell and the change in capacitance measured at various values of C_0 to give a calibration curve. This curve was fitted to Eq. 2.19 in order to find the constants a_0 , a_1 and a_2 , which are

$$\begin{aligned} a_0 &= 289 \\ a_1 &= -55.30 \\ a_2 &= 7.682 \end{aligned} \quad \text{Eq. 2.20}$$

A computer program to collect the data was written in C++ using the Trolltech QT toolkit. This provided a simple graphical windows program to collect the data, graph it and save it in a space separated column format.

3.8 Magnetic Susceptibility

The magnetic susceptibility of the ribbon samples was measured using the small signal ac susceptibility technique as shown in Figure 3.7.

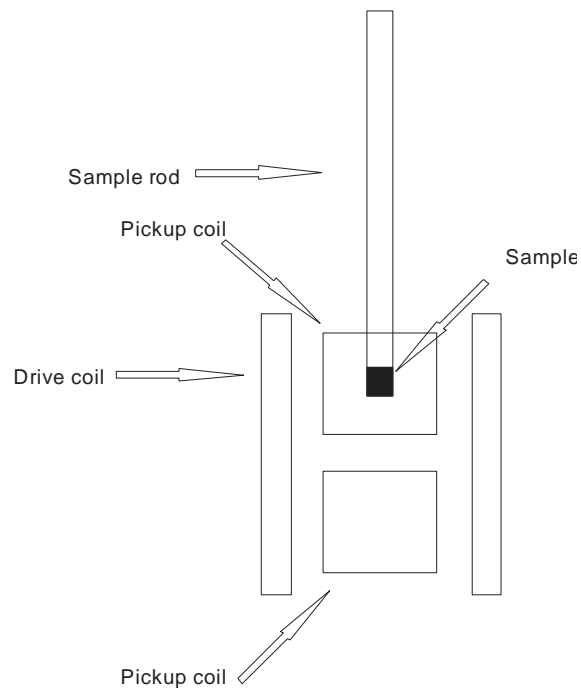


Figure 3.7 Diagram of the magnetic susceptibility measurement apparatus

The two pickup coils are wound in antiphase, connected in series and placed symmetrically inside the drive coil such that the voltage induced by the drive cancels when there is no sample inside either of the coils. The presence of the sample unbalances the pickup coils and results in a signal appearing across the

coils at the drive frequency. The apparatus was placed inside an Oxford instruments cryostat which was cooled with liquid N₂. A custom built furnace could also be used for heating above room temperature which proved useful for the samples with martensitic transition temperatures above 290K.

The drive coil is driven with a 220Hz sine wave, 1A peak current from an amplifier with current feedback so that the magnitude of the current remains constant even if the drive coil resistance changes, as it does with temperature. The pickup coil output is fed into a lockin amplifier which is locked to the drive signal frequency and has an averaging time of 3 seconds. A PT100 platinum resistance thermometer is fitted to the sample rod at the back of the flat to which the sample is attached so that a good measure of temperature can be obtained for susceptibility vs temperature curves. The output of the lock in amplifier, a field sensor and the temperature sensors were connected to digital voltmeters equipped with a GPIB interface. This allowed them to be connected to a computer and the whole apparatus was then controlled by software.

Some sensitivity problems were discovered because of the small ribbon samples that were available, typically 40-50mg of ribbon being used for each measurement. The apparatus suffered from temperature instability which in most cases caused a change in output comparable to, or greater than the output from the sample, probably as a result of eddy current loss in the metal in the surrounding cryostat. The output of the coil depended not only on the cryostat

temperature but on the cryogenic gas flow rate as well, presumably because of the different temperature gradients set up in the cryostat itself. With the Oxford Instruments cryostat it was impossible to compensate for this effect, but as some of the samples exhibited transition temperatures above room temperature the cryostat was replaced with a furnace which displayed much smaller interference and allowed measurements above room temperature to be made. This limited the measurements that could be made to only a few of the Ni-Mn-Ga samples.

3.9 References

- [1] V.I.Tkatch, A.I.Limanovskii, S.N.Denisenko, and S.G.Rassolov, "The effect of the melt-spinning processing parameters on the rate of cooling," *Mater. Sci. Eng.*, vol. A323, pp. 91-96, 2002.
- [2] D. Smith, *Thin-Film Deposition: Principles and Practice*: McGraw-Hill Professional, 1995.
- [3] E. v. Riet, C. Nilsen, and J. Dieleman, "Laser ablation deposition measurements from silver and nickel," *J.Appl.Phys*, vol. 74, pp. 2008, 1993.
- [4] A. B. Brailovsky, S. V. Gaponov, and V. I. Luchin, "Mechanisms of melt droplets and solid-particle ejection from a target surface by pulsed laser action," *Appl. Phys. A*, vol. 61, pp. 81, 1995.
- [5] N. J. Ianno and K. B. Erington, "Thin films of uniform thickness by pulsed laser deposition," *Rev. Sci. Instrum*, vol. 63, pp. 3525, 1992.
- [6] S.Foner, "Versatile and sensitive vibrating-sample magnetometer," *Rev. Sci. Instrum*, vol. 30, pp. 548-577, 1959.
- [7] C.Guy, "A simple approach to coil design for vibrating sample magnetometers," *J.Phys E. Sci. Instr.*, vol. 9, pp. 790-791, 1976.
- [8] A.Zieber and S.Foner, *Rev. Sci. Instrum*, vol. 53, pp. 1344, 1982.
- [9] *Instruction Manual, Andeen-Hangerling Model 2500 Capacitance bridge*.
- [10] E. W. Lee and M. A. Asgar, "The Magnetostriction of Nickel," *Proc. R. Soc. Lond. A*, vol. 326, pp. 73, 1971.
- [11] R. R. Briss and E. W. Lee, *Proc. Phys. Soc*, vol. 76, pp. 502, 1960.

[12] V. Madurga, A. Hernando, and M. Vasquez, "Variation of polycrystalline Ni magnetostriction with temperature up to T_c ," *J. Phys. D: Appl. Phys.*, vol. 14, pp. 913, 1981.

Chapter 4.....Results and Discussion

4.1 Melt Spun Ni-Mn-Ga

The effect of rapid quenching on Ni-Mn-Ga ferromagnetic shape memory alloys is investigated in this section. The magnetic and thermomagnetic properties are examined using a VSM fitted with an Oxford Instruments cryostat. Crystal structure is obtained from X-Ray diffraction and the effect of different heat treatments is explored in detail.

4.1.1 Sample preparation

One polycrystalline sample of Ni-Mn-Ga was obtained from Adaptamat Ltd. and four others were made at the Centre for Metallurgy and Materials at Birmingham by melting in an arc furnace under an argon atmosphere. The Adaptamat sample was available several months before the others, so it was used first and is presented before the others. The nominal composition of the four samples alloyed at Birmingham was chosen by looking at the unexplored composition region in [1] where it was expected that these compositions (samples 1,2,3,4) would exhibit the martensite phase at room temperature such that $27^{\circ}\text{C} < T_{\text{mart}} < T_c$ where T_c is the Curie temperature. Each ingot had a total mass of 20g. A small amount of Tin was also added to one of the ingots in an attempt to reduce the brittleness that all of the Ni-Mn-Ga alloys show. The composition of the alloys was determined by Inductively Coupled Plasma Mass Spectrometry (ICPMS) with an accuracy of $\pm 0.2\%$.

	Nickel	Manganese	Gallium	Tin
1	49.4(48.5)	29.1(30.3)	21.6(21.2)	
2	53.4(53.1)	26.3(26.6)	20.3(20.3)	
3	53.3(52.2)	24.9(25.0)	21.8(22.8)	
4	53.1(51.5)	26.2(25.8)	19.7(19.7)	0.9(3.0)
5 (Adaptamat)	52.1	26.5	21.3	

Table 4.1 Composition of the ingots of bulk NiMnGa as measured by

ICPMS. Nominal values are shown in brackets

Table 4.1 shows that the nominal and measured compositions of the alloys agree to within 2%. The discrepancies are likely caused by a combination of measurement error when weighing out the constituent elements and by evaporation of Manganese and Tin from the melt because of the relatively high vapour pressure of these elements. The five ingots were then broken using a 10 ton press into pieces small enough to fit into a 5mm tube for melt-spinning. They were then melt spun onto a single 20cm diameter copper roller under a flowing Helium atmosphere to produce ribbons of each composition. Various wheel speeds and ejection pressures were used to experimentally determine the conditions required to produce useful lengths of ribbon as shown in Table 4.2. The copper wheel was cleaned between each sample by a process of lightly sanding with 600 grit emery paper followed by 4um lapping paper to give a mirror finish. Finally all dust and surface contamination was removed with tissue paper soaked in acetone.

Sample No.	Wheel Speed (RPM)	Ar Injection Pressure (Psi)	Result
1.1	4000	12	Pieces < 10mm. Discoloured. The melt was probably too hot.
1.2	4000	12	Pieces < 10mm
1.3	3750	12	Pieces < 10mm
1.4	3250	12	Pieces <50mm. Silver colour with a slight gold hue.
2.1	4000	12	Pieces < 10mm
2.2	3500	12	Pieces < 10mm
2.3	3250	12	Pieces <30mm
2.4	3000	12	Pieces <30mm
2.5	2750	12	Pieces < 10mm
3.1	2750	12	Wirey pieces < 10mm
3.2	3000	12	Mostly pieces < 10mm, but a few up to 50mm
3.3	3500	12	Pieces < 10mm
3.4	4000	12	Pieces <40 mm
3.5	4500	12	Pieces < 10mm
4.1	3250	12	Pieces <40mm
4.2	4000	12	Pieces <40mm
4.3	4500	12	Pieces < 10mm
5.1	3550	12	Pieces < 30mm
5.2	4000	12	Pieces < 80mm
5.3	4500	12	Pieces < 30mm

Table 4.2 The melt spinning parameters used for sample production of the Ni-Mn-Ga ribbons

Samples of each melt spun batch were subsequently annealed in a vacuum furnace for the purpose of stress relief and recrystallisation of the ribbons. Several pieces of each sample were annealed at 400°C, 500°C, 600°C and 700°C under an argon (99.999%) atmosphere of 500mbar for 2 hours to study the effects of annealing temperature on crystal structure and magnetic properties. Initially when annealing at temperatures greater than 600°C a green oxide formed on the surface of the ribbons which then became extremely brittle and powdered when handled with tweezers. As a result of this, an anneal at 800°C was performed in quartz ampoules with a partial pressure of argon. This process was performed by Birmingham University, Metallurgy and Materials Dept. The oxidation was later found to originate from the vacuum grease on the 'o' rings at the end of the furnace which released vapour into the furnace that caused corrosion of the ribbons. The 'o' rings were replaced and all parts of the furnace were cleaned with acetone to remove any traces of grease. This reduced the problem of oxidation to an undetectable level.

4.1.2 Magnetisation

Figure 4.1 shows the Magnetisation curves of the ribbons formed from the Adaptamat ingot (sample 5.2). The as-spun sample has a low susceptibility with very low hysteresis, suggesting that magnetisation rotation is the dominant process in the magnetisation curve. Two distinct effects were visible on annealing, at 400°C there is some stress relief, shown on the magnetisation curve by the slightly increased magnetisation, but only limited recrystallisation.

The shape of this curve also suggests that there is a critical field of $\sim 300\text{kA/m}$ at which magnetisation begins to switch to the field direction. This is typical of alloys showing magnetic field induced twin boundary motion[2] and represents the point at which field induced twin boundary motion begins. This phenomenon appears to be a reversible process, suggesting that the cause is twin boundary motion acting against cast-in stresses in the material which restore the original shape on removal of the field. The higher temperature annealing increases M_s as a result of atomic rearrangement and recrystallisation, which increases the long range atomic order. It is expected to form the $L2_1$ Heusler phase that has been reported for single crystal Ni-Mn-Ga[3], but the Xray data lacked the sensitivity to detect this. The 700°C anneal shows a reduced M_s compared with 600°C , probably due to the visible oxidation suffered at this temperature.

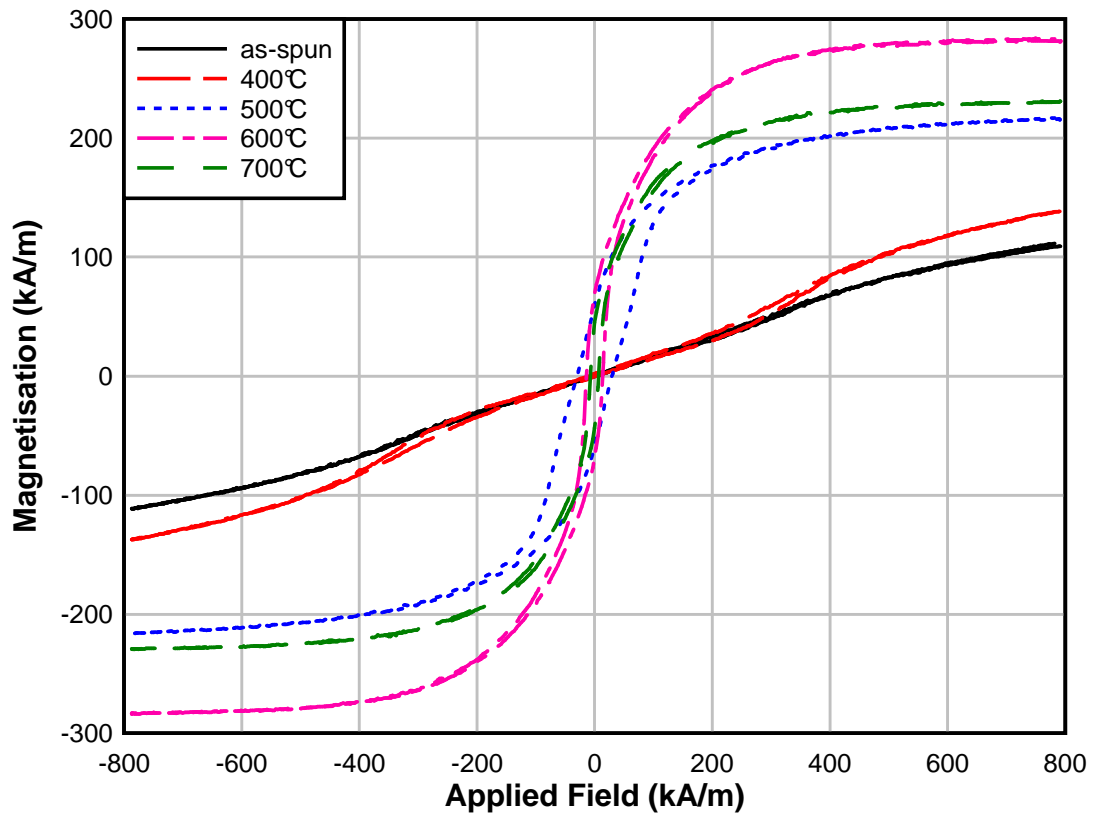


Figure 4.1 Magnetisation curves for sample 5.2 (Adaptamat) annealed at 400 – 700°C for 2 hours

The saturation magnetisation of single crystal samples of Ni-Mn-Ga has been shown to be 400kA/m and 512kA/m in the austenite and martensite phases respectively[4]. The sample annealed at 600°C has a saturation magnetisation of 290kA/m which is 27% lower than that seen in the literature for the Austenite phase. There is a measurement error of approximately $\pm 10\%$ in the above data which may account for some of the discrepancy but the difference is more likely to result from oxidation of the ribbon samples during annealing which forms paramagnetic oxides on the surface. Because the ribbons are only around 30 μm

thick it would only take a 3-4 μm thick oxide layer on each side to reduce the magnetisation by this amount.

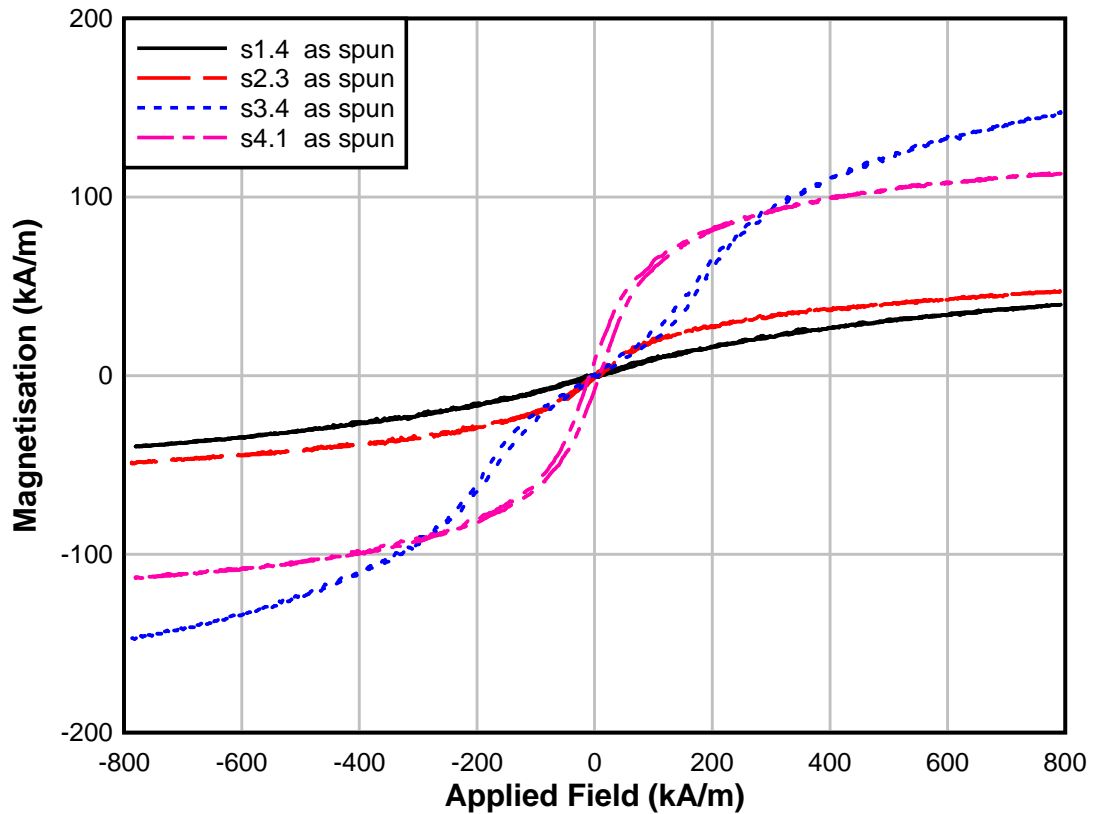


Figure 4.2 Magnetisation curves for the Ni-Mn-Ga ribbon samples in the as-spun state

Figure 4.2 shows the magnetisation curves for samples 1-4 in the as-spun state, before the subsequent annealing. It is clear that samples 1.4 and 2.3 show a similar behaviour to the Adaptamat sample with rotation of the moments being the dominant mechanism. Sample 3.4 however shows a distinctly different magnetisation curve, with the same critical field phenomena that appeared for the stress relieved Adaptamat sample. DSC subsequently confirmed that sample

3.4 is in the martensite phase at room temperature whereas the others are not. The unique features of this magnetisation curve are tentatively attributed to the onset of twin boundary motion. Sample 4.1 shows ferromagnetic behaviour similar to that expected from a soft magnetic material; it has no features that would indicate it was a shape memory alloy, a fact that is confirmed by DSC and XRD.

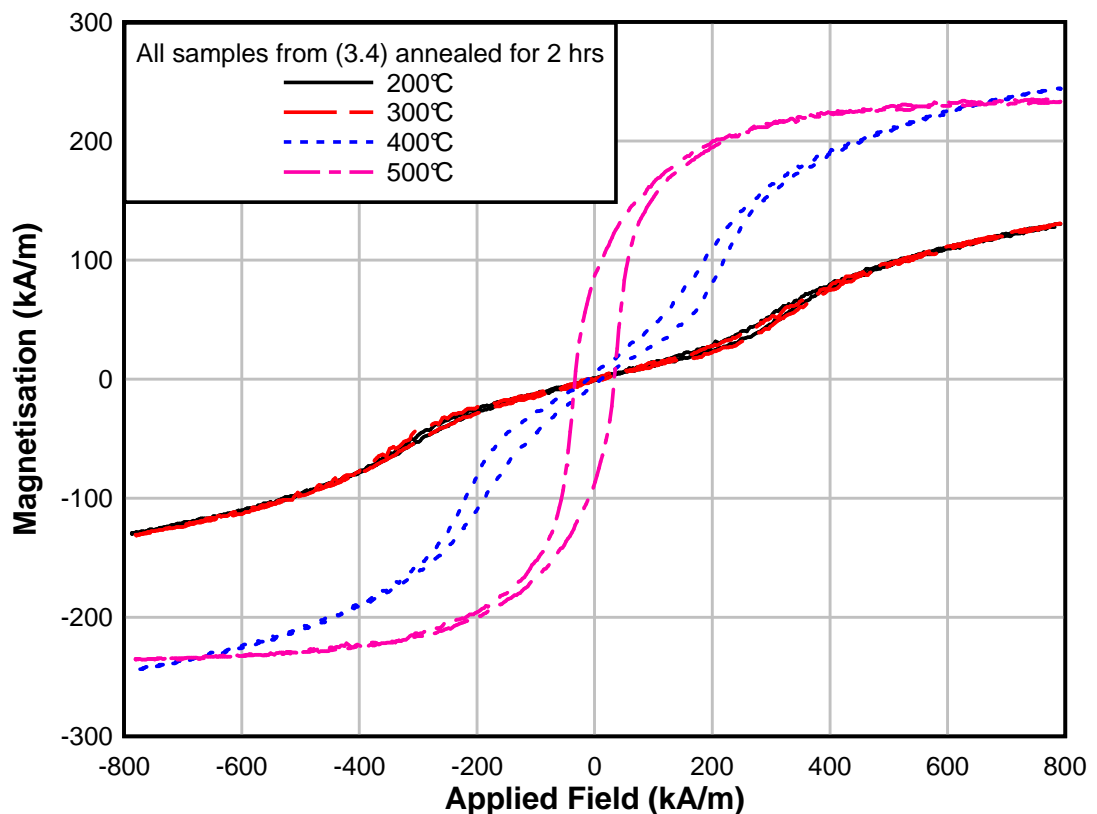


Figure 4.3 Magnetisation curves of Ni-Mn-Ga sample 3.4 showing the effect of annealing at 200°C, 300°C, 400°C and 500°C for 2 hours

Figure 4.3 shows the magnetic properties of sample 3.4 as a function of annealing temperature. It is evident that annealing temperatures $\leq 300^\circ\text{C}$ have

very little effect, with the magnetisation loop looking almost the same as for the as-spun material of sample 3.4. At 400°C there is expected to be some stress relief but little recrystallisation and this is evident in the hysteresis loop. The critical field phenomenon around 150kA/m is similar to that in the Adaptamat sample annealed at 400°C but much more pronounced with a larger hysteresis, probably as a result of the higher M_s in this sample. This phenomenon is attributed to the applied field causing twin boundary motion that is opposed by the increase in elastic energy which results from the random orientation of the crystal grains and provides the restoring force as the field is removed. It should be noted at this point that this effect, seen in the 400°C annealed ribbon of sample 3.4, is only observed in ribbons that have been shown to be in the martensite phase at room temperature and this is very similar to the magnetisation loops that show twin boundary motion in [5]. Annealing temperatures of 500°C and above result in a significant recrystallisation and a significant increase in grain size, with grains of ~5µm observed using optical microscopy. Samples annealed at 500°C or above do not show the critical field phenomenon that is evident in the sample annealed at 400°C. This is consistent with this being due to twin boundary motion, as in the samples annealed at 500°C or greater there was significant grain growth and therefore the elastic restoring force would have been much reduced and as a result once the field had moved the twin boundaries only a change in field direction to a perpendicular direction would move them again.

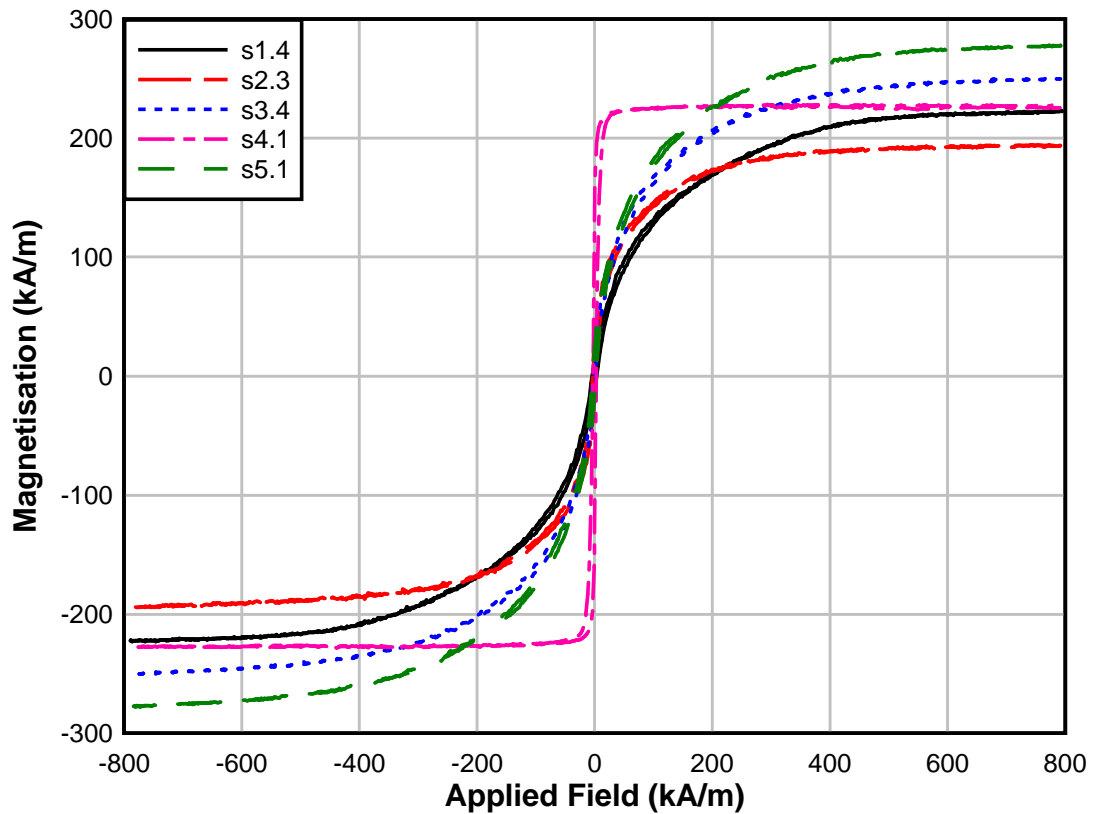


Figure 4.4 Magnetisation Curves for Ni-Mn-Ga ribbon annealed at 800°C for 12 hours

When the samples have been annealed at 800°C for 12 hours, a large degree of recrystallisation and grain growth has occurred and there is little residual stress. 800°C was chosen as the annealing temperature as it is the B2 to L21 (Heusler) transition temperature[3]. Figure 4.4 shows the hysteresis loops of the ribbons annealed at 800°C and it is evident that the saturation magnetization is increased on annealing and saturation is reached at a much lower field than in the as-cast state as a direct result of the increased atomic order and reduction of defects in the crystal lattice. Magnetisation rotation is the dominant mechanism as

evidenced by the low coercivity and hysteresis present in these loops. It is important to note here that samples 1.4, 3.4 and 5.1 were below their respective martensite transition temperatures and yet showed no sign of the critical field phenomenon seen in the corresponding samples that have been annealed at 400C suggesting that the relatively small randomly orientated crystal grains provide an elastic restoring force that the twin rearrangement works against. Sample 4.1 shows characteristics of being a soft magnetic material with low anisotropy. Subsequent DSC measurements revealed that this sample does not undergo a martensitic transition.

4.1.3 Crystal Structure

The X-Ray diffraction patterns of the as-spun ribbons are shown in Figure 4.5. It can be seen that samples 1, 4 and 5 all have a body centred cubic structure with a small amount of a face centred cubic phase present as well. The 3 large peaks at 43.5° , 63.5° and 80.3° in these samples result from the (220), (400) and (422) reflections of the BCC phase with the smaller peaks being from the FCC phase. Samples 2 and 3 however showed a more complex structure with some martensite present.

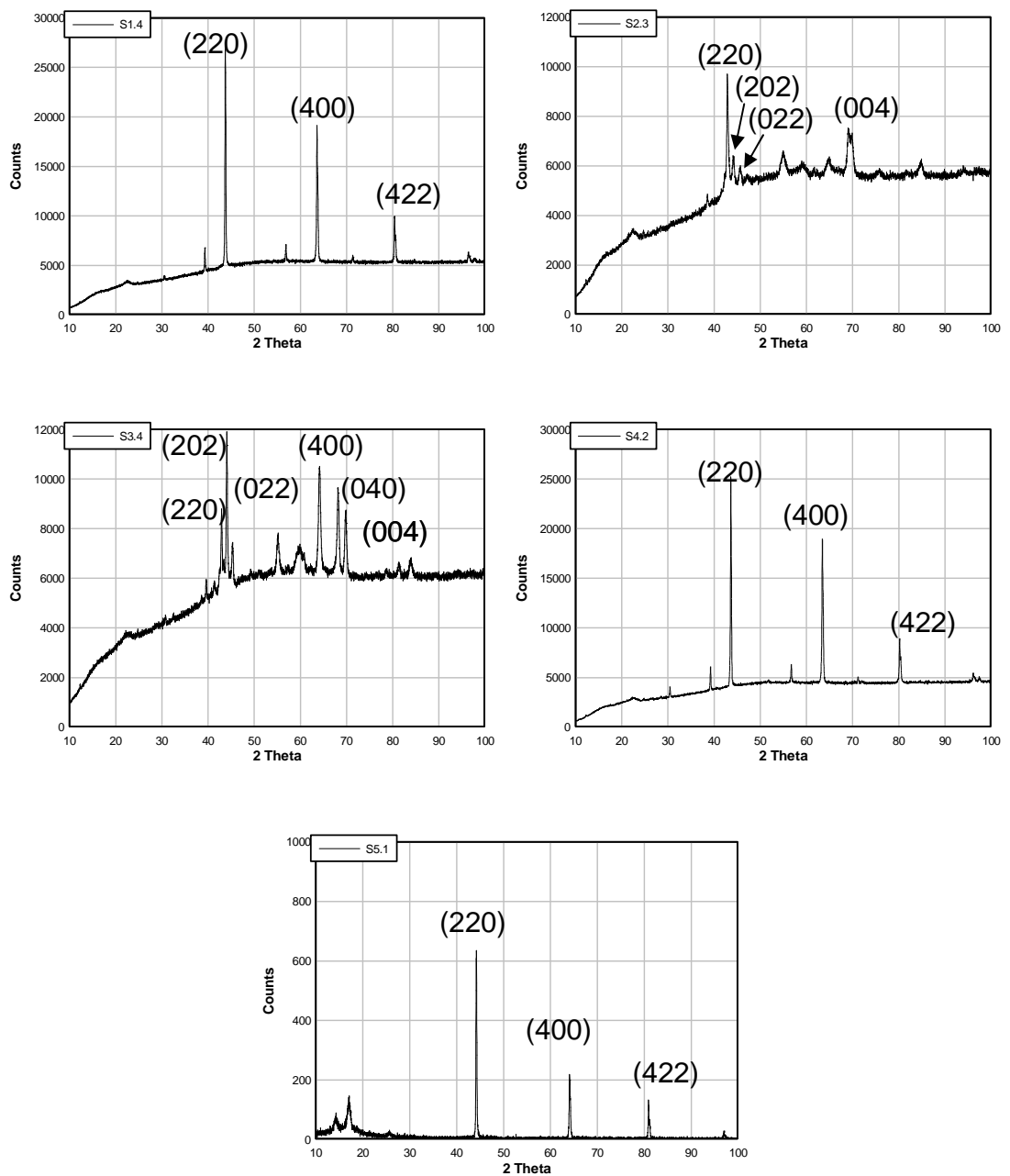


Figure 4.5 XRD patterns for 'as-spun' ribbons 1.4, 2.3, 3.4, 4.1 and 5.1

A curve fitting program (Fityk) was used to fit the data and remove the zero error of the diffractometer using the prior knowledge that there is likely to be a cubic or

orthorhombic phase present[6]. The zero error was typically 0.3° but it varied randomly between samples so it was necessary to eliminate this error to obtain accurate lattice parameters.

Sample	Phase	Lattice Parameters (nm)
1.4	BCC (Heusler)	0.584
	FCC	0.323
2.3	Orthorhombic	0.621, 0.571, 0.541
3.4	Orthorhombic	0.613, 0.579, 5.488
4.1	BCC (Heusler)	0.585
	FCC	0.324
5.1	BCC	0.580

Table 4.3 Lattice Parameters for as-spun Ni-Mn-Ga samples

There were two phases present in sample 1.4, a Heusler structure and another unidentified FCC phase. The Heusler structure was identified by the presence of a (200) peak at 30.5° which results from the different scattering factors of Mn and Ga atoms at the body centres. Sample 2.3 however has an orthorhombic martensitic phase at room temperature with another unidentified phase present. Sample 3.4 is also an orthorhombic martensite at room temperature. There are 2 phases in sample 4.1, very much the same as 1.4 to within experimental error and finally 5.1 has only the one BCC phase present although there are no extra peaks to indicate Heusler type ordering.

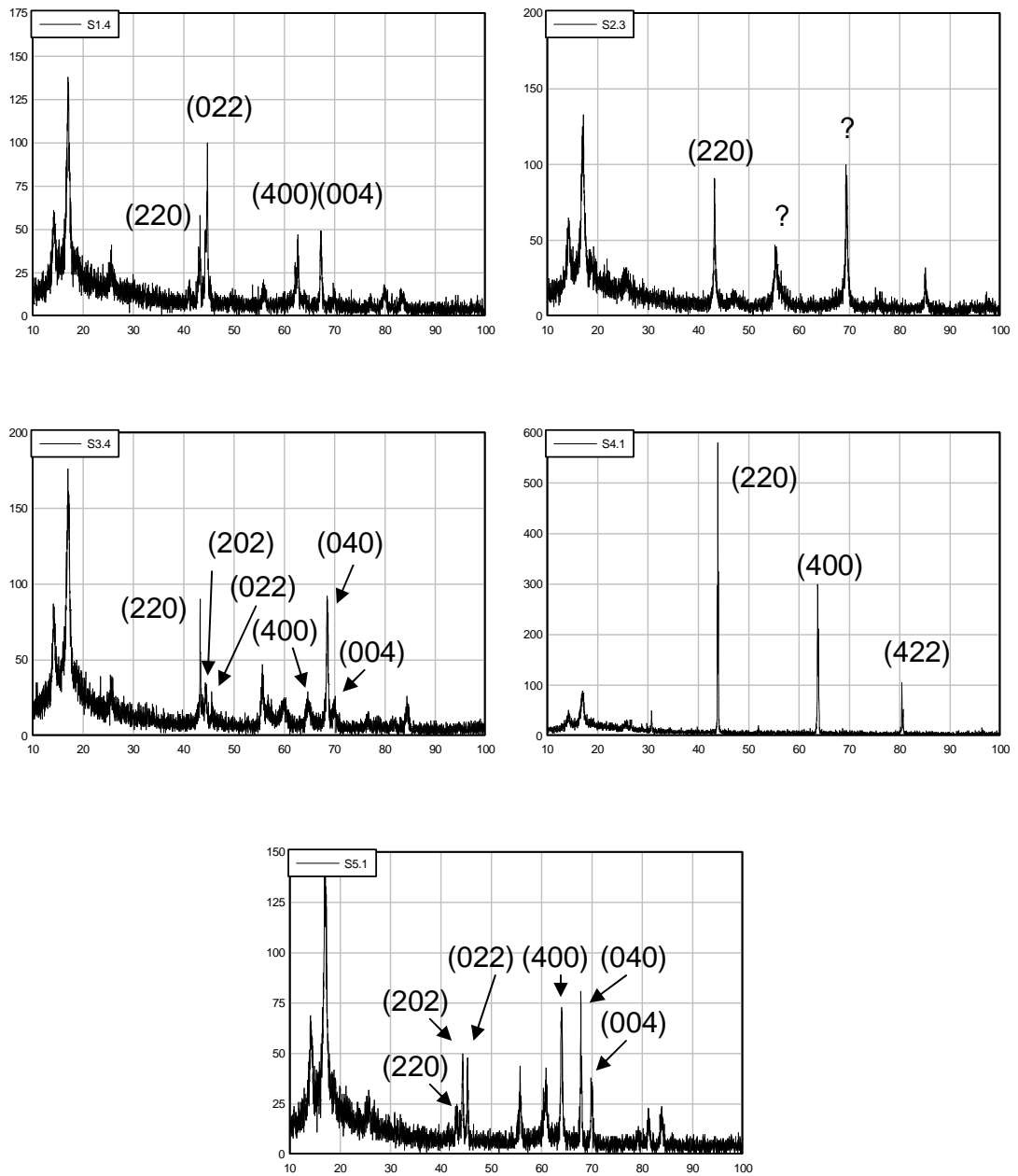


Figure 4.6 XRD of samples 1.4, 2.3, 3.4, 4.1 and 5.1 annealed at 800°C for 12 hours

Sample	Phase	Lattice Parameters (nm)
1.4	Tetragonal	a=b=0.594, c=5.58
2.3	BCC	0.588
3.4	Orthorhombic	0.623, 0.579, 0.552
4.1	BCC	0.583
5.1	Orthorhombic	0.610, 0.582, 0.552

Table 4.4 Lattice parameters of Ni-Mn-Ga samples annealed at 800°C for 12 hours

It was expected that the increase in stress and atomic disorder from the quenching involved during the preparation of ribbons would suppress the martensitic transition temperature such that it was below room temperature for the as-cast samples. The diffraction patterns show that this indeed happened with samples 1.4 and 5.1, both of which became martensitic at room temperature after annealing. Table 4.4 shows that sample 3.4 had a small change in lattice parameter as a result of the increase of atomic order on annealing and sample 4.1 kept the same lattice parameter although the second unexpected BCC phase was barely visible after annealing suggesting that it was a metastable phase precipitated out during rapid cooling. A re-examination of the data in Figure 4.2 and Figure 4.3 shows that it is the martensitic sample (3.4) that shows the critical field phenomena in the hysteresis loops, suggesting that it is connected with the

crystal structure. The martensite phase is known to exhibit field induced twin boundary motion at fields in the range of 200kA/m[7] which is approximately the field at which there is a rapid increase in the magnetic moment in Figure 4.3 suggesting that this feature of Figure 4.3 is due to twin boundary motion.

Optical microscopy coupled with Differential Interference Contrast (DIC) was used to analyse the annealed ribbons because of the ability of DIC to image changes in surface relief, leading to the ability to directly image twin boundaries. Figure 4.7 shows the surface of the annealed ribbon 1.4 in which the grain boundaries are clearly visible but there is no evidence of twin boundaries on the surface of this sample. The dark bands in Figure 4.8, Figure 4.9 and Figure 4.11 are formed by DIC coupled with sharp changes in the surface relief. This is indicative of a twinned structure, showing that samples 2.3, 3.4 and 5.1 have a twinned martensitic structure. These dark bands are not present in Figure 4.10 Figure 4.11 (sample 4.1) which has previously been shown to be in the austenitic cubic phase which does not form twins.

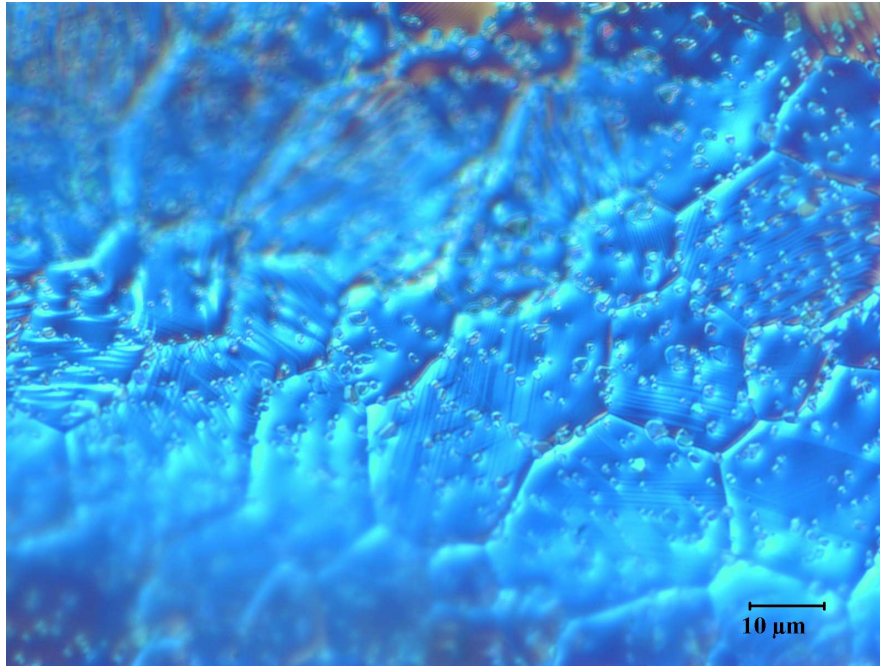


Figure 4.7 Optical image of annealed sample 1.4 at 1000x magnification using DIC

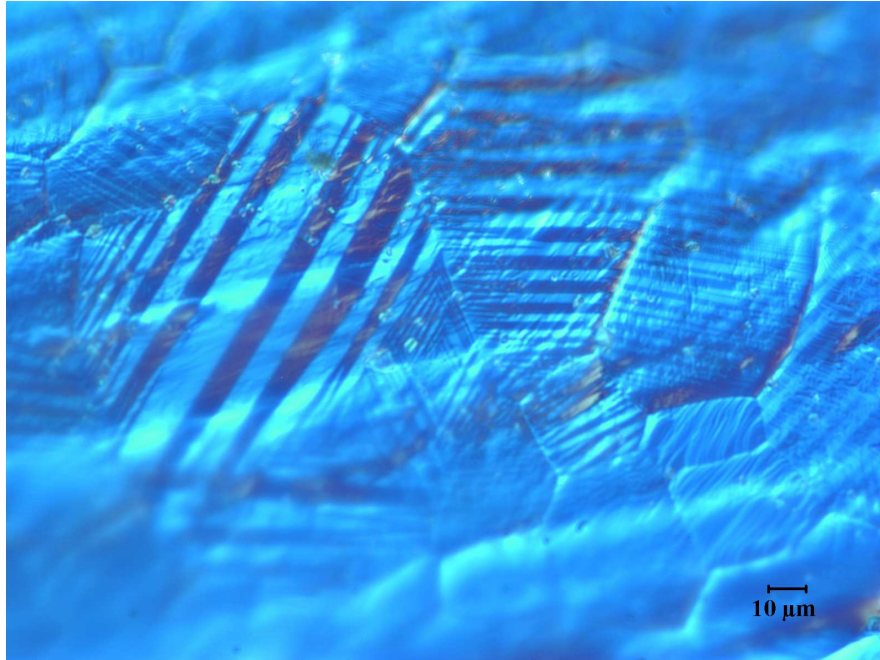


Figure 4.8 Optical image of annealed sample 2.3 at 1000x magnification using DIC

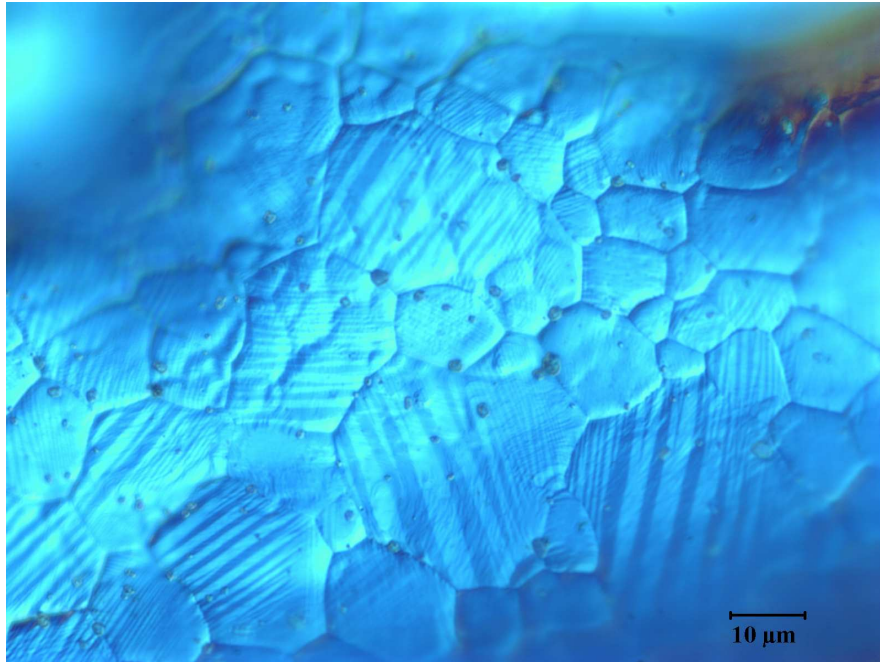


Figure 4.9 Optical image of annealed sample 3.4 at 1000x magnification using DIC

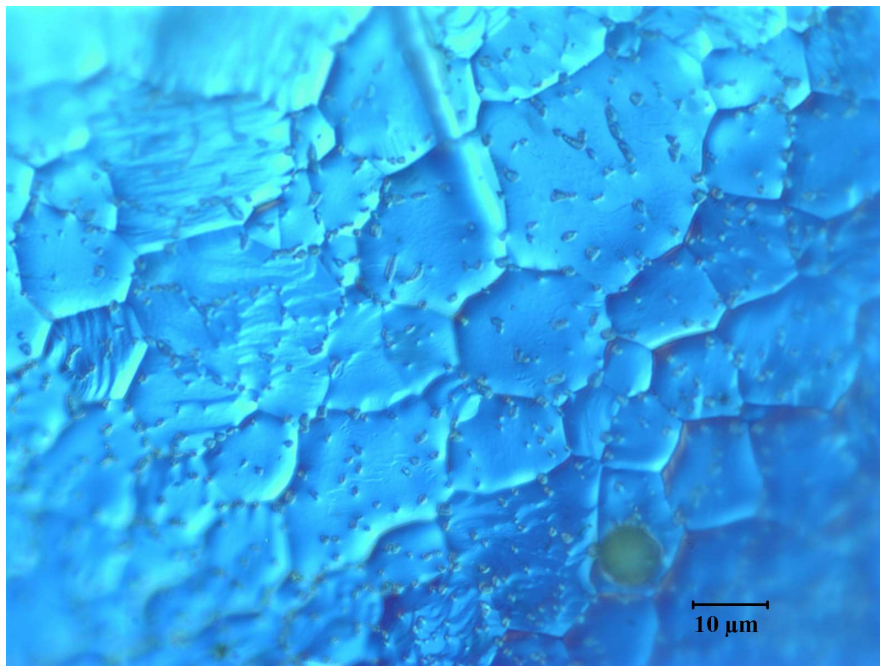


Figure 4.10 Optical image of annealed sample 4.1 at 1000x magnification using DIC

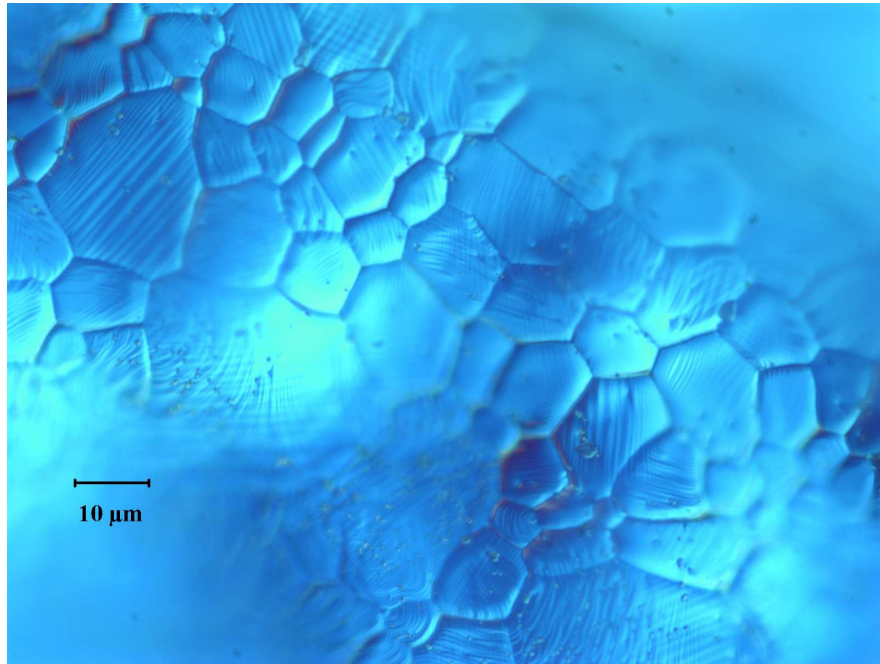


Figure 4.11 Optical image of annealed sample 5.1 at 1000x magnification using DIC

4.1.4 Magnetic Field Induced Strain

All of the ribbons were tested for field induced strain (λ) in the capacitance dilatometer at fields up to 1200kA/m. The saturation magnetostriction, λ_s was found from the usual parallel and perpendicular measurements of λ in which the field is set to maximum and the strain is measured with the field along the ribbon axis and then perpendicular to it. λ_s is then calculated from those measurements.

$$\lambda_s = \frac{2}{3} [\lambda_{parallel} - \lambda_{perpendicular}] \quad \text{Eq. 2.21}$$

It was found that all of the as-spun ribbons had a saturation magnetostriction λ_s of -5ppm +/- 2ppm. This increased on annealing to -40ppm +/- 5ppm which is

the same as pure nickel to within experimental error. The increase is attributed to relaxation of the cast-in stresses in the annealed ribbons. Interestingly this was true for samples in both the martensitic and austenitic phases. This, coupled with the low value for field induced strain, suggests that the strain is purely magnetostrictive in origin. Strains of several percent have been observed when the mechanism is twin boundary motion[7, 8]. This means one of two things, either the twin boundaries were pinned by crystal defects or the tension on the ribbon exerted by the spring was large enough such that the combination of applied field and magnetoelastic anisotropy could not exert enough force on the twin boundaries to move them. The tension was approximately 2MPa along the ribbon axis, It was attempted to make a weaker spring but this proved to be weakest possible with the current design of dilatometer. It is possible that 2MPa is enough stress to inhibit twin boundary motion but this was the lowest stress that could be achieved.

Plots of strain vs temperature were obtained for the ribbons that exhibited a martensitic transition within the temperature limits of the cryostat. The sample was placed in the dilatometer with a constant field applied along the ribbon axis, the temperature was ramped up through the transition temperature and then allowed to cool back to room temperature while the strain was observed. Figure 4.12 shows an interesting phenomenon for the ribbon 5.1 in that the transformation strain is dependent on an applied magnetic field. Figure 4.13 shows the transformation strain as a function of applied field. The transformation strain is defined as the difference in strain between points below M_f and above

Af. To remove the effect of the usual thermal expansion two parallel lines were drawn along the data below the transition and another along the data points above the transition temperature. This allowed the thermal expansion to be separated from the transformation strain.

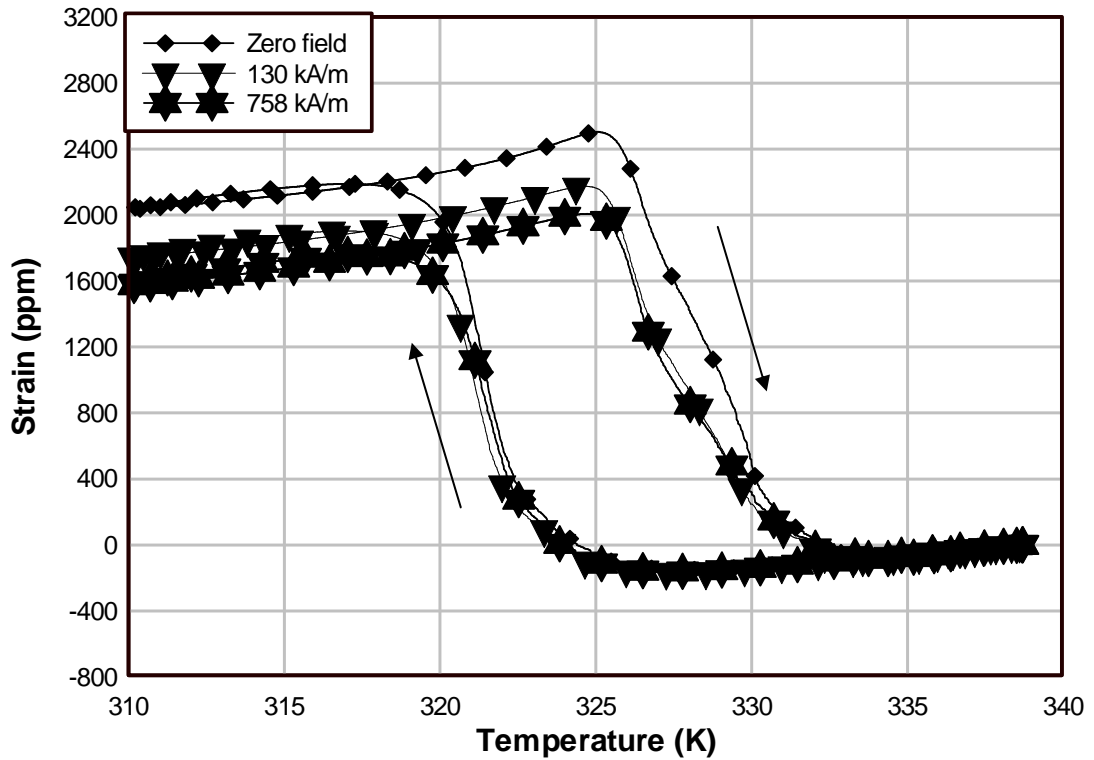


Figure 4.12 The effect of temperature and a field parallel to the ribbon axis on the transformation strain of ribbon 5.1 (annealed 800°C). Some of the curves were omitted for clarity.

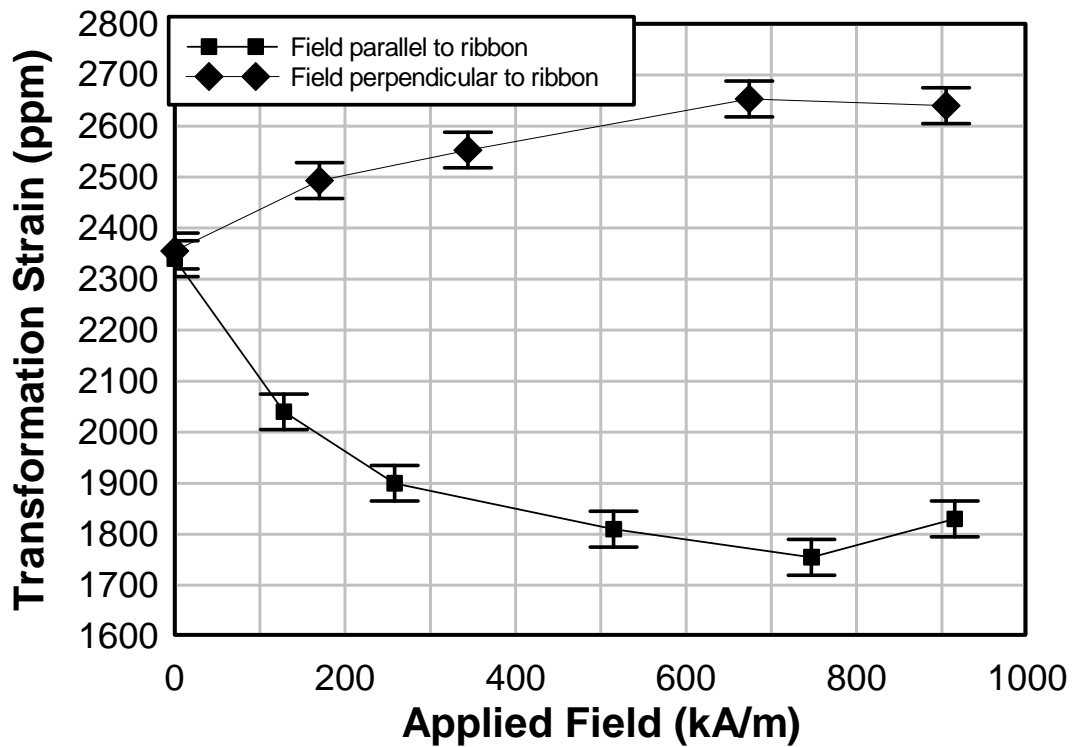


Figure 4.13 Transformation strain of sample 5.1 in an applied field

It can be seen that a magnetic field parallel to the ribbon axis reduces the transformation strain, possibly because of the nucleation of preferentially orientated martensite with the short c axis along the field direction. This hypothesis also fits with the data for a field perpendicular to the ribbon axis which would produce martensite with the short axis preferentially orientated perpendicular to the ribbon axis resulting in elongation along the ribbon axis. It should be noted at this point that this effect would be very sensitive to the applied tension because the nucleation of preferentially orientated martensite is in competition with the applied tension when the field is along the ribbon axis. The

two work together with the field perpendicular to the ribbon axis because both the anisotropy and elastic energies are lowered by an elongation of the ribbon.

4.1.5 Discussion and Summary

Melt spun ribbons of Ni-Mn-Ga have been successfully produced that exhibit the shape memory effect. A martensitic transformation was observed in samples 1.4, 2.3, 3.4 and 5.1, with the tin containing sample 4.1 not showing any transformation between -50°C and 500°C. Annealing at 800°C for 2 hours was shown to significantly increase the grain size to a point where crystal grains are of the order 5-10µm, visible with optical microscopy. It also increases the transformation temperature as a result of the increased atomic order. The presence of twins was confirmed in the annealed samples of 2.3, 3.4 and 5.1 at room temperature. None of the ribbons were observed to exhibit the large field induced strains that have been reported for single crystal NiMnGa, although the magnetisation curves of sample 3.4 did suggest that some twin rearrangement may be occurring. It was not possible to make a direct measurement of the strain. When it was attempted with the capacitance cell the sample did not exhibit any field induced strain above the 40ppm that is expected from magnetostriction. This is likely to be due to the stress from the capacitance cell being too great though this could not be proven.

There has only been one other report of melt spun Ni-Mn-Ga[9] in which a similar effect of the field dependence of the transformation strain was observed. In [9]

the field dependence of the transformation strain was of similar magnitude to that discovered in this work for sample 5.1 although it was of opposite sign because the field was perpendicular to the ribbon axis rather than along it. This effect is attributed to the formation of preferentially orientated twin variants in the presence of a magnetic field which results in the short axis being aligned with the field.

The small dimensions of melt spun ribbons, coupled with the low blocking stress of $\sim 2\text{MPa}$, make direct measurements of the field induced strain very difficult. These materials are very different from the melt spun rare earth magnetostrictive alloys that produce forces which are several orders of magnitude greater. Practical applications of melt spun ribbons of Ni-Mn-Ga are expected to be limited but the process is useful for examining the crystallography of the alloys and in particular analysing metastable states that can be 'quenched in' by the rapid cooling process. This is particularly useful for the analysis of Ni-Fe-Ga in which the BCC austenite phase is metastable.

4.2 Melt Spun Ni-Fe-Ga

4.2.1 Sample Preparation

A composition series of Ni-Fe-Ga-Tb was prepared by arc melting at Birmingham University. This was $\text{Ni}_{53}\text{Fe}_{21-x/2}\text{Ga}_{26}\text{Tb}_{x/2}$ for $x = 0 - 7$. The aim was to investigate the effect of Terbium substitution close to the composition $\text{Ni}_{54}\text{Fe}_{19}\text{Ga}_{27}$ which is known to have an M_s of 27°C and a T_c of 37°C [10]. The 20g ingots were broken up in a press into pieces small enough to fit inside the 5mm diameter quartz tubes of the melt spinner. The pieces were kept under vacuum when not being used to prevent oxidation. The melt spinning parameters were varied in the same way as for the Ni-Mn-Ga samples in order to obtain good pieces of ribbon of more than a few cm in length. Several pieces of each composition were annealed under argon at 500, 600 and 700°C for 2 hours to investigate the effect of recrystallisation and stress relief on the magnetic and crystalline properties of these alloys. The actual compositions were measured using ICPMS and are shown in Table 4.5.

Sample No.	Nickel (at%)	Iron (at%)	Gallium (at%)	Terbium (at%)
1a	54.47 (53)	20.41 (21)	25.12 (26)	0.00 (0)
2a	54.31 (53)	20.76 (20.5)	24.68 (26)	0.25 (0.5)
3b	55.13 (53)	19.75 (20)	24.62 (26)	0.50 (1)
4a	54.53 (53)	19.62 (19.5)	24.99 (26)	0.85 (1.5)
5a	54.73 (53)	19.09 (19)	24.97 (26)	1.20 (2)
6a	54.03 (53)	19.04 (18.5)	25.23 (26)	1.69 (2.5)
7a	54.52 (53)	17.75 (18)	25.44 (26)	2.29 (3)
8a	54.51 (53)	16.72 (17.5)	25.86 (26)	2.92 (3.5)

Table 4.5 Measured compositions of the melt spun Ni-Fe-Ga-Tb ribbons.

Nominal values are shown in brackets

4.2.2 Crystal Structure

The X-Ray diffraction patterns of the $\text{Ni}_{53}\text{Fe}_{21-x/2}\text{Ga}_{26}\text{Tb}_{x/2}$ samples are shown in Figure 4.14, Figure 4.15 and Figure 4.16 with the calculated lattice parameters in Table 4.6. It can be seen from this the samples are predominantly in a single BCC phase but some have a small amount of an additional phase present as identified by a weak peak at $\sim 43^\circ$. This second phase becomes more prominent in some samples after annealing at 600°C and 700°C and is identified from the resulting diffraction patterns and shown in Table 4.6. Interestingly however, on annealing the second FCC phase becomes less prominent with increasing Tb

content up to 1.2%. In sample 5a with 1.2% Tb there is almost no FCC phase present suggesting that a small amount of Tb stabilises the BCC phase. This effect could be very useful in producing Ni-Fe-Ga shape memory alloys which have the problem that the BCC phase, required for the shape memory effect is metastable and only produced in significant quantity with rapid cooling, as in the melt spinning process[11].

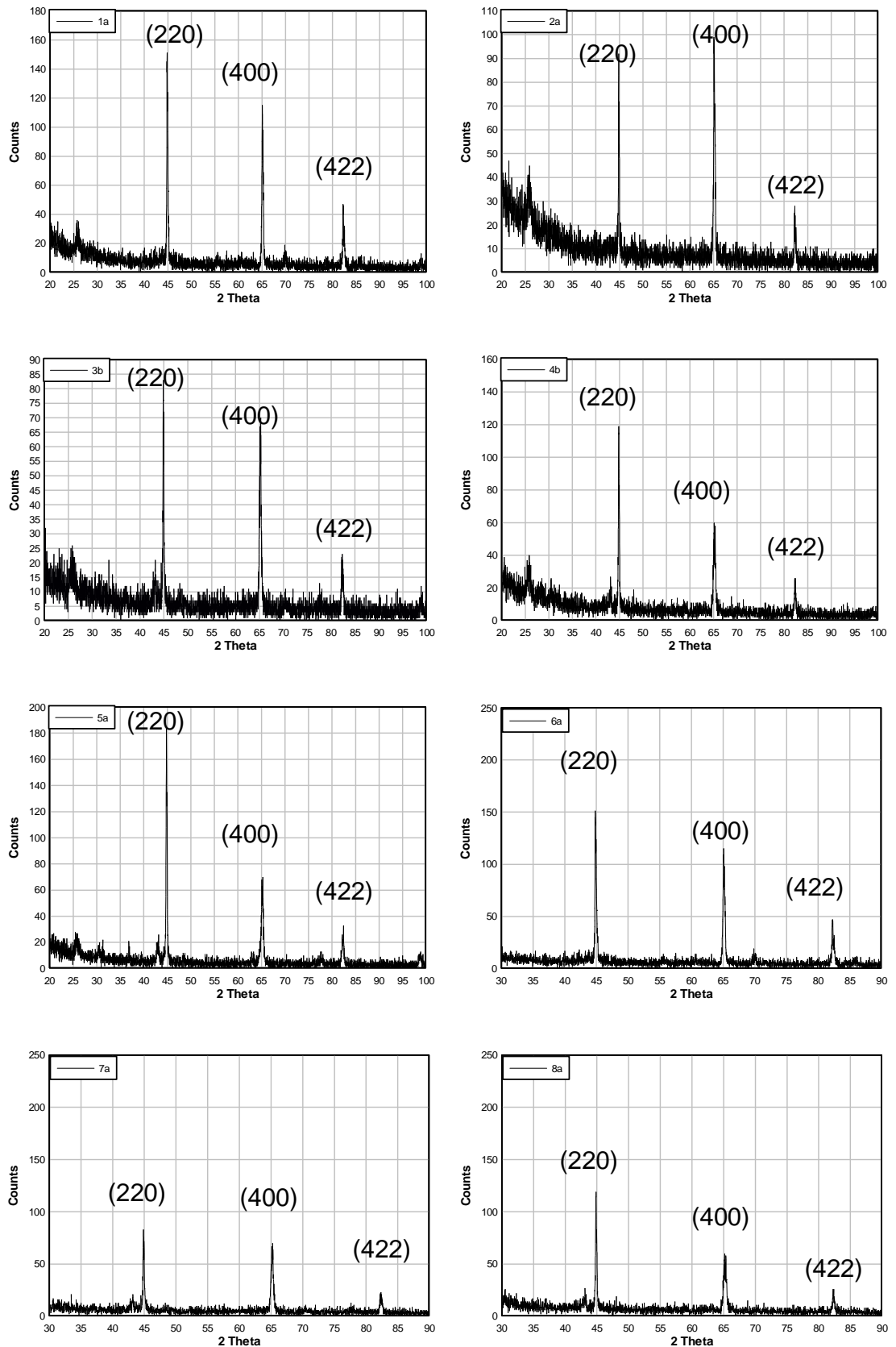


Figure 4.14 X-Ray Diffraction patterns of $\text{Ni}_{53}\text{Fe}_{21-x/2}\text{Ga}_{26}\text{Tb}_{x/2}$ ribbons in the as-spun state.

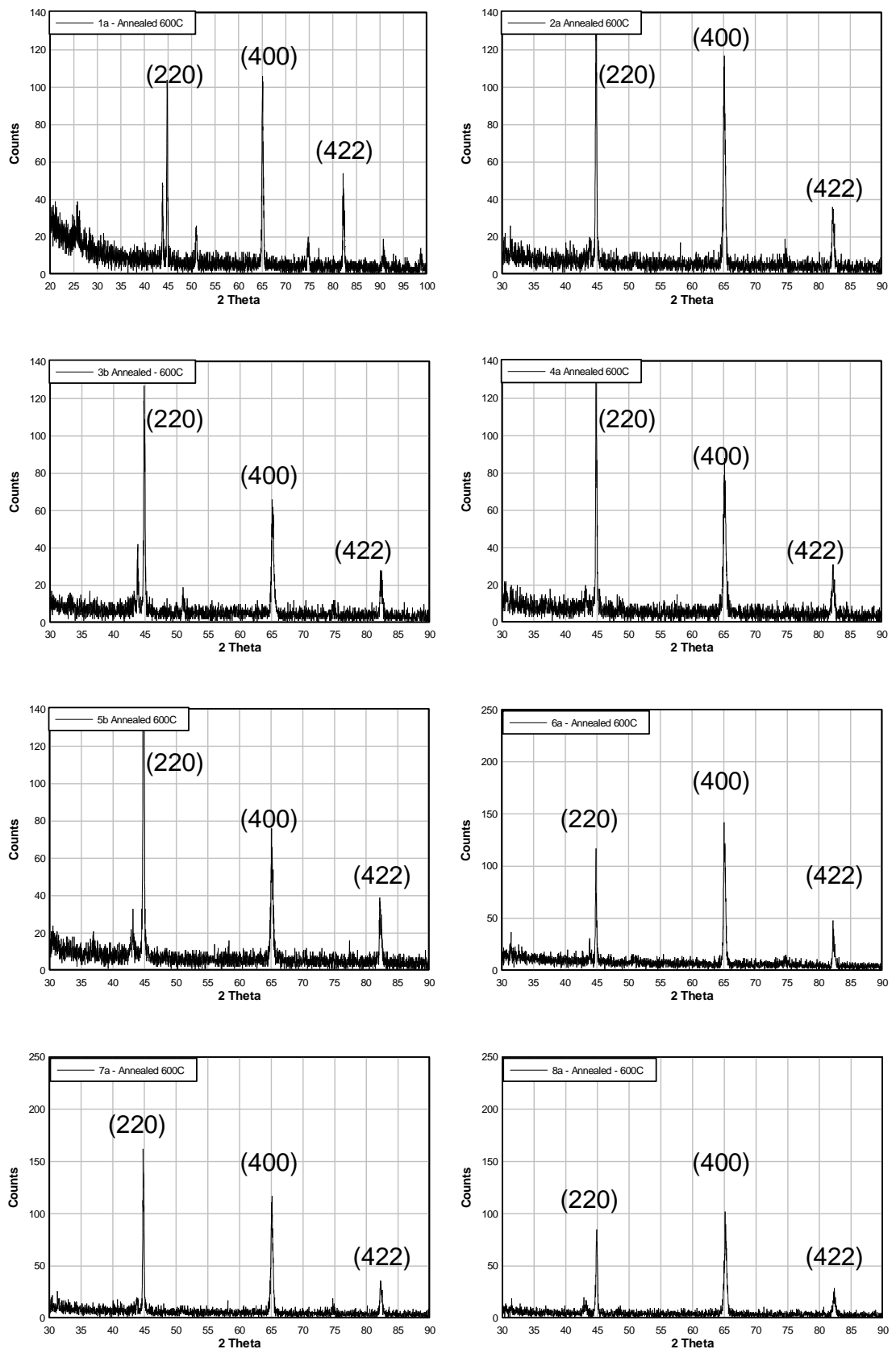


Figure 4.15 X-Ray Diffraction patterns of $\text{Ni}_{53}\text{Fe}_{21-x/2}\text{Ga}_{26}\text{Tb}_{x/2}$ ribbons after annealing at 600°C.

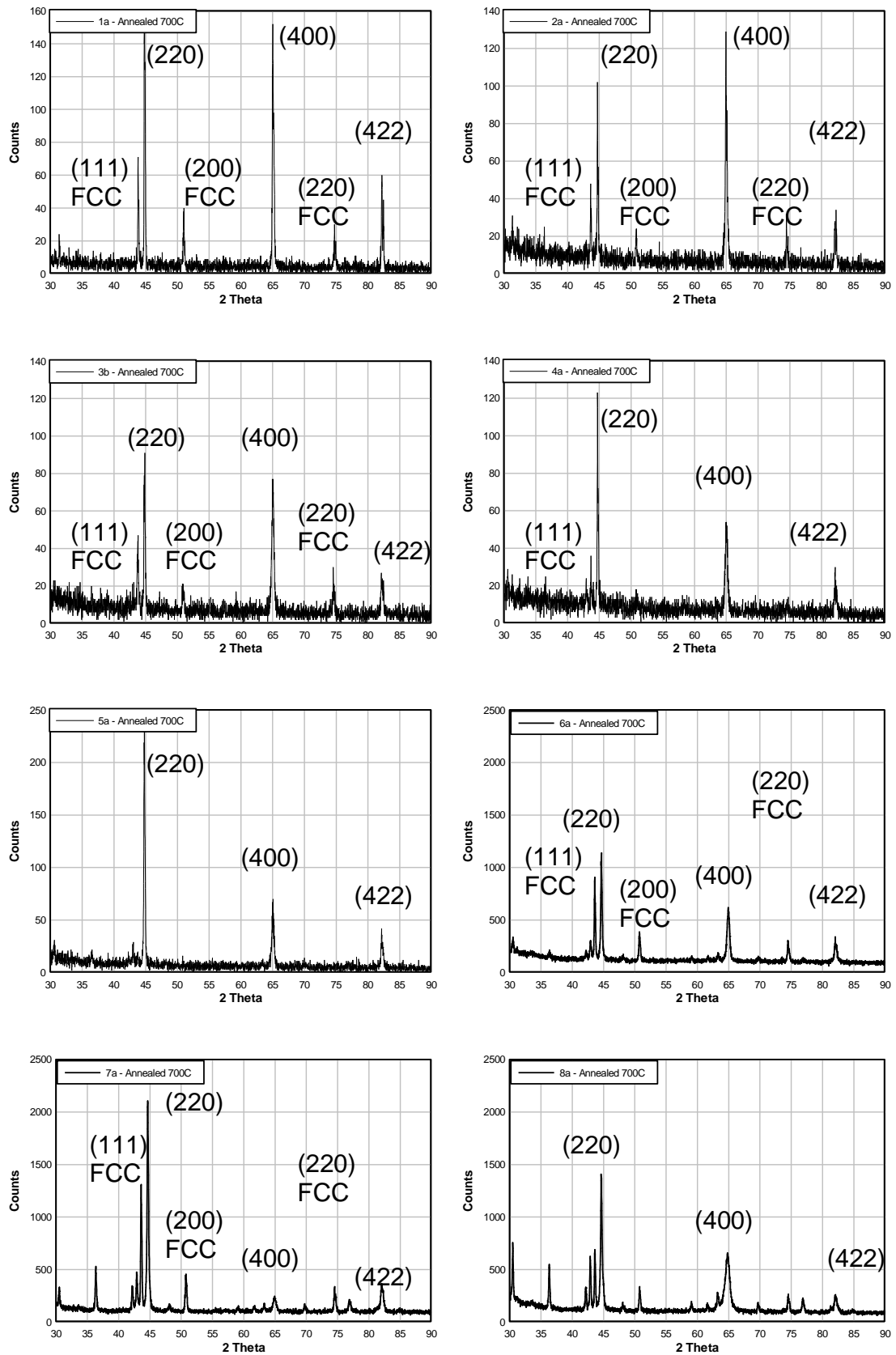


Figure 4.16 X-Ray Diffraction patterns of $\text{Ni}_{53}\text{Fe}_{21-x/2}\text{Ga}_{26}\text{Tb}_{x/2}$ ribbons after annealing at 700°C .

Sample No. and annealing temp (°C)	BCC lattice parameter (nm)	FCC lattice parameter (nm)
1a (As Spun)	0.5762	N/A
1a (600)	0.5761	0.3606
1a (700)	0.5763	0.3606
2a (As Spun)	0.5756	N/A
2a (600)	0.5758	0.3605
2a (700)	0.5763	0.3612
3a (As Spun)	0.5757	N/A
3a (600)	0.5758	N/A
3a (700)	0.5768	0.3614
4a (As Spun)	0.5757	N/A
4a (600)	0.5757	N/A
4a (700)	0.5762	0.3609
5a (As Spun)	0.5758	N/A
5a (600)	0.5757	N/A
5a (700)	0.5764	N/A
6a (As Spun)	0.5754	N/A
6a (600)	0.5755	N/A
6a (700)	0.5763	0.3610
7a (As Spun)	0.5755	N/A
7a (600)	0.5757	N/A
7a (700)	0.5765	0.3609
8a (As Spun)	0.5756	N/A
8a (600)	0.5757	N/A
8a (700)	0.5763	N/A

Table 4.6 Lattice parameters obtained from XRD for the $\text{Ni}_{53}\text{Fe}_{21-x/2}\text{Ga}_{26}\text{Tb}_{x/2}$

series

4.2.3 Magnetisation

The ribbons were analysed by field cooling to liquid nitrogen temperature (77K) and heating to room temperature in a static field of 100Oe. This allowed the phase changes and Curie temperatures to be clearly seen. Figure 4.17 shows the variation of these properties with composition. The martensitic transformation which starts at M_s appears on the thermomagnetisation curves as a sharp reduction in the magnetisation on cooling due to the larger magnetocrystalline anisotropy of the martensite as seen in Figure 4.18. The reverse transformation on heating which begins at A_s shows the opposite, a sharp increase of the magnetisation because the austenite phase is easier to magnetise due to the reduced anisotropy. There is always some hysteresis in the transformation, typically about 10K for the studied samples. The phase change temperatures are shown in Table 4.7. The as-spun samples showed no phase change in this temperature range and are therefore not shown. It is possible that the as-spun ribbons exhibited a phase change below 77K but this is not known at present. It was expected that annealing and the resultant stress relief and crystallisation would increase the martensitic transition temperatures as in the NiMnGa system. All five of the samples did show a martensitic transition after annealing with the transition temperatures shown in Table 4.7.

Sample No, and (annealing Temperature(°C))	Ms (K)	Mf (K)	As (K)	Af (K)	Tc (K)
1a (600)	138	114	125	160	376
1a (700)	148	132	136	168	361
2a (600)	148	131	150	201	380
2a (700)	108	86	94	119	369
3a (600)	205	135	150	217	380
3a (700)	120	81	93	128	370
4a (600)	147	104	118	168	370
4a (700)	124	104	112	135	369
5a (600)	153	100	110	167	374
5a (700)	150	110	123	161	366
6a (600)	n/a	n/a	n/a	n/a	383
6a (700)	n/a	n/a	n/a	n/a	375
7a (600)	n/a	n/a	n/a	n/a	399
7a (700)	n/a	n/a	n/a	n/a	373
8a (600)	n/a	n/a	n/a	n/a	368
8a (700)	n/a	n/a	n/a	n/a	395

Table 4.7 Martensitic transition temperatures and Curie temperatures of annealed $\text{Ni}_{53}\text{Fe}_{21-x/2}\text{Ga}_{26}\text{Tb}_{x/2}$ ribbons as measured by field cooling in 7.95kA/m applied field

Figure 4.17 shows how the transformation temperature varies with Terbium content. There is an initial decline between 0% and 0.25% Tb, but M_s then begins to increase until 1.25% at which point it is 150K, 12K higher than with no

Tb. A martensitic transition with up to 1.25% Tb is expected from the crystallography because the increasing Tb content up to that point inhibits the formation of the non shape memory FCC phase. Above 1.25% however no transformation occurs, probably due to the unidentified phase which begins to appear at these higher concentrations. The Curie temperature is relatively constant in the samples annealed at 700°C but shows a significant variation in the samples annealed at 600°C possibly due to these samples being less homogeneous after annealing.

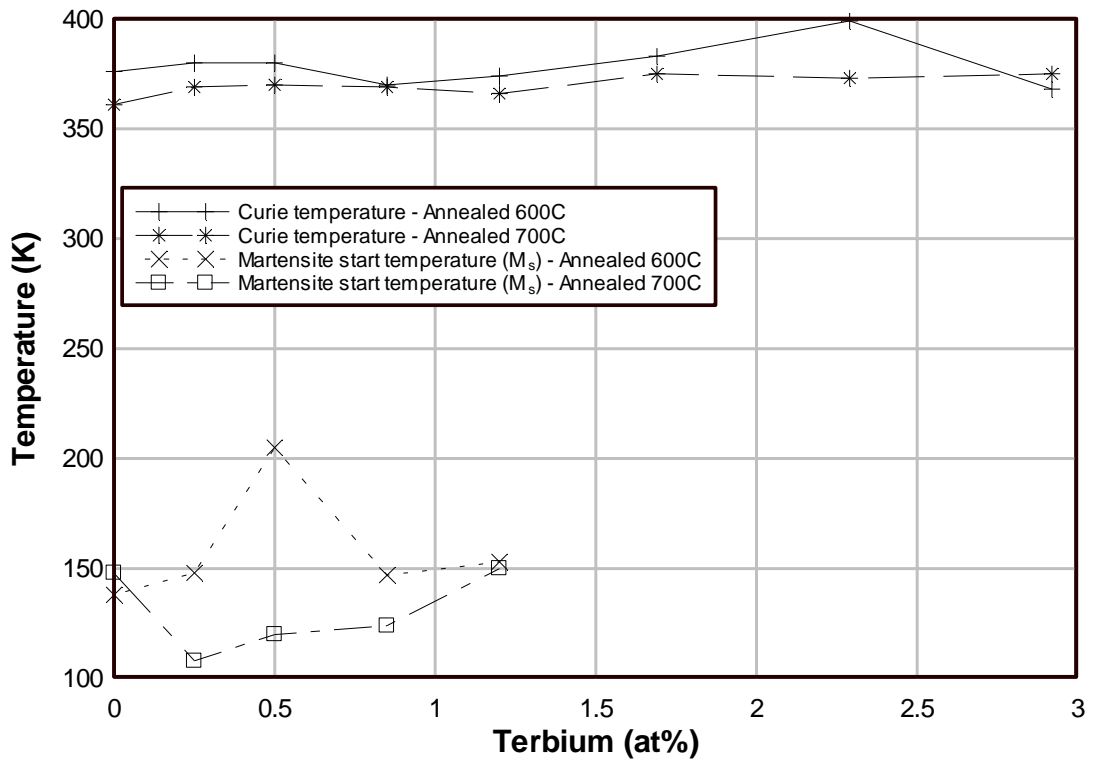


Figure 4.17 The variation of Curie temperature and martensite transformation temperatures for the series $\text{Ni}_{53}\text{Fe}_{21-x/2}\text{Ga}_{26}\text{Tb}_{x/2}$

Figure 4.18, Figure 4.19 Figure 4.20, Figure 4.21 and Figure 4.22 show the thermomagnetisation curves as samples 1a, 2a, 3b, 4a and 5a were cooled from 400K to 77K and heated again at a rate of 10K/min. These graphs show the significant differences of adding Terbium to the alloy. Sample 5a shows little difference between the 2 annealing temperatures whereas sample 2a has approximately a 75K difference in the martensitic transition temperatures. This difference can be explained from the crystallography of the alloys, a face centred cubic phase is formed at the higher annealing temperature in the alloys with less terbium, but the 1.2 at% Tb in sample 5a inhibits this formation and it is predominantly a BCC phase at both annealing temperatures.

Figure 4.23, Figure 4.24 and Figure 4.25 show that samples 6, 7 and 8 do not undergo any martensitic transformation at all and X-Ray diffraction shows several extra peaks and the extra Terbium enables the formation of an unidentified phase which inhibits the martensitic transformation. The Curie temperature of these three samples is also suppressed by approximately 25K by increasing the annealing temperature from 600°C to 700°C. This is attributed to the formation of the unknown phase that appears in these three samples.

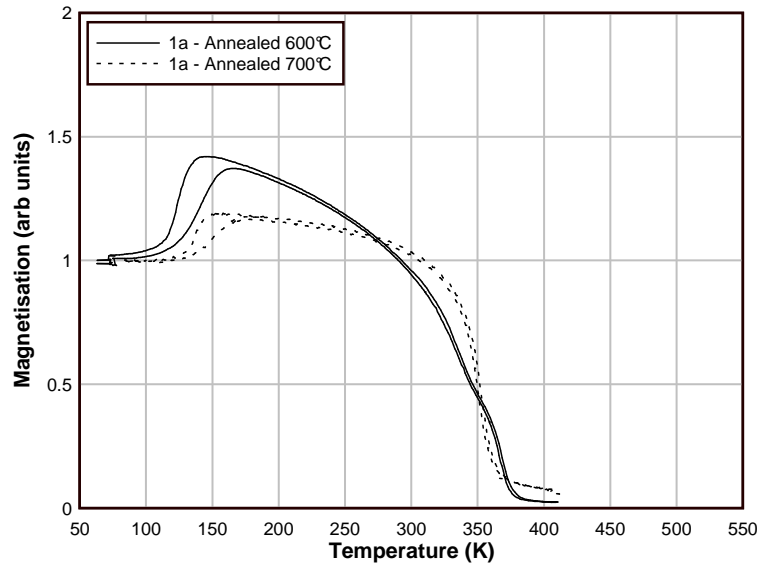


Figure 4.18 Thermomagnetisation curve for sample 1a at 7.95kA/m applied field

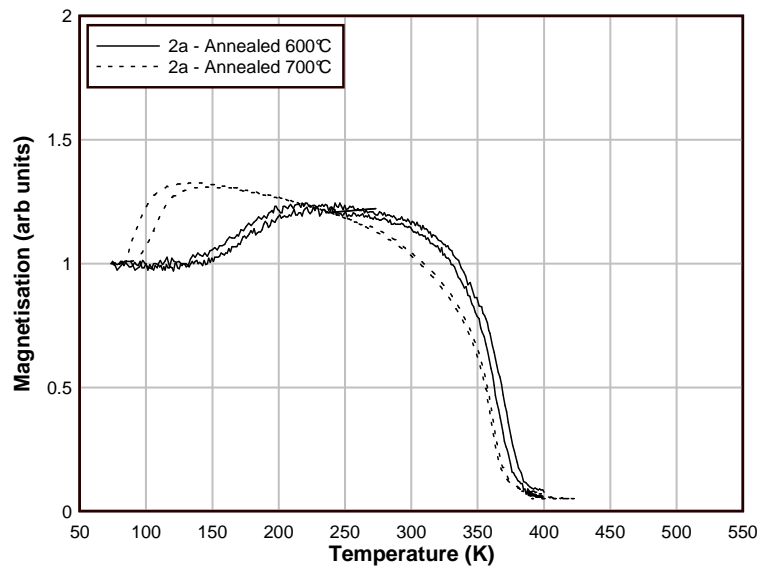


Figure 4.19 Thermomagnetisation curve for sample 2a at 7.95kA/m applied field

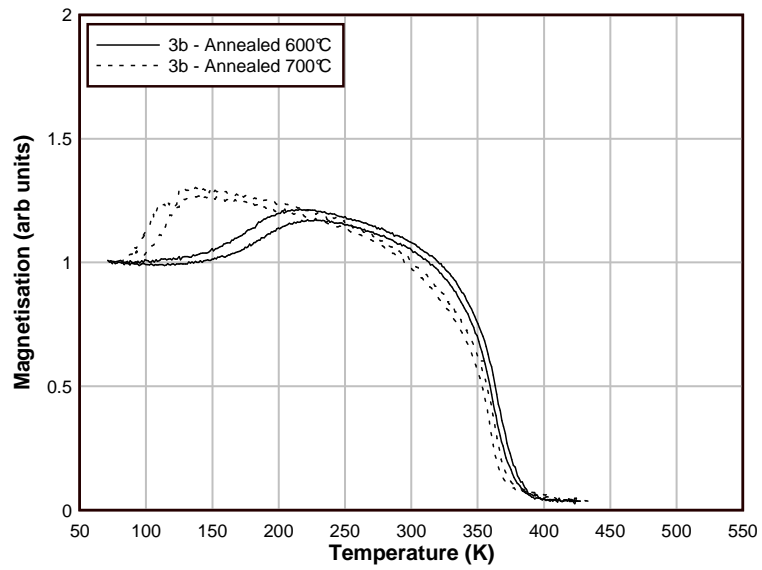


Figure 4.20 Thermomagnetisation curve for sample 3b at 7.95kA/m applied field

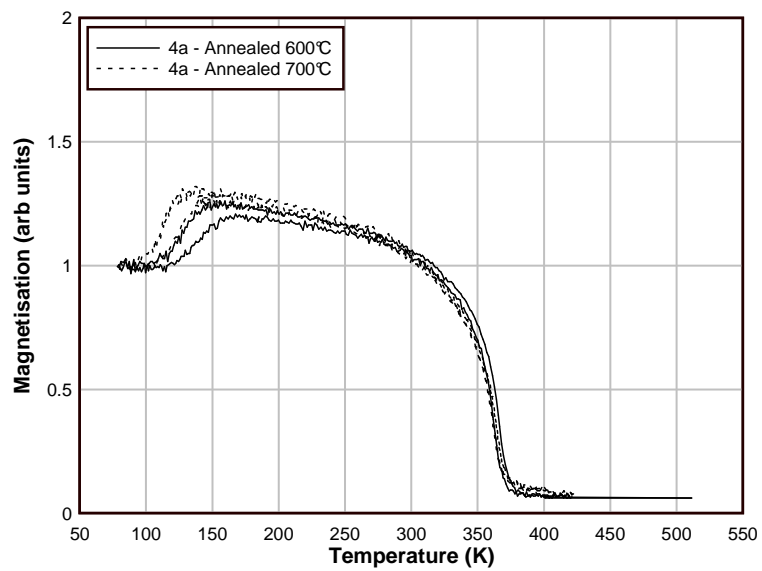


Figure 4.21 Thermomagnetisation curve for sample 4a at 7.95kA/m applied field

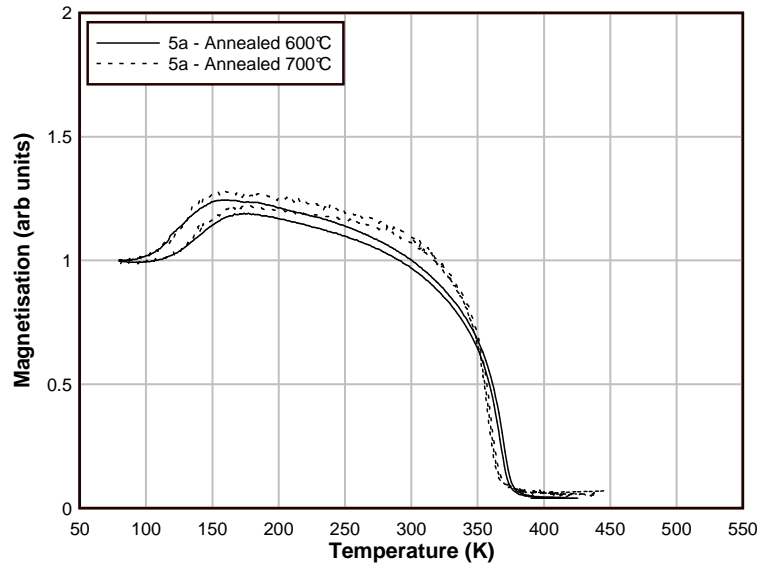


Figure 4.22 Thermomagnetisation curves of sample 5a at 7.95kA/m applied field

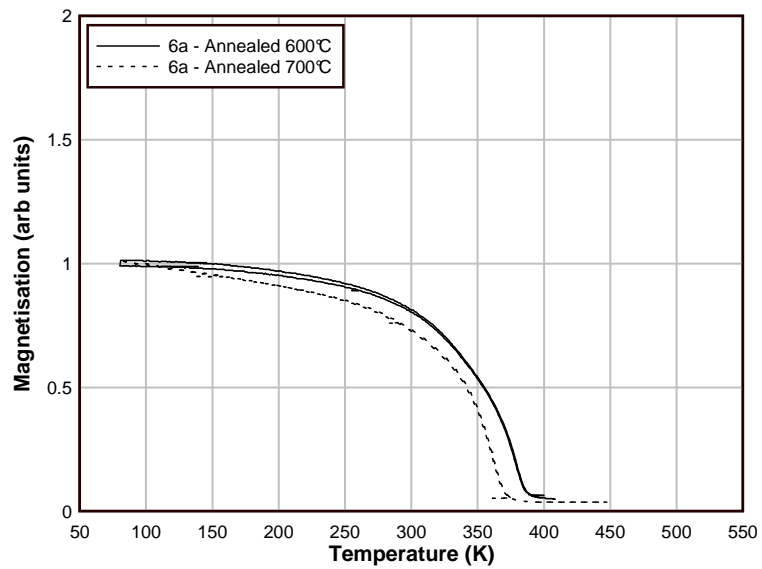


Figure 4.23 Thermomagnetisation curve for sample 6a at 7.95kA/m applied field

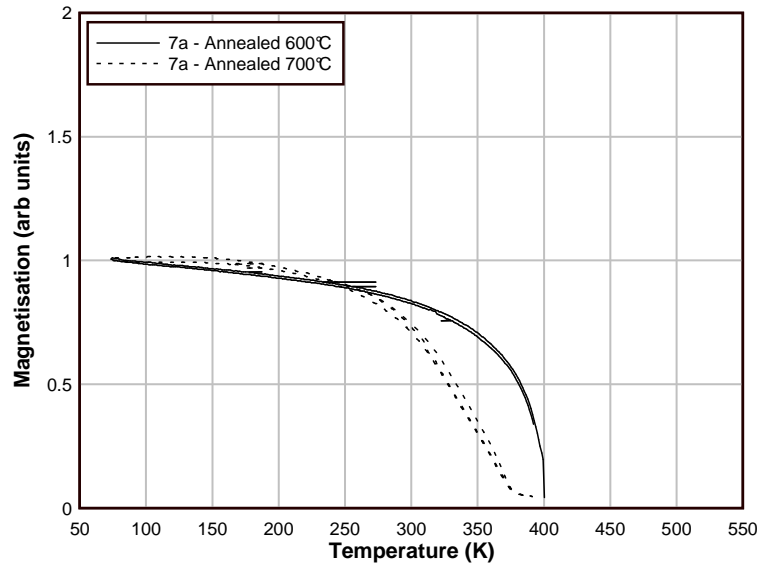


Figure 4.24 Thermomagnetisation curve of sample 7a at 7.95kA/m applied field

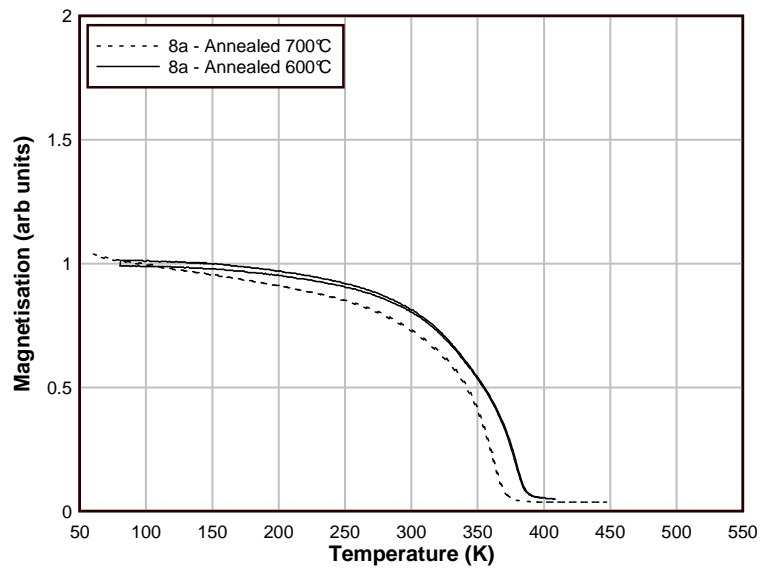


Figure 4.25 Thermomagnetisation curve for sample 8a at 7.95kA/m applied field

4.2.4 Discussion and summary

Ribbons of Ni-Fe-Ga that exhibit the memory effect have been successfully produced. It has also been shown that the rapid quenching of the melt spinning process stabilises the BCC phase that is required for the shape memory effect. This is in good agreement with [11], the only other report of melt-spun Ni-Fe-Ga ribbons. In [11], melt spun ribbons of the single composition Ni₂FeGa were produced which had a martensitic transformation temperature in the region of 130K, comparable to that found in this work. A significant new finding of this work is that the presence of a small amount of Terbium (1.2%) in the Ni-Fe-Ga ribbons inhibits the formation of the FCC phase (often called the γ phase) on annealing the ribbons at 700°C. This could be significant in the production of Ni-Fe-Ga alloys in which the formation of the FCC phase prevents the production of bulk samples with conventional crystal growing techniques.

An additional effect of increasing Terbium content is that the martensitic transformation temperature in the samples annealed at 600°C and 700°C begins to converge to the point where they are the same in sample 5a, at 150K. The XRD data suggests that the stabilisation of the BCC phase, and suppression of the FCC phase may be responsible for this effect. The difference in transition temperature at different annealing temperatures has been reported in [12] which presents results for Ni₅₁Ga₂₇Fe₂₂ that are comparable to sample 1a with a transition temperature of approximately 140K. No martensitic transformation is observed with > 1.25% Tb.

Some compositions of Ni-Fe-Ga have been shown to have a martensitic transition temperature near room temperature [13, 14] which is essential for the material to be used as an actuator device. The compositions studied in this work were very close to that studied in [13], but the reported transformation temperatures of 4°C are much higher than that found in this work. This is probably due to the fact that the sample in [13] was a single crystal grown by the Bridgman technique but the exact reason for the difference is not determined.

4.3 Melt Spun Ni-Fe-Al

It has been shown that the martensitic transition is highly dependent on the valence electron per atom ratio (e/a), with the transformation appearing when $e/a > 6.8$ and the transition temperature having a strong dependence on e/a [15, 16]. As a result of this it was postulated that a substitution of Al for Ga in the alloy Ni-Fe-Ga would result in a ferromagnetic shape memory alloy. Three alloy compositions were made, to cover a proportion of the composition range in which the shape memory should occur according to the valence electron per atom ratio. Clearly whether the alloy exhibits shape memory is also dependent upon the crystal structure and heat treatments so the alloys are subjected to the same procedures as the Ni-Mn-Ga melt spun ribbons.

4.3.1 Sample Preparation

Three ingots of Ni-Fe-Al were produced by arc melting under an argon atmosphere for an hour to produce a homogeneous alloy. These were then broken up in a hydraulic press to produce pieces small enough to fit inside the melt spinning tubes. The nominal compositions were $\text{Ni}_{52}\text{Fe}_{21}\text{Al}_{27}$, $\text{Ni}_{54}\text{Fe}_{19}\text{Al}_{27}$, $\text{Ni}_{56}\text{Fe}_{17}\text{Al}_{27}$ for samples 1, 2 and 3 respectively. Actual compositions were within 0.25% of nominal. Ribbons of each composition were then produced by melt spinning and these were heat treated at 700°C , under 500mbar argon for two hours for stress relief and recrystallisation.

4.3.2 Magnetisation

Samples of each ribbon were analysed in the VSM to determine whether there is any ferromagnetic phase change below room temperature and to analyse the magnetic properties of the material. Field cooling was performed at 7.95kA/m applied field from room temperature down to 77K to determine whether there is any martensitic transformation which is characterised by a large change in anisotropy energy in both Ni-Fe-Ga and Ni-Mn-Ga. Figure 4.26 shows that the Curie temperature of ribbons 2 and 3 is well above 430K, the maximum available in the VSM but there was no evidence of any martensitic phase change in either the as-spun or the annealed ribbons. Sample 1 has a lower Curie temperature of 395K. Room temperature hysteresis loops were also obtained and are shown in Figure 4.27.

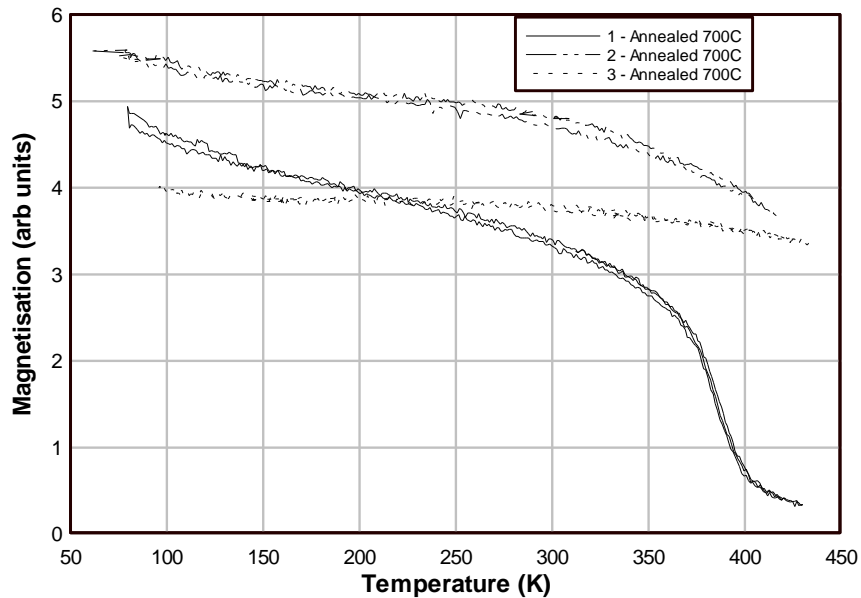


Figure 4.26 Thermomagnetisation curves for the annealed samples of Ni-Fe-Al at an applied field of 7.95kA/m

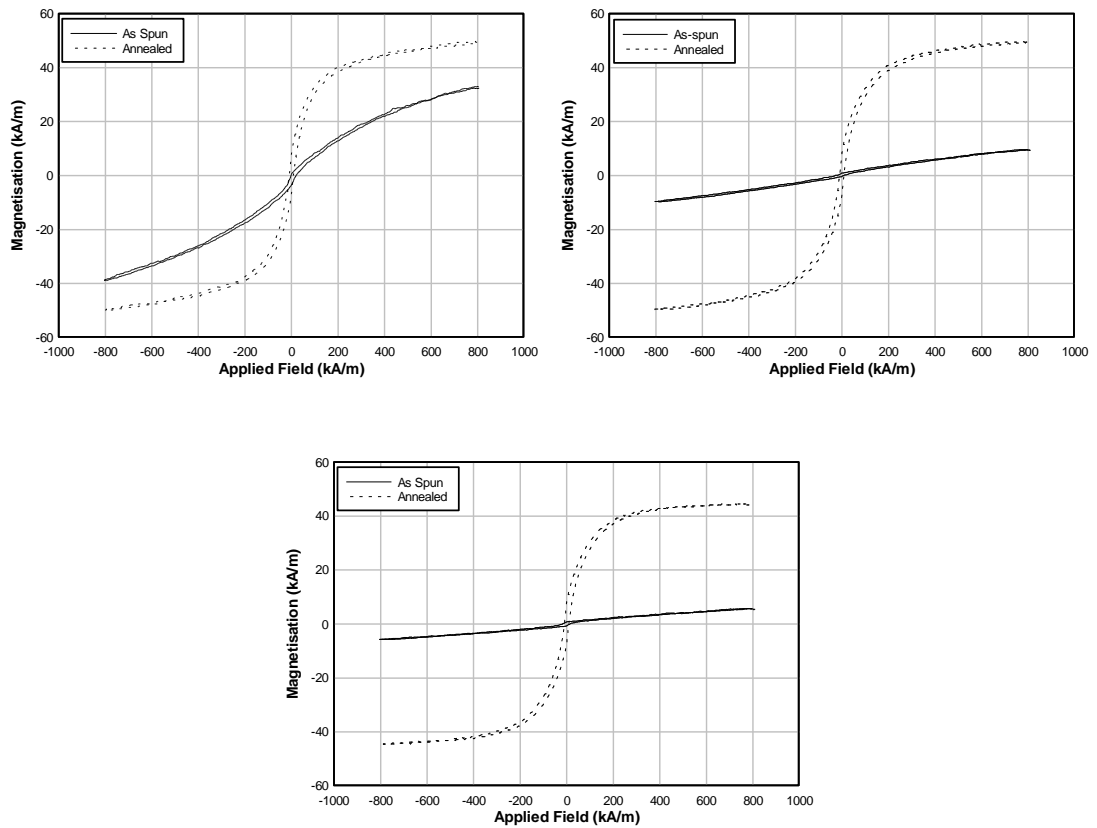


Figure 4.27 Magnetisation curves of Ni-Fe-Al samples, nos. 1 (top left), 2 (top right), 3 (bottom) showing the effect of annealing at 700°C for 2 hours

All three samples show a marked increase in saturation magnetisation on annealing with the annealed samples having approximately the same saturation magnetisation. The as-spun ribbons 2 and 3 look paramagnetic in nature as a result of the cast-in stresses and random atomic order. However sample no.1 shows almost ferromagnetic behaviour even in the as-spun state, probably as a result of the increased iron content. The stresses are removed and a significant amount of recrystallisation occurs on annealing leading to the increased

saturation magnetisation in these ribbons and the much lower field required to saturate them.

4.3.3 Crystal Structure

All three of the samples were in a pure BCC phase in the as-spun state which is shown by Figure 4.28. All of the peaks present can be explained by the heusler cubic structure; the first peak (200) at 31° verifies the Heusler structure; the others are the (220), (400) and (422) reflections.

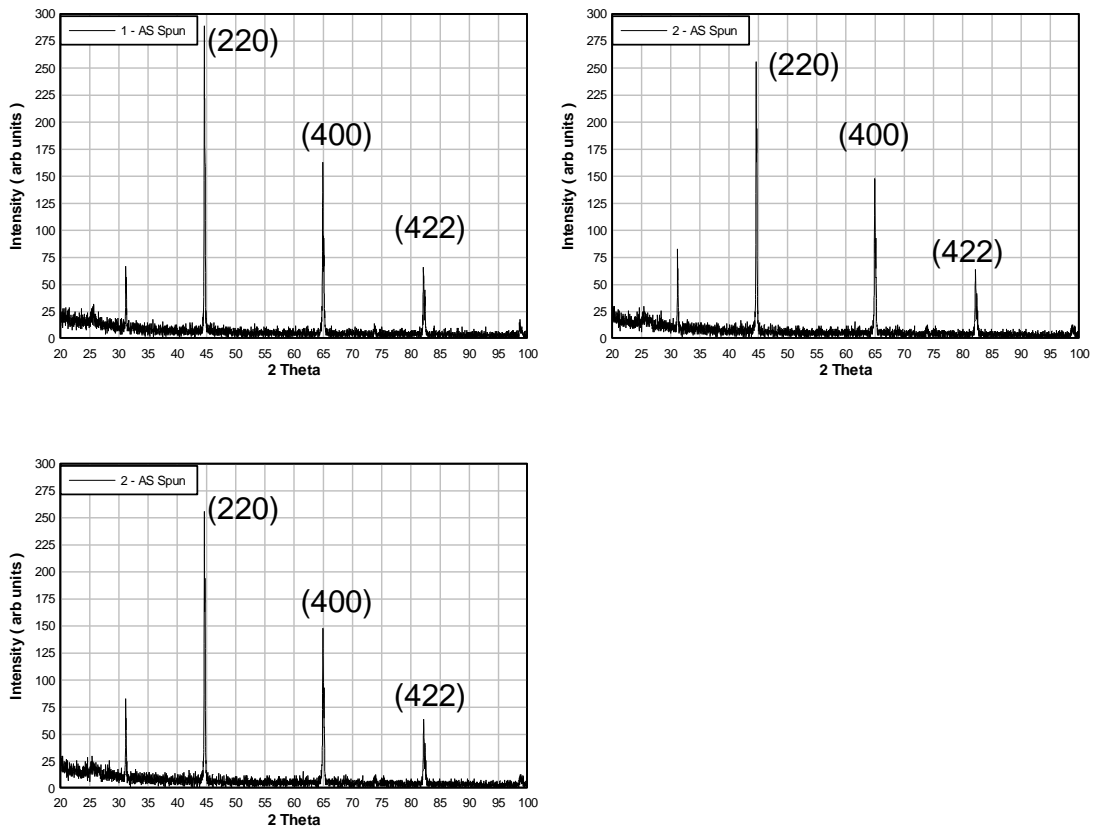


Figure 4.28 XRD patterns showing the Ni-Fe-Al samples 1,2 and 3 in the 'as spun' state

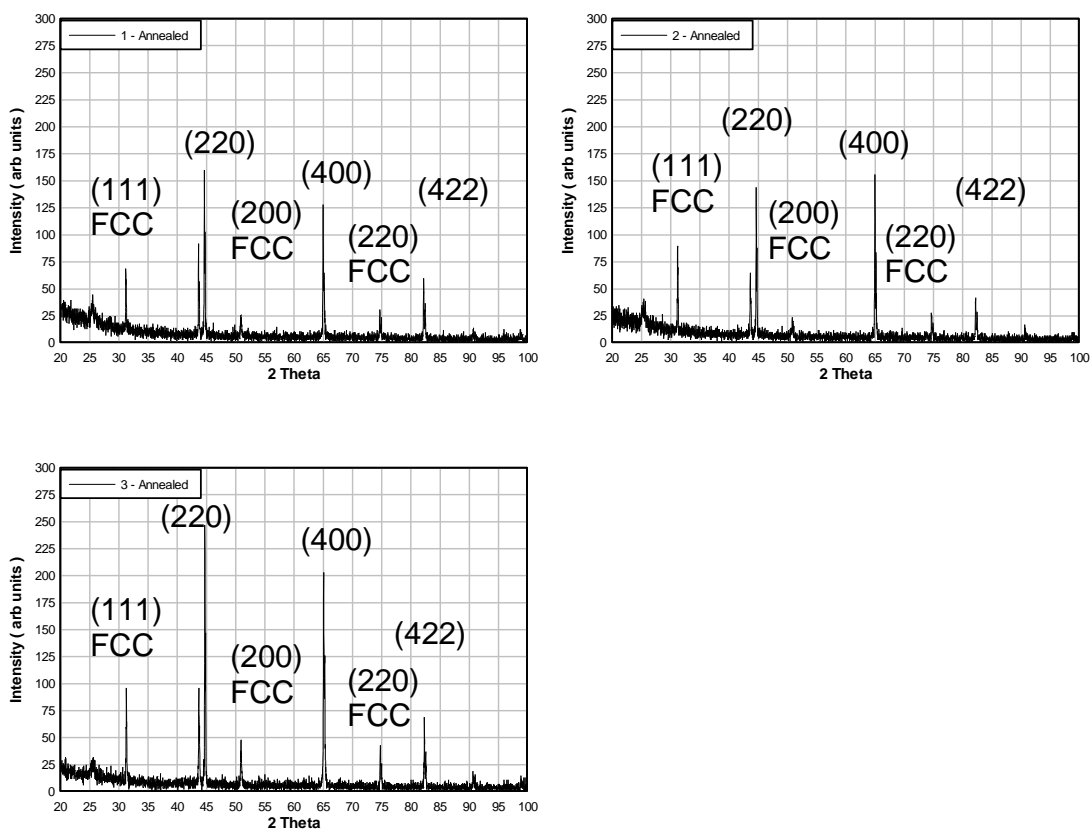


Figure 4.29 XRD patterns of the Ni-Fe-Al samples annealed at 700°C for 2 hours

The annealed samples however show a significant proportion of a second FCC phase present that affects the ability of the material to exhibit the shape memory effect since it is only the BCC phase that exhibits the martensitic transformation. The lattice parameters are shown in Table 4.8. The presence of the FCC phase essentially blocks the transformation in its vicinity because it is non compliant and provides stress large enough to prevent the martensitic transformation occurring in the material around it. This is a difficult problem to overcome

because the BCC as-spun ribbons have a lot of cast-in stress and only have short range atomic order and small crystallites <1 μ m. Larger crystallites, longer range order and a small residual stress are required for the shape memory effect to be displayed. The only method available to achieve this is annealing, but this results in a significant amount of the FCC phase being formed. The stress can be relieved at around 400 $^{\circ}$ C which is not high enough for recrystallisation. This material system was abandoned because it is not possible to anneal it without forming significant amounts of the FCC phase that inhibits the shape memory effect.

Ni-Fe-Al Sample no.	BCC lattice parameter (nm)	FCC lattice parameter (nm)
1 Ni₄₈Fe₂₅Al₂₇	0.573	N/A
1 Ni₄₈Fe₂₅Al₂₇ (700$^{\circ}$C)	0.572	0.360
2 Ni₅₀Fe₂₃Al₂₇	0.576	N/A
2 Ni₅₀Fe₂₃Al₂₇ (700$^{\circ}$C)	0.575	0.359
3 Ni₅₂Fe₂₁Al₂₇	0.572	N/A
3 Ni₅₂Fe₂₁Al₂₇ (700$^{\circ}$C)	0.574	0.360

Table 4.8 Lattice parameters of Ni-Fe-Al melt spun ribbons, before and after annealing at 700 $^{\circ}$ C for two hours

4.4 Sputtered Ni-Fe-Ga

Thin films of ferromagnetic shape memory alloys have the potential to be very useful for micro-electro-mechanical systems (MEMS). They could provide actuation on a very small scale with strains much larger than anything currently available providing the crystalline structure can be controlled with appropriate growth conditions and post growth treatments. Currently much work has focused on the production of thin films of Ni-Mn-Ga by sputtering[6, 17] and laser deposition[18] but there have been no attempts to grow a film of the ferromagnetic shape memory alloy Ni-Fe-Ga which is the focus of this work.

4.4.1 Sample Preparation

A 99.99% nickel sputtering target was used. In order to produce films of variable composition, chips of $\text{Fe}_{40}\text{Ga}_{60}$ and Fe were attached to the top of it with silver paint to provide satisfactory thermal conductivity. The iron chips were made by simply crushing several pieces of 99.9% Iron wire in a 10 Ton press to make flat chips. The chips of iron gallium were made by induction heating of 99.9% pure elements in a 12mm diameter quartz tube with 99.998% Argon atmosphere and then slicing them up using a spark erosion technique into slices around 3mm thick. An alloy with a higher gallium content, $\text{Fe}_{30}\text{Ga}_{70}$ was attempted first to give more flexibility in the film composition but the alloy expanded greatly on cooling making it dangerous to attempt to cast it in a quartz tube because it shatters the quartz. The resulting alloy when made in an arc furnace is shown in Figure 4.30.

It was also extremely brittle and making chips out of it would have been very difficult.



Figure 4.30 Ingot of $\text{Fe}_{30}\text{Ga}_{70}$ after arc melting under Argon and cooling

Initially the Trimag system was used to produce thin films but this produced contamination of up to 5% of Chromium in the deposited films which is clearly not acceptable. It appeared that a significant portion of the stainless steel housing was sputtered in addition to the target for unknown reasons. Hence the 3" magnetron replaced the Trimag for the production of all subsequent films. The 3" magnetron did not contaminate the film within the detection limits of EDX.

Initially the amount of chips required was estimated by using the ratio of surface areas of the target and chips along with the required compositions to give the

desired film composition. For each film the actual number of chips of Fe-Ga and Fe was varied by trial and error with a EDX composition analysis performed to optimise the arrangement and amount of the chips. An initial TEM composition analysis was used to set the correct amount of Fe and Fe-Ga chips. Copper TEM grids with a 100nm carbon film over the holes was used as a substrate because of the cost and ease of use as compared with other TEM compatible substrates. Glass microscope slides and 50nm thick Silicon Nitride membranes were used as substrates following this initial composition analysis and testing.

4.4.2 Films on glass microscope slides

Five Films were deposited onto 150 μ m thick glass microscope slides at room temperature with different compositions. The chamber was evacuated to $< 5 \times 10^{-6}$ mbar prior to deposition and the films were deposited for 10 minutes with a sputtering power of 95W. Seven 12mm diameter Fe-Ga chips were attached to the magnetron target with silver paint for the first film and for each successive film, one of the Fe-Ga chips was replaced with an Fe one of similar size to create a series of films substituting Iron for Gallium. A film on a carbon coated TEM grid was also deposited prior to deposition on the glass slide to obtain a composition analysis using EDX. Part of the film on glass was dissolved in aqua regia and analysed with ICPS to verify the accuracy of the EDX measurement. Both techniques agreed to within 1%. Hence EDX of a film on a carbon coated TEM grid is a suitable method to estimate the composition of the film on the glass substrate. It was also found that the composition on the TEM

grid was the same as that on the subsequent deposition only if the target was cleaned by sputtering for 5 minutes prior to deposition of both films.

Sample ID	No of FeGa chips	Ni (at%)	Fe (at%)	Ga (at%)
G3	3	40.5	19.5	40.0
G4	4	49.9	24.2	25.9
G5	5	53.6	26.5	19.9
G6	6	54.0	30.8	15.2
G7	7	55.5	31.4	13.1

Table 4.9 Composition of the Ni-Fe-Ga films deposited onto glass substrates.

Table 4.9 shows how the film composition varies as Fe chips are substituted for Fe-Ga discs. It is clearly seen that the Gallium content reduces as the substitution is made. The nickel content also increases down the series, probably because the pure Fe is harder to sputter than Fe-Ga. The film G3 was the first film to be deposited after the chips were attached to the Nickel target and has a particularly high Ga content (40%) which suggests that the 5 minutes of pre-deposition cleaning was not enough to establish an equilibrium. The fresh surface of the target was preferentially depleted of Gallium before establishing an equilibrium state where stoichiometric transfer occurs between target and film.

All five of these films proved to be slightly paramagnetic when analysed in the VSM. This suggests that the films were amorphous/nanocrystalline because they were deposited at room temperature. The films were then annealed for 2

hours at 500°C under 500 mbar of argon in order to crystallise and relieve stress. The surface of the films remained shiny and not tarnished after the heat treatment. 500°C was chosen as it was approximately the highest temperature that the glass could stand without deforming. The annealed films showed some more interesting magnetic properties, shown in Figure 4.31. Sample G3 is slightly paramagnetic which is unsurprising due to the large (40%), non-magnetic Gallium content. Samples G4, G5, G6 and G7 are ferromagnetic with increasing saturation magnetisation and decreasing coercivity throughout the series. Iron has a large magnetic moment so it is expected that substitution of Iron for Gallium will increase the overall magnetic moment which is as observed. The decreased coercivity is attributed to the formation of Ni-Fe phases at low Gallium concentrations. Alloys of Nickel and Iron, commonly known as permalloy, are very soft magnetic materials with very high permeability and low coercivity[19]. Samples G4 and G5 have coercivity in the range 5-10kA/m which is similar to that of the melt spun Ni-Fe-Ga ribbons suggesting a similar magnetic structure as would be expected.

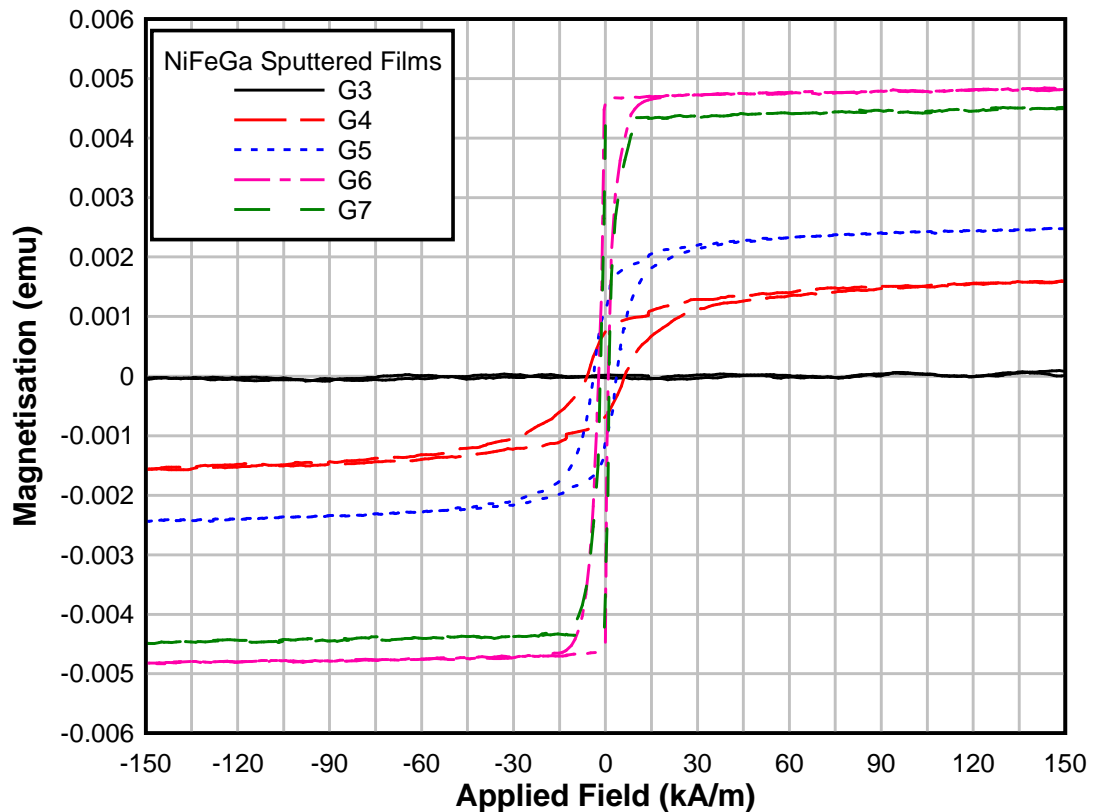


Figure 4.31 Hysteresis loops of the sputtered Ni-Fe-Ga films annealed at 500°C for 2 hours

Figure 4.32 confirms that the magnetic properties of the films are strongly linked to the crystal structure, with the expected BCC phase being present only in films G4 and G5, identified by the peak at 45°. This corresponds to the BCC phase seen in the Ni-Fe-Ga melt spun ribbons. Films G4 and G5 that contain the BCC phase showed a similar hysteresis loop to the melt spun Ni-Fe-Ga and Ni-Mn-Ga ribbons in the austenite phase suggesting that this is the same phase that is present in the melt spun ribbons of Ni-Fe-Ga. Sample G3 which is paramagnetic does not show the BCC phase, and neither do films G6 and G7 which are

strongly ferromagnetic with very low coercivity. The large peak at 29° is present on the blank glass slide as well and is attributed to the glass. The other peaks are not consistent with the melt spun Ni-Fe-Ga and are of unknown origin but are probably from a mixture of NiFe, NiGa and FeGa precipitates. The paramagnetic nature of G3, despite the XRD data looking similar to G5 and G6 can be explained by the large concentration of Gallium that would disrupt the exchange interaction responsible for ferromagnetism in these alloys.

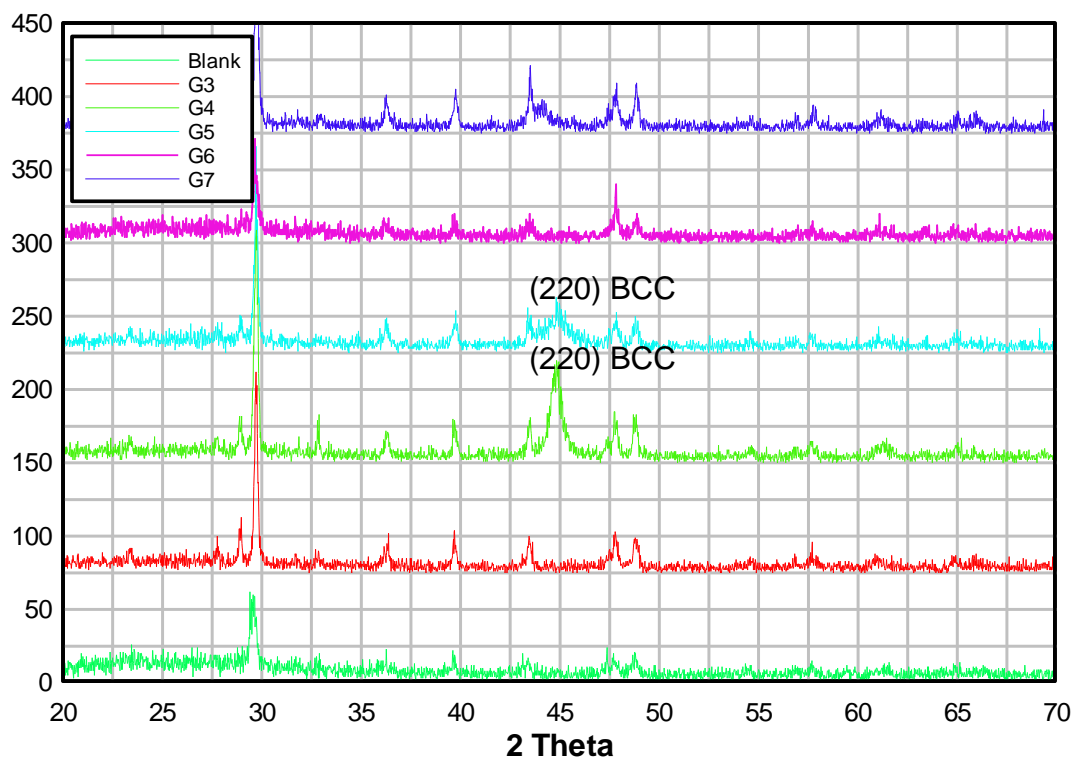


Figure 4.32 XRD patterns of the annealed Ni-Fe-Ga films deposited on glass microscope slides.

Field cooling measurements in the VSM were performed to determine any transformation temperatures below room temperature but none of these films exhibited the ferromagnetic shape memory effect on cooling. This is likely because the films are constrained by the substrate and this stabilises the cubic phase on cooling as a result of stress at the interface.

4.4.3 Films on Silicon Nitride Membranes

Silicon Nitride membranes offer a simple and effective method of depositing a thin film for analysis in a TEM. These are 3mm discs of silicon with a 50nm thick SiN membrane on top. A 0.5 x 0.5mm hole is etched from the back to provide a free standing film. It is also possible to deposit the films at elevated temperatures without risking cracking of the substrate, unlike with glass substrates.

Several films were deposited onto SiN membranes at room temperature, 500, 600, 700 and 800°C to investigate the effect on crystal structure and composition. The temperature was measured with a thermocouple on the back of the heater which gives a reading to within 5% precision as confirmed by putting a thermocouple on the front and back simultaneously to establish the accuracy. The temperature at the membrane is likely to be slightly lower, but there was no method available to accurately measure it. The silicon substrate was tightly pressed to the heater giving good thermal contact and at

temperatures of >600°C it appeared to glow the same colour as the heater beside it so the temperature was estimated to be within 50°C.

Sample ID	Deposition Temp (°C)	Ni (at%)	Fe (at%)	Ga (at%)
1	25	53.4	19.1	27.5
2	500	52.5	20.4	27.1
3	600	52.0	20.8	27.2
4	700	52.1	21.8	25.9
5	800	52.1	22.1	25.8

Table 4.10 Composition analysis of the films deposited on SiN membranes at elevated temperatures

All of the films were deposited under the same conditions with the aim of achieving a composition of $\text{Ni}_{53}\text{Fe}_{20}\text{Ga}_{27}$, a composition known to exhibit the shape memory effect[13]. The chamber was pumped to $< 10^{-5}$ mbar prior to deposition and the target cleaned for 5 minutes whilst covered by the shield. Sputtering power was 95W for all 5 films.

Table 4.10 shows the measured compositions of the deposited films illustrating the point that Gallium is lost from the film at temperatures exceeding 600°C due to its vapour pressure being larger than the Nickel and Iron. EDX analysis also gave an indication of the oxygen content of the films which is a good indicator as to the state of the vacuum system and the gas purity. All of the films had a low

oxygen content in the range of 1.5-3 at%. It is not certain whether the mild oxidation of the films was due to oxygen in the chamber or if it happened as they are returned to atmosphere.

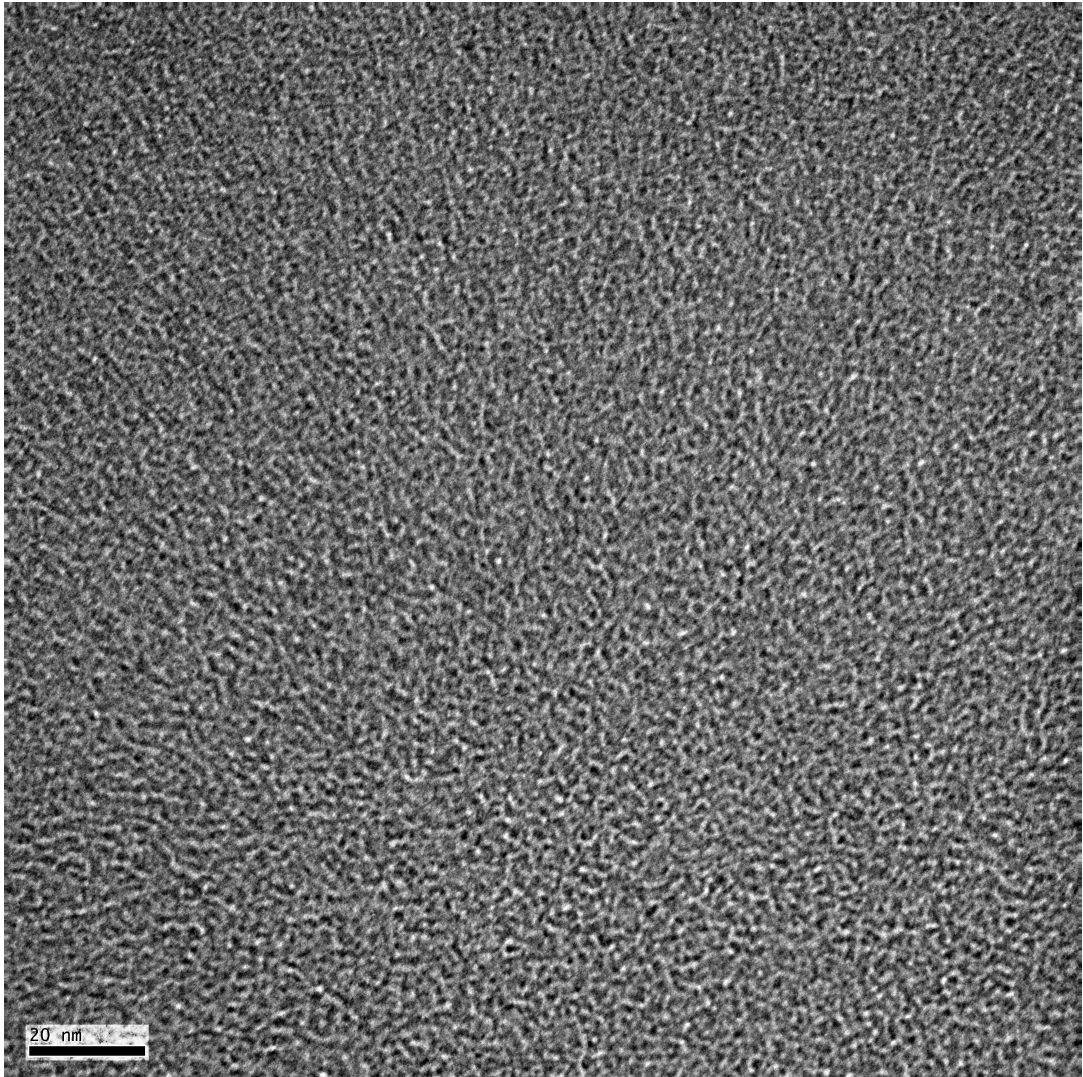


Figure 4.33 TEM image of the Ni-Fe-Ga film deposited at 25°C

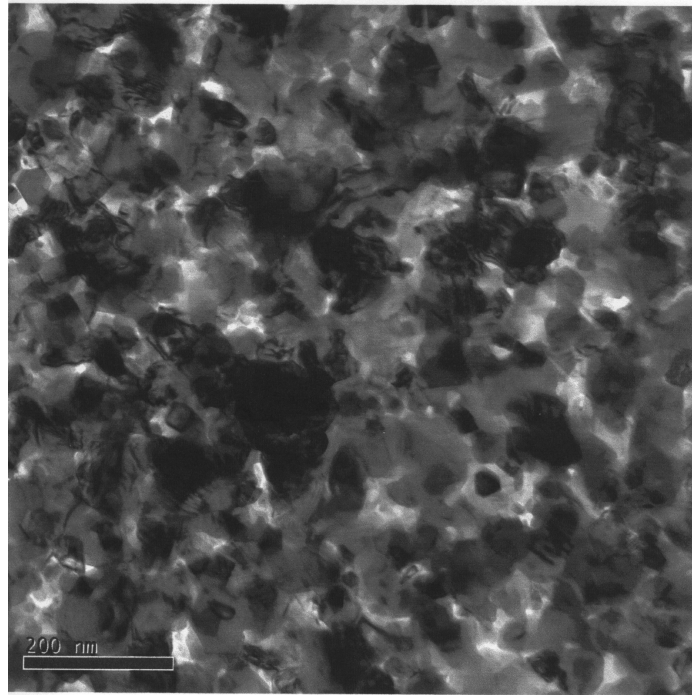


Figure 4.34 TEM image of the Ni-Fe-Ga film deposited at 500°C

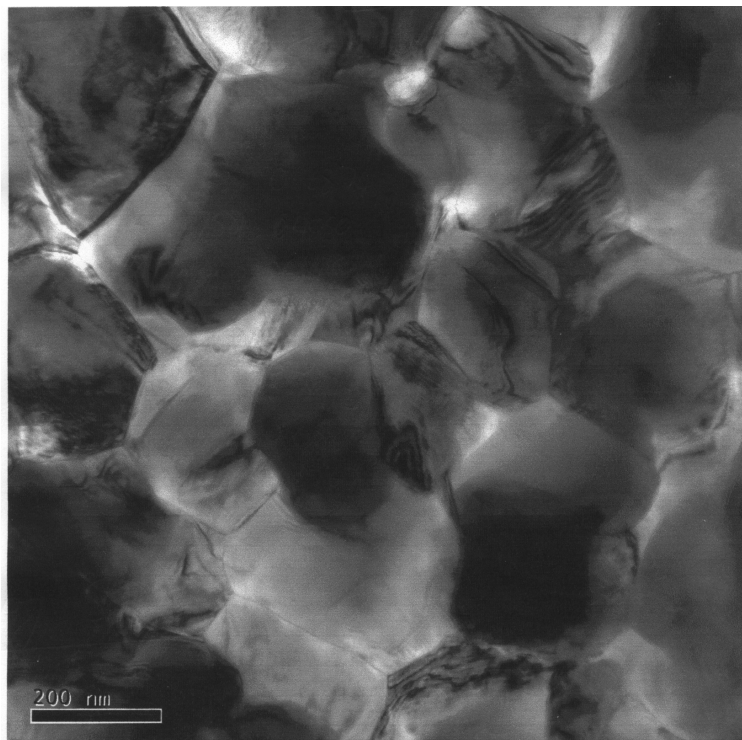


Figure 4.35 TEM image of the Ni-Fe-Ga film deposited at 600°C

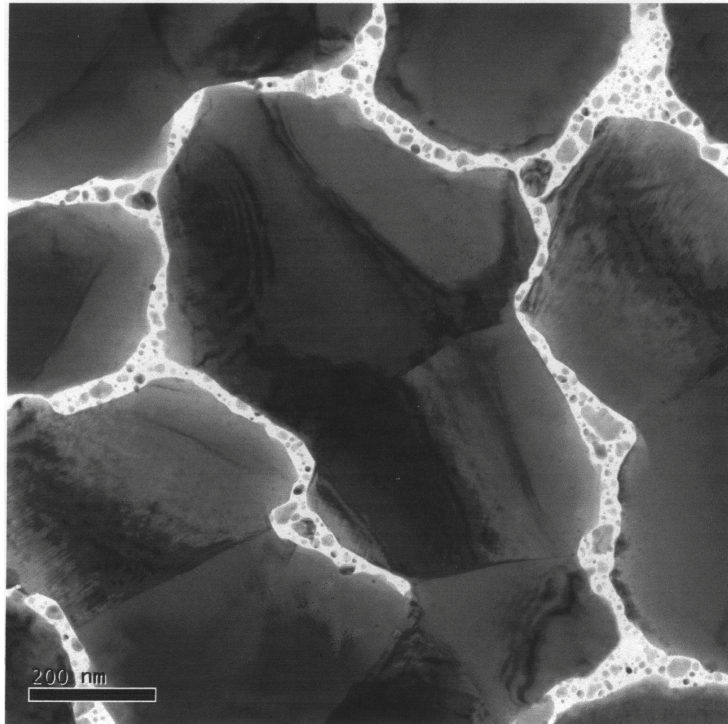


Figure 4.36 TEM image of the Ni-Fe-Ga film deposited at 700°C

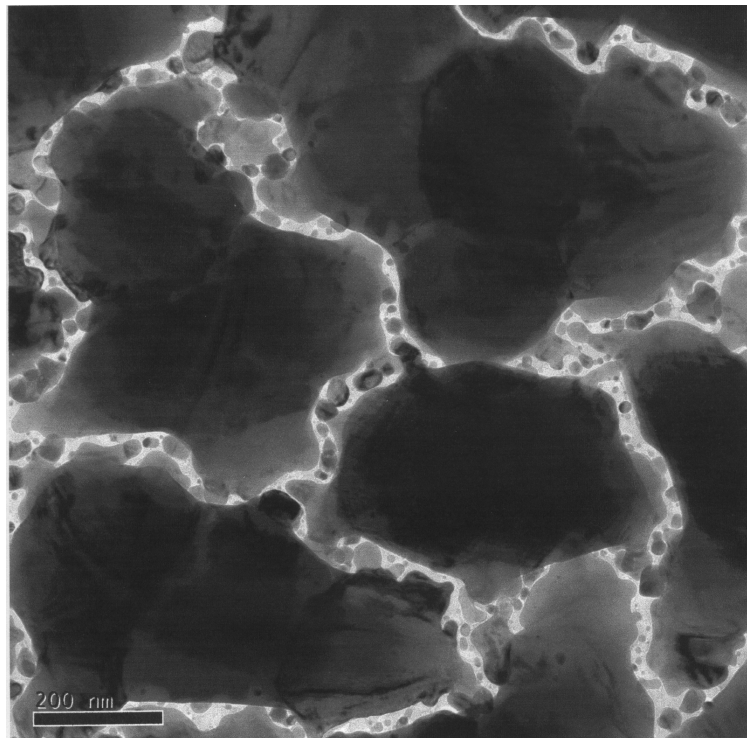


Figure 4.37 TEM image of the Ni-Fe-Ga film deposited at 800°C

Figure 4.33 shows that the film deposited at room temperature is nanocrystalline with no large crystal grains; there are no grains larger than a few nm. This is largely expected as a result of the low mobility of atoms as they condense onto the cold substrate with the structure being nanocrystalline or amorphous. As the deposition temperature is increased, the grain size increases dramatically to ~100nm in diameter at 500°C (Figure 4.34). At 600°C the largest grains are approximately 400nm in diameter and the trend continues with ~500nm grains at 700°C and 600-700nm grains at 800°C. All films deposited onto SiN substrates in this fashion have such small crystals because the SiN membrane itself is an amorphous structure. In order to achieve single crystalline films a lattice matched substrate must be used to promote growth of the BCC phase along a certain crystallographic direction dependent on the lattice parameter of the substrate.

It was attempted to obtain selected area diffraction patterns of these crystallites but this proved to be not possible because of their small size. So diffraction patterns were taken of a large area of the film giving the standard ring patterns from many crystallites simultaneously. These patterns illustrated that the films all contained the BCC phase, with the 700°C and 800°C films containing an FCC phase as well. This result ties in well with what was observed with the melt spun NiFeGa ribbons that also formed an appreciable amount of an FCC phase when annealed at temperatures over 700°C. The lattice parameters observed from the TEM are shown in Table 4.11. These lattice parameters show a slightly

increased lattice parameter at 700°C and 800°C, the same as the melt spun ribbons, but measuring these in the TEM incurs a larger error than XRD with a typical error of this system being +/- 0.003nm. Lattice parameters are the same as those obtained for the melt spun ribbons of Ni-Fe-Ga to within experimental error, suggesting that the films have the same crystal structure.

Sample ID	Deposition Temperature(°C)	BCC lattice parameter (nm)	FCC lattice parameter (nm)
1	273	0.576	N/A
2	500	0.579	N/A
3	600	0.577	N/A
4	700	0.580	0.363
5	800	0.581	0.367

Table 4.11 Lattice parameters of the films deposited on SiN membranes calculated from TEM diffraction patterns.

4.4.4 Summary and Conclusions

Films of Ni-Fe-Ga that have the crystal phase necessary for the shape memory effect have been successfully grown on both glass microscope slides and on silicon nitride membranes. The composition range necessary for the shape memory effect to occur has also been obtained in the films deposited on Silicon Nitride membranes.

Of the 5 films on glass microscope slides only two, G4 and G5 showed the BCC phase, determined by XRD. The magnetic measurements showed G4 and G5 to

have a similar hysteresis loop to the melt spun ribbons of Ni-Fe-Ga also suggesting that the austenitic phase was present. G4 and G5 both had a few percent too much Iron for them to exhibit the shape memory effect and field cooling in the VSM did not show any martensitic transition between room temperature and 77K. This could also be due to the clamping action of the substrate but this could not be determined. Film G3 on glass had 40% Gallium, much higher than the target range of 18-26%, which resulted in a paramagnetic film which did not show the expected BCC phase required for the shape memory effect. The large Gallium content was attributed to inadequate conditioning of the target prior to deposition and the preferential sputtering of Gallium before an equilibrium was established. The other films on glass showed a magnetically soft phase, probably due to the large Iron content and reduced Gallium.

All of the films deposited upon silicon nitride membranes showed the cubic phase with the slight increase of lattice parameter in the films deposited at 700°C and 800°C, similar to the Ni-Fe-Ga melt spun ribbons that showed the same effect in the ribbons annealed at similar temperatures. The films deposited at > 700°C also showed the FCC phase with similar lattice parameter to that seen in the Ni-Fe-Ga melt spun ribbons. None of the ribbons however showed the martensitic phase at room temperature and it was not possible to examine these films below room temperature. Magnetic measurements in the VSM were not able to show any shape memory effect in the films deposited on silicon nitride because the magnetic moment of these films was below the detection limit of the VSM.

4.5 Ni-Mn-Ga Films produced by Pulsed Laser Deposition

It was attempted to produce Ni-Mn-Ga films on glass and SiN membranes by the process of pulsed laser deposition using a Questek 2000 series Excimer laser which could be run with KrF or ArF gas mixtures, giving output at 248nm or 193 nm respectively. This was done in a vacuum chamber that was pumped with an oil diffusion pump with a liquid nitrogen trap to achieve pressures of $<10^{-5}$ mbar. The target was a $\text{Ni}_{52.1}\text{Mn}_{26.5}\text{Ga}_{21.4}$ alloy purchased from Adaptamat Ltd and sliced into suitable sized pieces with a spark eroder.

4.5.1 Initial Deposition

The purpose of the first few depositions was to give an indication of the deposition parameters that would likely be successful. The aim was to produce pure, non-oxidised films of the same composition as the target with large crystallites. For TEM analysis films of 100nm thickness were desired. The first film was deposited on a SiN membrane under vacuum with a pressure of 1.8×10^{-5} mbar and with the substrate at room temperature. The substrate was positioned at the end of the visible plume, which was 20mm from the target which was polished with $3\mu\text{m}$ lapping paper to give a mirror finish. The laser was operated with ArF gas at 10Hz for 60s giving 600 shots with a fluence on the target of $4.7\text{J}/\text{cm}^2$. The chamber was then vented to atmospheric pressure with

Nitrogen. The SiN membrane was removed and stored in a vacuum until it was taken for analysis in the TEM.

EDX analysis in the TEM showed a measured composition of $\text{Ni}_{36.5}\text{Mn}_{40.4}\text{Ga}_{23.1}$, a large deficiency in Nickel content and excess of Manganese. Gallium was only slightly higher than expected. A large Oxygen content corresponding to 33at% of the film was detected which indicated a possible leak in the vacuum chamber. This prompted the replacement of all removable seals in the system and a subsequent leak test. This analysis demonstrated the need to ablate the polished target with several 100's of shots before beginning the deposition process in order to allow an equilibrium to be established whereby stoichiometric transfer can be achieved. It also prompted a spectroscopic analysis of the plume to determine how many shots are necessary to establish this equilibrium.

4.5.2 Spectroscopic analysis of the ablation plume

An Ocean Optics USB4000-UV-VIS fibre spectrometer was used to capture the spectrum of the ablation plume. A lens was placed outside the observation window to focus the light from the plume onto the end of the fibre input to maximise the light transferred to the spectrometer and give the largest signal possible. The target was polished to a mirror finish and the windows cleaned prior to obtaining these spectra to recreate the conditions of the initial film deposition described above. The laser was fired at a repetition rate of 10Hz and the spectrometer set to capture a spectrum every 2 seconds. Unfortunately the

laser output was much reduced to begin with and could not be improved with several refills of ArF gas mixture. The laser was then filled with a KrF gas mixture, giving a more reliable output at 248nm.

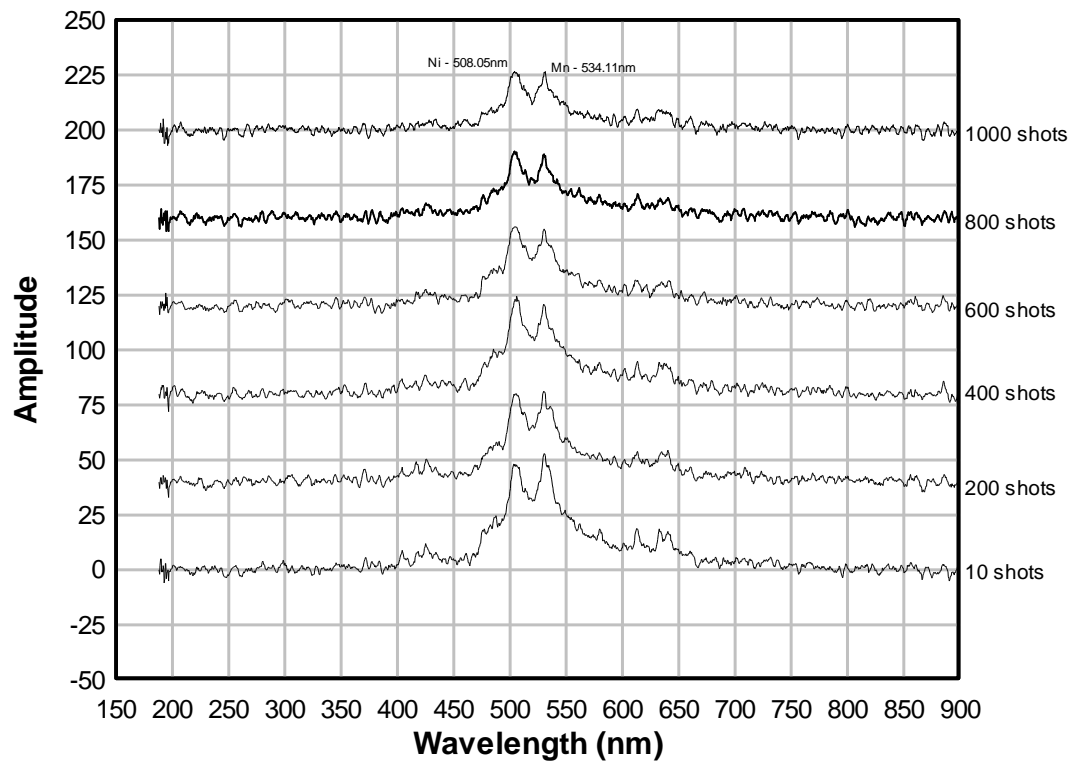


Figure 4.38 Emission spectra of the ablation plume for a Ni-Mn-Ga target as the deposition process progresses. This shows the gradual reduction of Mn content and an increase of Ni, supporting the composition analysis of the first film. Ni and Mn peaks shown are the more intense spectral lines from[20].

Figure 4.38 shows the evolution of the ablation plume as the deposition progresses, where the two large peaks are from atomic Nickel and Manganese as marked on the graph. It can clearly be seen that the relative intensities of these two peaks changes over the first 400 shots and then remains constant from 600 – 1000 shots, explaining the composition anomaly of the first film. It is expected that firing 1000 shots onto the target prior to exposing the substrate would result in stoichiometric transfer and this was indeed the case.

4.5.3 Films on SiN membranes

Following the spectral analysis the target was polished and then ablated for 1000 shots before deposition of all of the following films. Films of Ni-Mn-Ga were deposited onto SiN membranes at room temperature, 500, 600 and 700°C to investigate the changes in crystal structure that result from changing the substrate temperature.

Sample ID	Substrate Temperature (°C)	Fluence (J/cm²)	Deposition Time (no. of shots)
1	25	4.0	2400
2	500	4.4	2400
3	600	4.3	2400
4	700	4.2	2400

Table 4.12 Deposition parameters for the films deposited onto SiN membranes

All of these films were opaque to visible light after around 1000 shots and they were still transparent to the electron beam in the TEM suggesting a thickness of 100-200nm.

Figure 4.39 shows the effect of depositing a film at room temperature, where the grains are very small, < 50nm and the diffraction pattern shows that this film is amorphous without a well defined crystal structure. This is expected from a film deposited at low temperature because of the low mobility of the adsorbed atoms. EDX identified the large blob on this picture as being carbon which was also identified on the other films. The most likely origin of this was back streaming from the oil diffusion pump but this cannot be definitively identified as the cause. Figure 4.40 shows the film deposited at 500°C which has crystal grains of 50nm – 100nm, significantly larger than in

Figure 4.39. The evenly spaced diffraction rings indicate that this is a BCC structure with lattice parameter of 0.564nm as is expected for the Ni-Mn-Ga system. Figure 4.41 shows the film deposited at 600°C which has a typical grain size of 50nm – 100nm and the diffraction pattern showed the equally spaced rings from a BCC structure with lattice parameter of 0.572nm. Figure 4.42 shows the film deposited at 700°C which is very similar in structure to those deposited at 500°C and 600°C with typical grains in the region 50nm – 100nm. The associated diffraction pattern also showed the BCC structure with lattice parameter 0.569nm. The lattice parameters obtained from these diffraction patterns were obtained by measuring the distances on the imaged features using the TEM software. It was a manual system and subject to a degree of ambiguity

as to where the center of each line is which introduces error. There was a degree of astigmatism in the imaging system leading to the rings being slightly oval which also introduces a small error. Taking these into account the system is expected to have an error of around 2%, an order of magnitude greater than XRD. This error is probably the reason that the lattice parameters are 0.02nm smaller than the melt spun ribbons and no conclusions can be drawn from the slightly reduced lattice parameter.

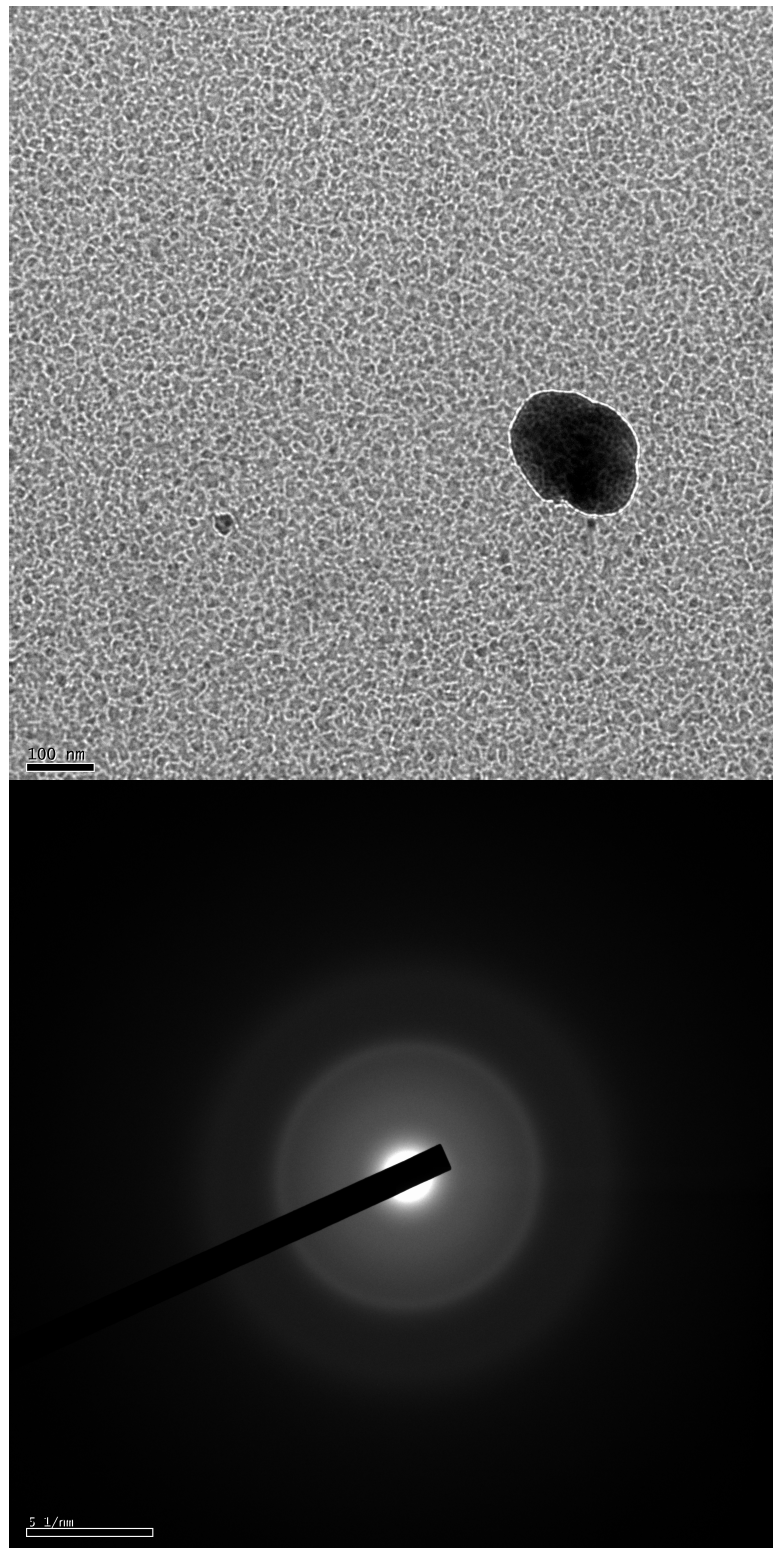


Figure 4.39 TEM image and diffraction pattern of film1 deposited at 20°C

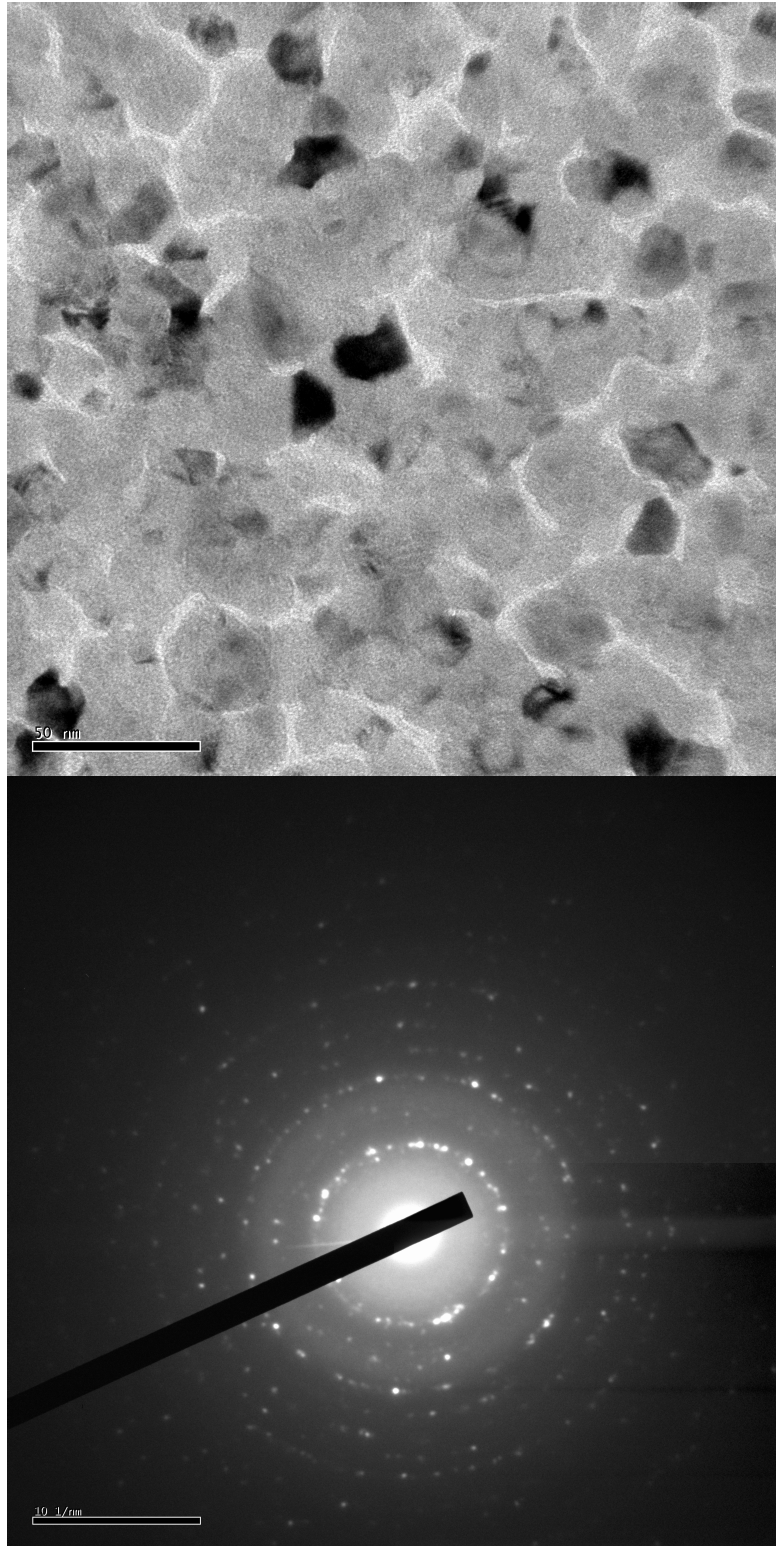


Figure 4.40 TEM image and diffraction pattern of film2 deposited at 500°C

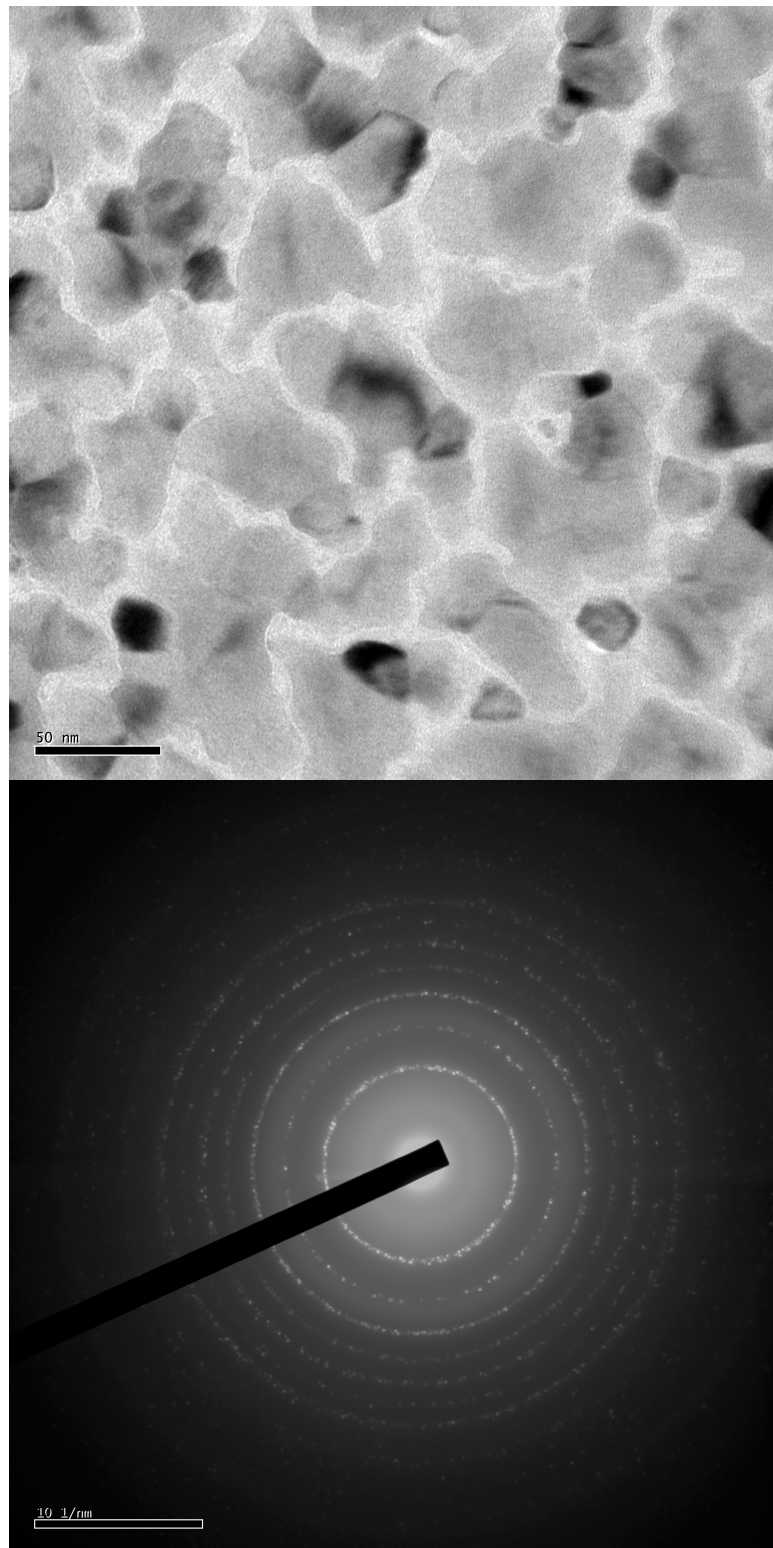


Figure 4.41 TEM image and diffraction pattern of film3 deposited at 600°C

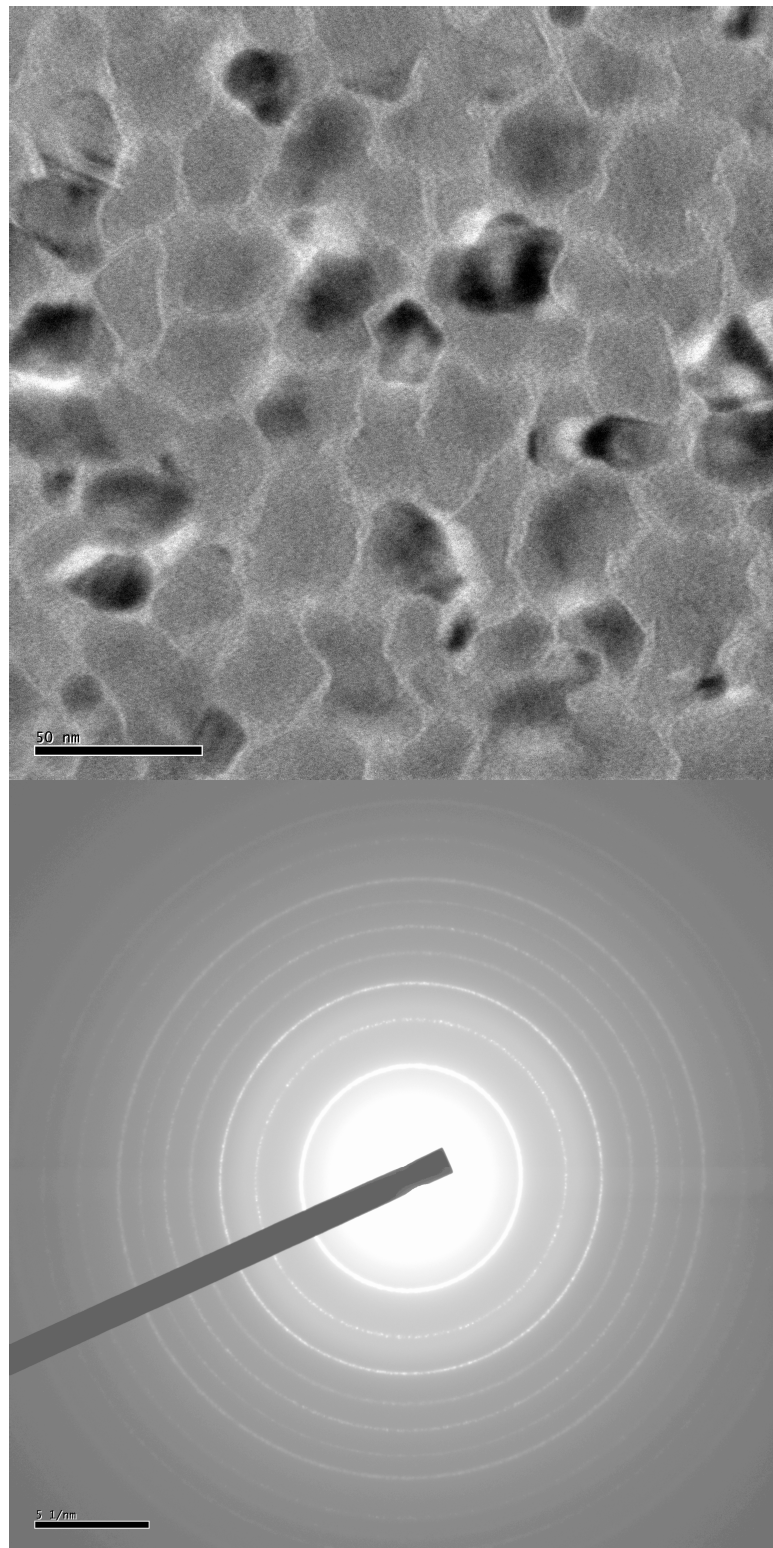


Figure 4.42 TEM image and diffraction pattern of film4 deposited at 700°C

Sample (Deposition Temp (°C))	Ni (at%)	Mn (at%)	Ga (at%)	O (at%)
1 (25)	36.2	37.5	26.3	32
2 (500)	46.5	29.4	24.1	28
3 (600)	47.6	28.4	23.8	31
4 (700)	48.1	30.4	21.5	29

Table 4.13 The composition of Ni-Mn-Ga films deposited onto SiN membranes from a $\text{Ni}_{52.1}\text{Mn}_{26.5}\text{Ga}_{21.4}$ target. Composition was determined by EDX analysis. Ni, Mn, Ga values are given exclusive of the oxygen content.

Table 4.13 shows the large Manganese content in film 1 as the equilibrium was established, it was this result that led to ablating the target for 600 pulses before deposition. The other films show approximately the same composition as one another to within the error of the EDX system (+/- 1%). Films 2-4 also show near stoichiometric transfer from the target which allows the desired composition to be obtained. All of the films however show a large proportion of Oxygen is present, amounting to >28% for all films. This level of oxygen in the films is unacceptable and explains why the films looked discoloured on removing them from the chamber.

4.5.4 Discussion and Summary.

Films of Ni-Mn-Ga have been deposited onto Silicon Nitride membranes using PLD. The films deposited at 500°C and above showed the BCC structure that is characteristic of Ni-Mn-Ga alloys. The lattice parameter was 0.02nm lower than

that observed for the Ni-Mn-Ga melt spun ribbons but that is within the experimental error so no conclusions can be drawn from this data. Despite best efforts to produce pure films by this method the deposited films contained a large proportion of Oxygen. The deposition chamber was stripped and cleaned and every seal replaced and leak tested but there was no significant reduction in the oxygen content of the deposited films suggesting that it was either outgassing from somewhere or that it was back streaming from the oil diffusion pump. This type of pump is not ideal when performing thin film deposition in a high purity atmosphere. The Argon gas bottle was also changed and all the high pressure pipes were checked for leaks but none were found. Because of these problems producing pure films using the available equipment and the inability to suitably modify the chamber this technique was abandoned as a production method.

4.6 References

- [1] X. Jin, M. Marioni, D. Bono, S. M. Allen, and R. C. O'Handley, "Empirical mapping of NiMnGa properties with composition and valence electron concentration," *J.Appl.Phys*, vol. 91, pp. 8222-8224, 2002.
- [2] R. C. O'Handley, "Model for strain and magnetisation in magnetic shape memory alloys," *J.Appl.Phys*, vol. 83, pp. 3263-3270, 1998.
- [3] V. V. Khovailo, T. Takagi, A. N. Vasilev, H. Miki, M. Matsumoto, and R. Kainuma, "On order-disorder (L2(1) \rightarrow B2') phase transition in Ni_{2+x}Mn_{1-x}Ga Heusler alloys," *Phys Stat. Solidi A*, vol. 183, pp. R1-R3, 2001.
- [4] Heczko, O., Lanska, N, Soderberg, O, Ullakko, and K, "Temperature Variation of structure and magnetic properties of Ni-Mn-Ga magnetic shape memory alloys," *J. Magn. Magn. Mater*, vol. 242-245, pp. 1446-1449, 2002.
- [5] O. Heczko, K. Jurek, and K. Ullakko, "Magnetic properties and domain structure of magnetic shape memory Ni-Mn-Ga alloy," *J. Magn. Magn. Mater*, vol. 226-230, pp. 996-998, 2001.
- [6] J. Ahn, N.Cheng, T.Lograsso, and M.Krishnan, "Magnetic properties, Structure and shape memory transitions in Ni-Mn-Ga thin films grown by ion beam sputtering," *IEEE Trans. Mag.*, vol. 37, pp. 2141-2143, 2001.
- [7] S. J. Murray, M. Marioni, P. G. Tello, S. M. Allen, and R. C. O'Handley, "Giant Magnetic-field-induced strain in Ni-Mn-Ga crystals: experimental results and modelling," *J.Magn. Magn. Mat.*, vol. 226-230, pp. 945-957, 2001.

- [8] S. J. Murray, M. Marioni, S. M. Allen, and R. C. O'Handley, "6% magnetic-field-induced strain by twin-boundary motion in ferromagnetic Ni–Mn–Ga," *Appl. Phys. Lett*, vol. 77, pp. 886-888, 2000.
- [9] P. A. Algarabel, C. Magen, L. Morellon, M. R. Ibarra, F. Albertini, N. Magnani, A. Paoluzi, L. Pareti, M. Pasquale, and S. Besseghini, "Magnetic-field-induced strain in Ni₂MnGa melt-spun ribbons," *J. Magn. Magn. Mater*, vol. 272-76, pp. 2047-2048, 2004.
- [10] K. Oikawa, T. Ota, T. Ohmori, Y. Tanaka, H. Morito, A. Fujita, R. Kainuma, K. Fukamichi, and K. Ishida, "Magnetic and martensitic phase transitions in ferromagnetic Ni–Ga–Fe shape memory alloys," *Appl. Phys. Lett*, vol. 81, pp. 5201, 2002.
- [11] z. H. Liu, M. Zhang, Y. T. Cui, Y. Q. Zhou, W. H. Wang, and G. H. Wu, "Martensitic transformation and shape memory effect in ferromagnetic Heusler alloy Ni₂FeGa," *Appl. Phys. Lett*, vol. 82, pp. 424-426, 2003.
- [12] K.Oikawa, T.Omori, R.Kainuma, and K.Ishida, "Effects of annealing on martensitic and magnetic transitions of NiFeGa ferromagnetic shape memory alloys," *J. Magn. Magn. Mater*, vol. 272-276, pp. 2043-2044, 2004.
- [13] Y.sutou, N.Kamiya, T.Omori, R.Kainuma, and K.Ishida, "Stress-strain characteristics in NiFeGa ferromagnetic shape memory alloys," *Appl. Phys. Lett*, vol. 84, pp. 1275, 2004.
- [14] H.Morito, A.Fujita, K.Fukamichi, R.Kainuma, and K.Ishida, "Magnetic field induced strain of NiFeGa in single variant state," *Appl. Phys. Lett*, vol. 83, pp. 4993, 2003.

- [15] Jiang, Chengbao, Feng, Gen, Gong, Shengkai, XU, and Huibin, "Effect of Ni excess on phase transformation temperatures of NiMnGa alloys," *Mater. Sci. Eng.*, vol. 342, pp. 231-235, 2003.
- [16] N. Lanska, O. Soderberg, A. Sozinov, Y. Ge, K. Ullakko, and V. K. Lindroos, "Composition and temperature dependence of the crystal structure of Ni-Mn-Ga alloys," *J.Appl.Phys*, vol. 95, pp. 8074-8078, 2004.
- [17] M.Ohtsuka, M.Sanada, M.Matsumoto, and K.Itagaki, "Magnetic field induced shape memory in NiMnGa sputtered films," *Mater. Sci. Eng.*, vol. 378, pp. 377-383, 2004.
- [18] F. J. Castano, B. Nelson-Cheeseman, R. C. O'Handley, and C. A. Ross, "Structure and thermomagnetic properties of polycrystalline Ni-Mn-Ga films," *J.Appl.Phys*, vol. 93, pp. 8492, 2003.
- [19] Akhter, M. A, Mapps, D. J, M. Tan, Y. Q, Petford-Long, Amanda, and Doole, "Thickness and grain-size dependence of the coercivity in permalloy thin films," *J.Appl.Phys*, vol. 81, pp. 4122-4124, 1997.
- [20] D. R. Lide, "CRC Handbook of Chemistry and Physics, 77th Edition," CRC Press, 1996, pp. 10-1.

Chapter 5.....Summary and Outlook

The objective of this study was to investigate the production of polycrystalline ferromagnetic shape memory alloys in the form of melt spun ribbons and thin films. Prior to this work, most of the research in this area had focussed on the properties of single crystal alloys which is very useful for understanding the material system. However they are very difficult and expensive to produce which limits their practical uses. For FSMAs to be widely used in industry the more easily manufactured polycrystalline forms of the alloy need to be investigated. This study aimed to address this by investigating the effects of rapid quenching and subsequent heat treatment on the properties of polycrystalline FSMAs.

The combination of X-Ray diffraction and thermomagnetisation measurements were primarily used to deduce the presence of a martensitic transition in the alloys studied. Unfortunately X-Ray measurements were only available at room temperature and so only the room temperature crystal structure could be determined. The thermomagnetisation curves revealed the presence of a martensitic transition because of the large difference in anisotropy between the austenite and martensite phases. This was particularly useful for the Ni-Fe-Ga alloys that had transition temperatures below 223K, the limit of the Differential Scanning Calorimeter that was used in this research..

In this work, melt spinning has been shown to produce ~30µm thick ribbons of Ni-Mn-Ga and Ni-Fe-Ga-Tb that exhibit the shape memory effect. The melt spinning process produces nanocrystalline ribbons with large “cast-in” stresses that inhibit the shape memory effect in all of the ribbons produced. Annealing at temperatures of 400°C was shown to significantly relieve stress and increase the saturation magnetisation. Annealing temperatures of 700 - 800°C were shown to promote crystal growth, with crystals of ~20µm visible under optical microscopy in the annealed ribbons. The combination of increased grain size, increased atomic order and stress relief resulted in some of the annealed ribbons exhibiting a field dependent transformation strain comparable to that shown in [1]. None of the ribbons produced showed a field induced strain, possibly because the internal stresses were too large because of the polycrystalline nature of the ribbons. This could also be due in part to the design of the capacitance cell that could not apply a stress of < 1.5MPa to the ribbons despite significant effort in designing new springs to apply less force. This is less than the blocking stress of single crystal Ni-Mn-Ga but the blocking stress of polycrystalline Ni-Mn-Ga is unknown at present and may be lower.

A significant problem in making polycrystalline FSMAs is the formation of the FCC phase that does not form twins and therefore inhibits the shape memory effect. Formation of this phase was shown to be inhibited by the rapid quenching of melt spinning with none of the ‘as cast’ samples showing any of this phase under XRD analysis. The rapid quenching also ‘cast in’ large stresses which also

inhibits the shape memory effect in these materials. Unfortunately many of the ribbons contained significant amounts of the FCC phase after annealing to remove this stress and re-crystallise the ribbons. An interesting and significant result to come out of this work was that the addition of 1.2% Tb to the Ni-Fe-Ga-Tb samples prevented the formation of the FCC phase, even after annealing at 800°C. This could be potentially useful in creating polycrystalline FSMAs. It is not known if this effect would be present in other alloy systems such as Ni-Mn-Ga, but it would be worth pursuing.

The ferromagnetic shape memory effect has been demonstrated to manifest itself in Ni-Mn-Ga and Ni-Fe-Ga alloys with a valence electron per atom ratio (e/a) of ~ 7.8 [2, 3]. These alloys are brittle and easily broken if handled roughly so it was proposed that a Ni-Fe-Al alloy with e/a ratio of 7.8 may also exhibit the ferromagnetic shape memory effect. A series of Ni-Fe-Al alloys, $\text{Ni}_{52}\text{Fe}_{21}\text{Al}_{27}$, $\text{Ni}_{54}\text{Fe}_{19}\text{Al}_{27}$, $\text{Ni}_{56}\text{Fe}_{17}\text{Al}_{27}$ were produced to investigate this hypothesis. These alloys were shown not to exhibit a martensitic transformation down to 77K by field cooling measurements. Also a significant amount of an FCC phase was formed on annealing making these alloys unlikely to be useful as a shape memory alloy. This material system was abandoned at this point.

Pulsed laser deposition of Ni-Mn-Ga was attempted as a thin film production process. A target of the desired composition was used for this purpose. By observing the emission spectra of the ablation plume it was deduced that the

material transfer was not stoichiometric for the first 500 pulses and that manganese was preferentially ablated in the early pulses, a point that must be considered when using PLD with Ni-Mn-Ga targets. All of the films produced by PLD had a large oxygen content, with EDX showing an oxygen content of up to 50% and a carbon content of > 5% for all films. This high level of contamination was reduced a little by thoroughly cleaning the system and leak testing the chamber. Even after this the contamination was still too great and the PLD chamber was deemed to be unsuitable for further work with Ni-Mn-Ga alloys. It was thought that the main source of contamination was the combination of oil from the diffusion pump and rotary pump. It was clear from this work that an Ultra High Vacuum (UHV) system is required for successful deposition of Ni-Mn-Ga by pulsed laser deposition.

Films of Ni-Fe-Ga that have the crystal phase necessary for the shape memory effect have been successfully grown on both glass microscope slides and on silicon nitride membranes by the process of magnetron sputtering. When sputtering Ni-Fe-Ga from a fresh target it was observed that gallium is sputtered preferentially. In order to get repeatable results and stoichiometric transfer the target had to be cleaned by sputtering for approximately 10 minutes prior to exposing the substrate for deposition. The austenitic BCC phase was observed in XRD patterns from two of the films on glass, but no martensitic transition was observed, probably due to the clamping effect of the substrate. It was expected that the films on the SiN membranes would undergo the martensitic

transformation but this could not be detected because of the limited sensitivity of the VSM and cooling in the TEM was not available. These films did however show the expected crystal structure. However further work with sputter deposited Ni-Fe-Ga films would be worthwhile, since sputtered Ni-Mn-Ga films have been shown to exhibit the ferromagnetic shape memory effect[4]. The next step would be to fabricate free-standing bridges of Ni-Fe-Ga to remove the clamping effect of the substrate. This would allow the film to undergo the martensitic transformation and the shape memory properties could be studied in detail, especially if heating/cooling can be performed in-situ in a TEM.

A significant result of this research was the effect of adding small quantities of Terbium to Ni-Fe-Ga alloys and the effect it had in suppressing the formation of the unwanted FCC phase. This effect warrants further investigation and could lead to further advances in the production of polycrystalline ferromagnetic shape memory alloys. It would be useful to continue to research Terbium addition in the Ni-Fe-Ga system to investigate the cause of the suppressed M_s in the studied alloys and to research more of the composition range that may produce ferromagnetic shape memory alloys. Further work could be done to discover the mechanism of this effect and to determine whether it is unique to Terbium or if other cheaper and more abundant elements could perform the same function. It would also be interesting to see whether Terbium substitution had a similar effect on other ferromagnetic shape memory systems, in particular Ni-Mn-Ga and Co-Ni-Ga.

One thing that is clear from this work though is that deposition of thin films of these ferromagnetic shape memory alloys does require a UHV system with turbo-molecular and scroll pump which have no oil exposed to the vacuum. The energetic nature of the ablation plume in PLD and the plasma in sputtering promotes chemical reactions between contaminants and the highly reactive elements in the deposited film, degrading film quality. Care must be taken with cleanliness of the vacuum chamber as even excess vacuum grease has been shown to contaminate samples of Ni-Mn-Ga when it is warmed and allowed to outgas into the chamber.

References

- [1] O. Heczko, P. Svec, D. Janickovic, and K. Ullakko, "Magnetic properties of Ni-Mn-Ga ribbon prepared by rapid solidification," *IEEE Trans. Mag.*, vol. 38, pp. 2841-2843, 2002.
- [2] C. Jiang, Y. Muhammad, L. Deng, W. Wu, and H. XU, "Composition dependance on the martensitic structures of the Mn rich NiMnGa alloys," *Acta. Mater.*, vol. 52, pp. 2779-2785, 2004.
- [3] X. Jin, M. Marioni, D. Bono, S. M. Allen, and R. C. O'Handley, "Empirical mapping of NiMnGa properties with composition and valence electron concentration," *J.Appl.Phys*, vol. 91, pp. 8222-8224, 2002.
- [4] M.Ohtsuka, M.Sanada, M.Matsumoto, and K.Itagaki, "Magnetic field induced shape memory in NiMnGa sputtered films," *Mater. Sci. Eng.*, vol. 378, pp. 377-383, 2004.

Appendix 1: Publications resulting from this research.

N.Dearing and A.G.Jenner "Magnetic and magnetoelastic properties of melt spun Ni-Mn-Ga", IEEE Trans. Mag. Vol.42 (2006), p. 78